

The Morphology and Optical Properties of Organic Molecules and Heterostructures

Manal Alkhamisi

Supervised by Professor Peter H. Beton

Thesis submitted to the University of Nottingham

for the degree of Doctor of Philosophy

February 2020

School of Physics and Astronomy
University of Nottingham

United Kingdom

Abstract

By growing optically active small organic molecules on insulating substrates, the interplay between their optical properties and structural control imposed by molecular self-assembly and the formation of molecular heterostructures can be explored. Controlling the arrangement of molecules within nano-structures is of great interest as a means to develop materials with novel optical and electronic properties.

The first part of this body of work deals with the case of the self-assembly of free-base phthalocyanine (H_2Pc) monolayers on hBN. Needle-like islands were found to arrange on the surface with orientations reflecting the symmetry of the underlying hBN lattice, which has three axes of rotational symmetry. The unit cell of this organic monolayer was extracted from high resolution AFM images and found to be a_{Pc}= b_{Pc}= 2.2 $\pm$ 0.03 nm and a_{Pc}= b_{Pc}= 2.18 $\pm$ 0.05 nm for room temperature and higher substrate temperature growth respectively. These lattice vectors were also found to be subtended by an angle θ= 86°. The vibrationless optical transition (0-0) of H_2Pc monolayers adsorbed on hBN (1.879 eV) was measured using steady state photoluminecence, and was found to be red shifted by ΔE= 0.13 eV. The ZnPc molecule was also investigated, and was found to form islands with a height (0.6 $\pm$ 0.1 nm), consistent with molecules adsorbed in a non-planar geometry. Fluorescence spectroscopy was carried out on the ZnPc layers on hBN, with a peak observed at 1.82 eV.

The growth of NTCDI on hBN, resulted in the formation of anisotropic monolayer islands with height of 0.3 ± 0.1 nm. As the substrate temperature was increased, the size of islands was found to increase, and the island morphology changes to a lily- pad shape for further increased in temperature growth. Upon a description of the growth of NTCDI films, the formation of heterostructures produced by sequential deposition of PTCDI/NTCDI, and NTCDI/PTCDI on hBN/SiO_2 was then discussed.

Heterostructures of thick hBN flakes and monolayers of PTCDI were formed using mechanical flake transfer. The change in properties of the encapsulated material was explored with photoluminescence (PL). This simple case of PTCDI encapsulated by hBN approach offers numerous opportunities to fabricate technologically relevant devices, such systems offer many opportunities to fabricate electronic devices where structure can be imposed on the molecular and monolayer thickness length scales in the in-plane and out-of-plane directions respectively.

Finally, the self-assembly of PCDA molecules on hBN and HOPG surfaces was carried out using different solvents and different concentrations. Highly ordered islands grown on these surfaces were observed using AFM. The self-assembled molecules on hBN were exposed to UV light (245 nm), and the light induced polymerisation of these was discussed. The intensity of the PL response increased as a result of increasing the exposure time.

Acknowledgements

I would like to express my deepest gratitude to my supervisor Professor Peter Beton for his excellent supervision and guidance throughout the different stages of this thesis. As a student, I have advanced greatly in my knowledge and expertise which was aided by his support throughout my studies.

I also would like to thank my colleagues; Dr James Kerfoot, Dr Abigail Browning, James Thomas, Dr Juan Albar, Dr Simon Svatek, Dr Vladimir Korolkov, and Dr Alex Summerfield for their support and for dedicating time to exchange knowledge and experience that helped me overcome challenges more easily.

The Nottingham Nanoscience group has provided a very productive working environment that facilitated the work of researchers and my thanks are extended to them as a collective entity. I should also thank King Abdula-Aziz University for grant me the scholarship to pursue my ambition and to quench my thirst for further studies in the nanoscience field.

I would like to express my heartfelt gratitude to my family; my parents, my sisters and brothers. This thesis won't saw the light of day without the unconditional support of their encouraging words were the fuel that get me going in times where giving up felt the only option.

My deepest thank go to my husband, **Mubarak**, my backbone. Without you and your understanding and sacrifices, it would have not been possible to continue my studies. My little girls, **Nada** and **Lena**, whose dancing routines cheer us up without a fail every time. A special mention to my youngest, **Akram**, I had to leave you back home when you were two months old. While being away from me, I spent every-night thinking of you. You can't imagine the suffering I endured. I brought you here with the anxiety that you need to be compensated for living away from your family, only to find that you were the one who compensated me for all the hard work I am going through. I highly appreciate your endurance and patience.

List of publications

- **M. Alkhamisi**, V. V Korolkov, A. S. Nizovtsev, J. Kerfoot, T. Taniguchi, K. Watanabe, N. A. Besley, E. Besley, and P. H. Beton, "The growth and fluorescence of phthalocyanine monolayers, thin films and multilayers on hexagonal boron nitride," Chem. Commun., vol. 54, no. 85, pp. 12021–12024, 2018.

- J. Kerfoot, V. V Korolkov, A. S. Nizovtsev, **M. Alkhamisi**, T. Taniguchi, K. Watanabe, P. W Parkinson, and P. H. Beton, "Two-Dimensional Diffusion of Excitons in a Perylene Diimide Monolayer Quenched by a Fullerene Heterojunction," The Journal of Physical Chemistry C, 2019.

List of conference abstracts

- **M. Alkhamisi**, V. V Korolkov, A. S. Nizovtsev, J. Kerfoot, T. Taniguchi, K. Watanabe, N. A. Besley, E. Besley, and P. H. Beton, "The growth and fluorescence of phthalocyanine monolayers, thin films and multilayers on hexagonal boron nitride," DPG Spring Metting2018., Germany, Berlin, 11-16 March (2018).

- **M. Alkhamisi**,, V. V Korolkov, A. S. Nizovtsev, J. Kerfoot, T. Taniguchi, K. Watanabe, N. A. Besley, E. Besley, and P. H. Beton, "The growth and fluorescence of phthalocyanine monolayers, thin films and multilayers on hexagonal boron nitride," E-MRS Spring Metting2018., France, Strasbourge, 18-22 June, (2018).

  In this conference, ChemComm honored me with poster prize.

- **M. Alkhamisi**,, J. Kerfoot, V. V Korolkov, T. Taniguchi, K. Watanabe, and P. H. Beton, "NTCDI Thin Films and NTCDI/PTCDI Heterostructures on Hexagonal Boron Nitride," RMS SPM Metting2018., UK, Leeds, 25-26 June (2018).

- **M. Alkhamisi**, J. Kerfoot, V. V Korolkov, T. Taniguchi, K. Watanabe, and P. H. Beton, "NTCDI Thin Films and NTCDI/PTCDI Heterostructures on Hexagonal Boron Nitride," mmc2019., UK, Manchester, 1-5 July (2019).

Glossary

AFM- Atomic Force Microscopy.

AM-AFM Amplitude Modulated Atomic Force Microscopy.

DFT-Density Functional Theory.

DOS- Density of States.

FM-AFM- Frequency Modulated Atomic Force Microscopy.

H_2Pc- Free base Phthalocyanice.

hBN – Hexagonal Boron Nitride.

HOMO – Highest Occupied Molecular Orbital.

HOPG – Highly Oriented Pyrolytic Graphite.

LUMO- Lowest Unoccupied Molecular Orbital.

ML- Monolayer.

NC-AFM- Non-contact Atomic Force Microscopy.

PDMS- Poly di-methyl siloxane.

PPC- Poly propylene carbonate.

PTCDI- Perylene tetracarboxylic diimide.

QCM- Quartz Crystal Microbalance.

RT- Room Temperature.

SiO_2/Si - Thermally Oxidised Silicon Dioxide on Silicon.

SPM- Scanning Probe Microscopy.

STM- Scanning Tunnelling Microscopy.

STML- Scanning Tunnelling Microscopy induced luminescence.

UHV- Ultra High Vacuum.

vdW- van der Waals.

ZnPc- Zinc Phthalocyanice.

Contents

1 Introduction **1**

1.1 Thesis outline 4

2 Theory and background **6**

2.1 Organic molecular structure 6

2.2 Theory of thin film growth on surfaces 8

2.3 Organic molecules used in this work 12

2.3.1 Phthalocyanine 12

2.3.2 PTCDI 15

2.3.3 NTCDI 19

2.3.4 PCDA 21

2.4 Substrate materials 24

2.4.1 HOPG 24

2.4.2 Hexagonal boron nitride 26

3 Experimental techniques, methodology and sample preparation **28**

3.1 Scanning probe microscopy (SPM) 29
3.1.1 Scanning tunneling microscopy (STM) 30
3.1.2 Atomic force microscopy (AFM) 35
3.1.3 Static AFM (contact mode) 38
3.1.4 Dynamic AFM (non-contact mode) 42
3.2 Impact of AFM tip termination 46
3.3 AFM cantilever configurations 47
3.4 Optical microscopy 47
3.5 Fluorescence 50
3.6 Sample preparation 52
3.6.1 SiO_2 substrate 52
3.6.2 Exfoliated hBN 53
3.7 Vacuum deposition system 53
3.8 Heterostructure fabrication using stamping 57
3.8.1 Polymer stamp preparation 58
3.9 Summary 59

4 Phthalocyanine on hexagonal boron nitride 61

4.1 Growth of phthalocyanine thin films 62
4.1.1 Growth of H_2Pc monolayer 62
4.1.2 The morphology of H_2Pc thin films on hBN: coverage dependence 69

4.1.3 The morphology of H_2Pc thin films on hBN: temperature dependence . . . 77

4.2 The Fluorescence of H_2Pc thin films on hBN . . . 79

4.3 The fluorescence of H_2Pc thick films on hBN at different substrate temperatures . . . 85

4.4 Growth and fluorescence of ZnPc thin films on hBN at room temperature 89

4.5 Summary . . . 90

5 NTCDI thin films and heterostructure of organic molecules on hexagonal boron nitride 92

5.1 Growth of sub-monolayer NTCDI at room temperature . . . 94

5.2 NTCDI on hBN: temperature dependence . . . 96

5.3 NTCDI on hBN: thickness dependence . . . 101

5.4 Sequential formation of PTCDI/NTCDI heterostructures . . . 102

5.4.1 PTCDI on NTCDI . . . 103

5.4.2 NTCDI on PTCDI . . . 109

5.4.3 NTCDI/PTCDI/NTCDI . . . 111

5.5 The fluorescence of sublimed NTCDI and NTCDI/PTCDI heterostructure on hBN . . . 112

5.6 Summary . . . 115

6 Encapsulating PTCDI between hBN layers 116

6.1 Transfer of flakes by mechanical transfer . . . 117

6.2 Different cleaning approaches 120

6.2.1 Furnace clean 121

6.2.2 Solvent clean 122

6.3 Comparison of different cleaning methods 123

6.4 PTCDI polarisation 124

6.5 Summary 127

7 Self-assembly and photo-polymerization of diacetylene molecular wire on hBN and HOPG **128**

7.1 AFM investigation of PCDA self-assemble on HOPG 131

7.2 Deposition of PCDA on hBN 134

7.3 Polymerization under UV light 138

7.4 Summary 142

8 Conclusion **143**

Bibliography **148**

CHAPTER 1

Introduction

Developing functional electronic and optoelectronic devices using organic molecules offers a pathway to new technologies which are competitive with existing extensively used inorganic semiconductors [1–6]. Using established synthesis techniques, a vast array of molecular structures can be realised and modified in order to engineer desirable physical properties [7, 8]. Furthermore, organic systems often have mechanical and chemical properties which offer a number of potential advantages over current inorganic wafer based processes. In particular, there is the possibility of flexible, stretchable, and printable functional materials which could be produced using scalable fabrication methods at a relatively nominal cost [9].

With organic materials, the ability to control molecular structure is very well established, whereas the control over intermolecular structure is often somewhat limited. This poses a challenge to the goal of realising practical organic devices, as crucial properties for device performance, including carrier mobility, exciton diffusion, exciton dissociation, absorption and emission maxima often depend heavily upon the intermolecular structure. One way in which the structure of such materials can be affected by

adsorbing such materials on a surface, where particular interactions such as hydrogen bonding, dipole-dipole interaction, metal-organic coordination, and charge transfer mechanisms can give rise to a variety of molecular packing structures.

Growing well defined assemblies of organic materials on a surface is important in realising their potential for applications in nanotechnology. The molecular and surface science community has studied organic molecules adsorbed at interface for decades, with particular emphasis towards molecular self-assembly on conductive surfaces addressed using scanning tunnelling microscopy (STM) under ultra-high vacuum (UHV) conditions, ambient conditions and at the liquid-solid interface [10]. The 2D periodic structure of many hydrogen bonded systems has also been studied on many conducting substrates, including highly oriented pyrolytic graphite (HOPG), graphene, molybdenum disulphide and noble metals [11–14].

Conductive substrates are a pre-requisite for any STM study of supramolecular self-assembly. However, in order to study electronic and optical properties of such systems, an insulating substrate is required in order to eliminate effects such as quenching and substrate interactions. In particular, using non-conducting substrates is the only way to obtain optical properties and to prevent fluorescence quenching. Influencing intermolecular structure in order to promote desirable functional properties and possible device architectures on surfaces is a major goal in the surface science community, with a number of particularly elegant recent experiments by groups utilising alkali halide spacer layers on noble metals offering significant promise in realising this goal [15].

Using hBN as an insulating substrate is a good choice since it is offers an atomically flat and weakly interacting surface which is compatible with molecular deposition and

subsequent characterisation [16–19]. In this case, it is possible to use AFM to identify and control molecular ordering within an adsorbed monolayer at an interface.

The motivation of this study is to investigate the morphology and structure of organic molecules since their electronic, optical and physical properties make them promising materials for active components in optoelectronic devices. In these applications, producing well-ordered monolayers is very important for understanding fundamental molecular properties and may also be related to device performance. The properties of organic molecules are significantly affected by the organic-substrate interface. This makes it necessary to understand, in detail, the structural formation, electronic properties and adsorption of the electronically active molecules on various surfaces.

In this thesis, the morphology and structure of sublimed organic molecules are studied. Thin films of organic molecules have been successfully fabricated by sublimation on hBN/SiO_2 substrates using ultra high vacuum (UHV) deposition technique. The molecules are deposited on the substrate held at or above room temperature using a controlled rate of deposition to obtain various film thicknesses. In addition to use UHV environment for molecues deposition, the morphology and structure of the solution deposition of 10, 12-pentacosadiynoic acid (PCDA) on both hBN/SiO_2 and HOPG are studied. In this investigation, atomic force microscopy (AFM) was the main technique used to investigation the surface topography, while photoluminescence (PL) was also measured in conjunction with an optical microscope in order to determine the local optical properties. This experiment aims at characterising the morphology of the mono and multi-layers of the organic materials on hBN/SiO_2 and HOPG substrates and observe their structural and optical properties. The formation of these layers is

affected by many conditions including the temperature of the substrate surface during deposition, as well as the film thickness.

1.1 Thesis outline

This thesis aims to shed light on how the arrangement of molecules on a surface can have an effect on their optical characteristics.

Chapter Two will provide a discussion of the general background in relation to the mechanism of thin film growth on the surfaces. Another topic to be discussed is the scanning tunnelling microscopy (STM) investigations of fluorescent species on metal surfaces, especially in terms of the potential for templating the molecular arrangement through hydrogen bonding with supramolecular networks. In this chapter, the molecules under investigation in this study, including perylene tetracarboxylic diimide (PTCDI), naphthalenetetracarboxylic diimide (NTCDI), phthalocyanine (Pc), and 10,12-pentacosadiynoic acid (PCDA) will be introduced. The substrates used including the vdW crystals HOPG and hBN will also be discussed.

Chapter Three will provide an introduction into the experimental mechanisms adopted in this study. These include STM for electronic surface properties, AFM for morphology and structural investigations, and optical and fluorescence microscopies for studying the surface and investigating optical properties. Following this, preparation techniques for SiO_2 substrates and exfoliated hBN will be discussed. The vacuum deposition used in this study will also be described in detail. Finally, the stamping processes for flake transfer and heterostructure creation including polymer stamp preparation and usage are discussed.

In **Chapter Four**, the deposition of the free-base phthalocyanic (H_2Pc) and zinc phthalocyanic (ZnPc) grown on hBN will be discussed. Also shown are fluorescence measurements from these films on the morphology of H_2Pc and ZnPc thin films grown on hBN at a number of substrate temperatures and substrate thickness. There will also be a discussion on the fluorescence influence of on the optical properties of these films.

Chapter Five provides a discussion of NTCDI thin films sublimed on hBN in UHV, with monolayer islands observed for the growth at room temperature, and an investigation of morphology at increasing substrates temperature. Further discussion in this chapter on the formation of sequential heterostructures of two species of organic molecules is also provided.

In chapter Six, PTCDI molecules sandwiched between two hBN flakes to form layered heterostructure made using the stamping process described in chapter 3 are studied.

Chapter Seven covers the solution deposition of PCDA on both hBN and HOPG and it's analysis with AFM.

CHAPTER 2

Theory and background

In this chapter, organic molecular structure, π-conjugated systems, the mechanism of thin film growth on surface, and some of the organic materials used in this thesis are introduced.

2.1 Organic molecular structure

Organic materials - polymers and small molecules - comprise of carbon and other elements that are connected by covalent bonds. Organic materials which have a π-conjugated system display a certain degree of conductivity, behaving like semiconductors [20]. In this regard, π-conjugated systems, in both small-molecules and polymer semiconductors, are of prime interest owing to their unique electrical and optical properties paving the way for the fabrication of new optoelectronic devices with unique functionalities [21, 22].

Each constituent atom has electron orbitals corresponding to different energy levels such as 1s, 2p, 3d, and 4f, etc.. The interaction between two or more atoms can lead to

the combination of their atomic orbitals to form a molecular orbitals. These molecular orbitals can be either bonding (lower energy, e.g. π) or anti-bonding (higher energy, π^*) as shown in Figure 2.1.

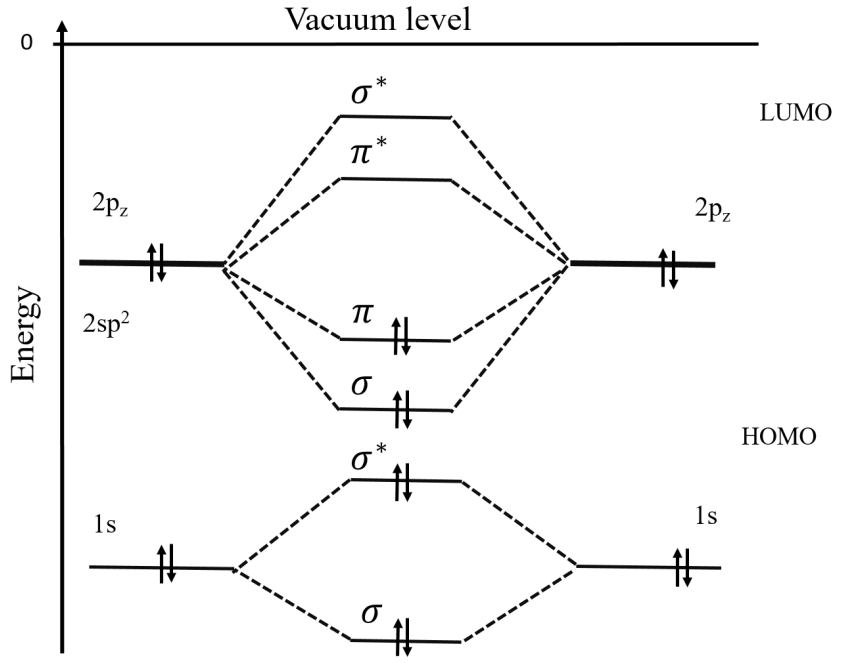


Figure 2.1: Simplified energy level diagram illustrating the formation of σ and π bonds in small semiconductor molecules.

Figure 2.2 illustrates that the C-atoms in ethene, (C_2H_4) for example, typically have sp^2 hybridised orbitals and form σ-bonds. Unhybridised p_z orbitals that are perpendicular to the hybridized orbitals will form π-bonds for a large molecule can be delocalised forming a conjugated system. Thus, the electrons have some freedom to move along the entire chain. These π-bonds are divided between bonding and anti-bonding states, thus constituting the band gap of semiconducting molecules. This energy difference between π and π^* orbitals typically lies in the range of a few electron volts. As a result, many conjugated organic molecules display semiconducting properties for many or-

ganic materials for example phthalocyanine, perylene tetracarboxylic diimide (PTCDI), and naphthalenetetracarboxylic diimide (NTCDI).

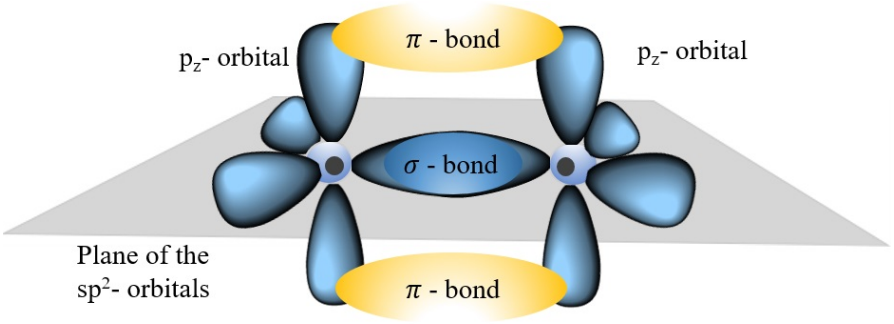


Figure 2.2: Schematic diagram of the orbital bonds in ethene.

2.2 Theory of thin film growth on surfaces

Molecular deposition is a non-equilibrium and dynamic process often used to grow thin organic films under vacuum conditions. There exist several models that have been applied for the growth of various organic semiconductors. It is important to understand the growth process and structure formation because it is crucial for technological progress [23–29]. In the initial stage of growth the organic molecules arrive at the substrate surface with deposition rate, R, [30] given by

$$R = P/(2\pi m k_B T)^{1/2} \tag{2.1}$$

where P is the vapour pressure, m is the mass of the molecules, k_B is the Boltzmann constant and T is the temperature.

A number of mechanisms can generate the attractive interactions between deposited molecules and a substrate, which can control the arrangement of molecular thin films at interfaces. When the molecules impinge on the surface, there are two possibilities.

The molecules may not bind to the surface (reflected) if the loss of the energy is not sufficient, or they lose energy and become bound to the surface (adsorbed).

The adsorption process is categorised in two ways depending on binding strength and mechanism; these are physical adsorption (physisorption) and chemical adsorption (chemisorption). The van der Waals interaction is an example of physisorption. In the van der Waals interaction spontaneous dipoles within molecules induce dipoles within adjacent molecules and surface atoms. This type of bonding is weak and occurs in all materials [31]. When spontaneous and induced dipoles interact, an attractive force results, known as the London force, and is the attractive element of the Lennard-Jones potential.

Following adsorption on the surface, the molecule can diffuse, by jumping to adjacent binding sites or become localised at one site [26, 28, 32]. An increase in the substrate temperature leads to an increase in the probability that a given molecule can hop to an adjacent binding site. The diffusion coefficient, D , the rate at which molecules jump to the next adsorption site, is given by

$$D = D_0 \exp\left(-E_d / k_B T\right) \tag{2.2}$$

where D_0 is $v_d\ a^2$ (v_d is the vibration frequency of adatoms, a the distance of jump) and E_d is the diffusion energy barrier between two adjacent sites [33].

Diffusion of molecules across the substrate surface occurs until they either desorb or occupy a binding site on the surface with a greater binding energy. It is common for such binding to take place at step edges and defects on the substrate, and along the edges of pre-formed clusters (islands) of molecules. In addition, new stable clusters on the surface can form through nucleation caused by the interaction of a number of mo-

bile molecules [26]. The nucleation occurs during the primary stages of growth when the first molecules arrive on the surface and create a stable cluster. At a specific temperature, the critical cluster size refers to the number of molecules needed to generate a cluster that is kinetically stable, to the extent that the rate of attachment of additional molecules surpasses the rate of detachment of molecules bound to the island.

Assuming the arrival rate of molecules per unit area on the surface is R, the time that a molecule takes to desorb from the surface, τ_a, the time for isolated molecules to cluster together in nucleation events, τ_n, the time for molecules to merge into stable clusters on the surface, τ_c, and the rate of coalescence of pre-formed critical islands $U_{Cluster}$, a pair of coupled equations can be extracted for n_1 and n_x, the surface concentrations of isolated molecules and critical clusters respectively, as shown in Equations 2.3 and 2.4 [26, 33, 34].

$$\frac{dn_1}{dt} = R - \frac{n_1}{\tau} \quad \text{where,} \quad \tau^{-1} = \tau_a^{-1} + \tau_n^{-1} + \tau_c^{-1} + ... \tag{2.3}$$

$$\frac{dn_x}{dt} = \frac{n_1}{\tau_c} - U_{Cluster} \tag{2.4}$$

Several physics models have been proposed to describe the island growth of organic layers [35, 36]. The number of islands per unit area *(N)* depends on the deposition rate, R, and the substrate temperature, T, as given in Equation 2.5

$$N = R^{\delta} \exp\left(E_N/kT\right) \tag{2.5}$$

where, δ=$i/(i$+2), and, i is the number of molecules forming a stable cluster. E_N is the nucleation energy barrier and is defined as:

$$E_N = E_i + iE_d/(i+2) \tag{2.6}$$

where E_d is the diffusion energy barrier, E_i is the difference in surface energy between i adsorbed molecules on the substrate and i molecules in a stable cluster.

The following mechanisms of growth formation occur during the deposition of thin films as shown in Figure 2.3; arrival, diffusion, nucleation and adsorption [33].

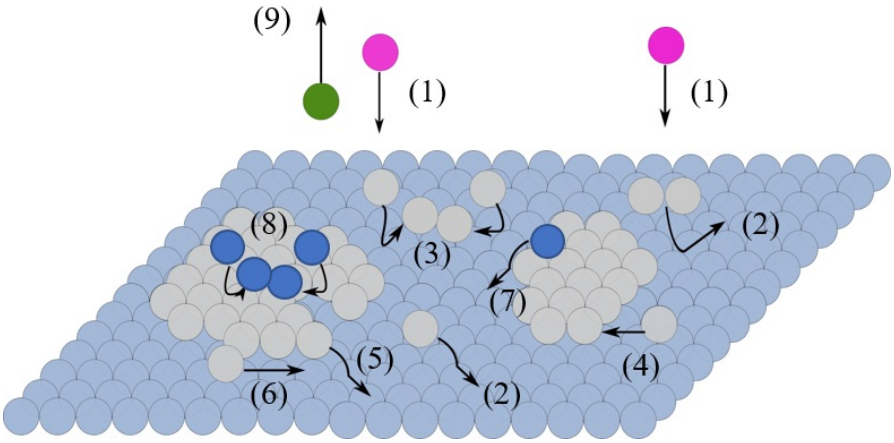


Figure 2.3: Typical processes of thin film growth; (1) when the atoms or molecules of organic materials evaporate onto a surface substrate, (2) diffusion of the atoms on the surface, (3) atoms meet other atoms to form dimers,(4) an atom attaches to an existing island, (5) or diffuses from an island, (6) diffusion along the island edge, (7,8) deposition onto existing islands followed by any of the previous processes, (9) re-evaporation at high temperature.

As shown in Figure 2.4, the film morphology is classified in three modes of thin film growth which each take into account the surface energies of the substrate, the film, and the interface between them [33]. The Frank-van der Merwe mode (layer by layer growth) occurs if the interaction strength between the adsorbates and the substrate

exceeds the interaction strength between the molecules themselves. During this mode of growth, a complete layer is formed followed by the growth of higher layers. Volmer-Weber mode (island growth) is achieved if the adsorbate molecules interact more strongly than their interaction with the substrate. In this case, small clusters are nucleated and grow in the form of islands. The Stranski-Krastanov mode (layer and island growth) occurs when the islands nucleate on the previously formed monolayer.

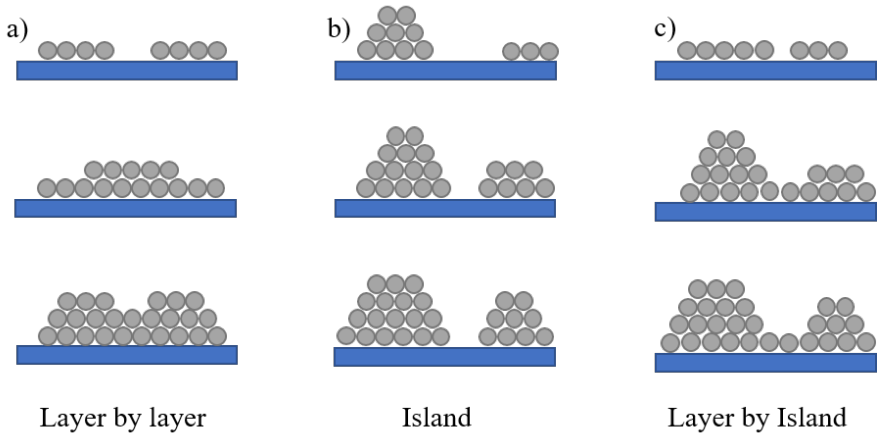


Figure 2.4: Schematic diagram of the three modes of thin film growth; a) Frank-van der Merwe (Layer by Layer), b) Volmer-Weber (Island), c) Stranski Krastanov (Layer by Island).

2.3 Organic molecules used in this work

2.3.1 Phthalocyanine

Phthalocyanines have an aromatic macro-cycle which consists of an 18 π-electron-conjugated system [37]. The chemical formula for this compound is $C_{32}H_{18}N_8$. Phthalocyanine derivatives have been utilized in important functional materials in many fields. Their useful properties are attributed to their efficient electron transfer abilities. The central cavity of phthalocyanines is known to be capable of accommodating 63

different elemental ions, including hydrogen. A phthalocyanine molecule containing one or two metal ions is known as a metal phthalocyanine (M-Pc). These are formed by coordination of a metal atom in the central cavity of the macrocycle with the four pyrrole nitrogen atoms [38]. The basic phthalocyanine molecules or free-base phthalocyanine (H_2Pc), were first reported in the year 1907 by Braun and Tcherniac who noted the reaction of benzamide in a hot alcohol solution, which resulted in a highly insoluble product with a blue colour. In order to describe the blue dye, Linstead first coined the term phthalocyanine in 1933.

This organic molecule has a range of interesting physiochemical properties due to its delocalized π-electron system, and has been used in dyes, chemical sensors, photodynamic cancer drugs, nonlinear optical materials and catalysts. It has a close relation with naturally occurring porphyrins. As depicted in Figure 2.5 the chemical structure for porphyrin and phthalocyanine both incorporate a ring macrocycle. These molecules share some similarity with the active group in chlorophyll and haemoglobin and are used in the field of biomimetics.

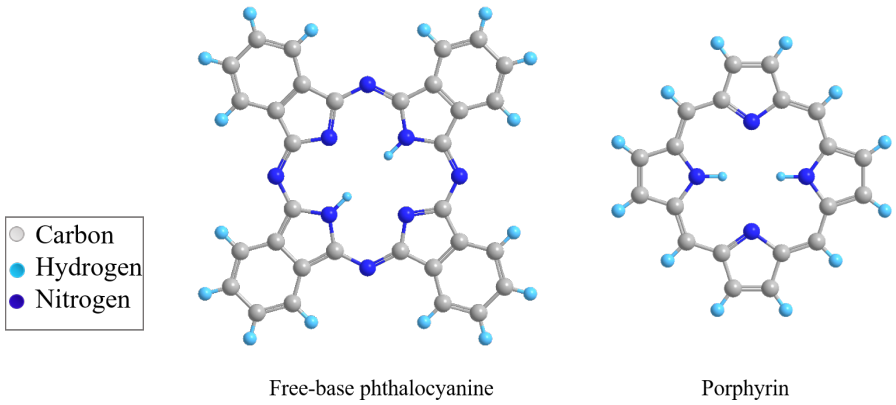


Figure 2.5: Chemical structure of free-base phthalocyanine, and the simplest example of a porphyrin.

Figure 2.6 shows highest occupied molecular orbital (HOMO) and lowest unoccupied molecular orbital (LUMO) of free-metal phthalocyanine [39].

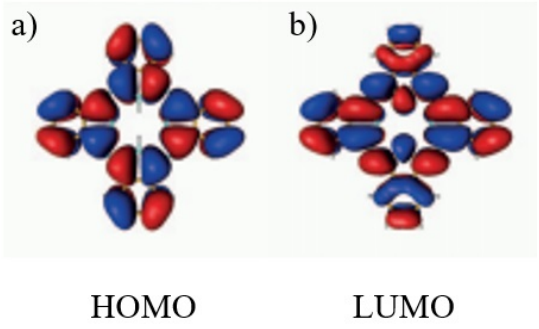


Figure 2.6: Diagram representing; a) the highest occupied molecular orbital π, b) the lowest unoccupied molecular orbital π^* of free-metal phthalocyanine [39].

The unique properties of phthalocyanines have led to their use in many applications. Due to their high stability, improved characteristics of spectroscopy and their diverse coordination properties, as well as their architectural flexibility, phthalocyanines are preferred to porphyrins in numerous applications. The applications of phthalocyanine in organic solar cells [40, 41] and transistors [42] are of particular interest. It has been reported that phthalocyanine acts as a donor material in molecular electronics so can be used as a hole transport layer [43] or emitting layer [44] in LEDs. Phthalocyanines can also be used as chemically sensitive films for gas sensors [45]. In addition, phthalocyanines are easy to handle in vacuum and their thermal and chemical stability facilitates sublimation at temperatures ranging between $300 - 500°C$. Numerous studies have been carried out on metal phthalocyanine and metal-free phthalocyanine on different surfaces with the aim of developing devices [46–49]. For example, Gopakumar et al. have investigated the adsorption of palladium phthalocyanine on graphite using STM [50] (see Figure 2.7).

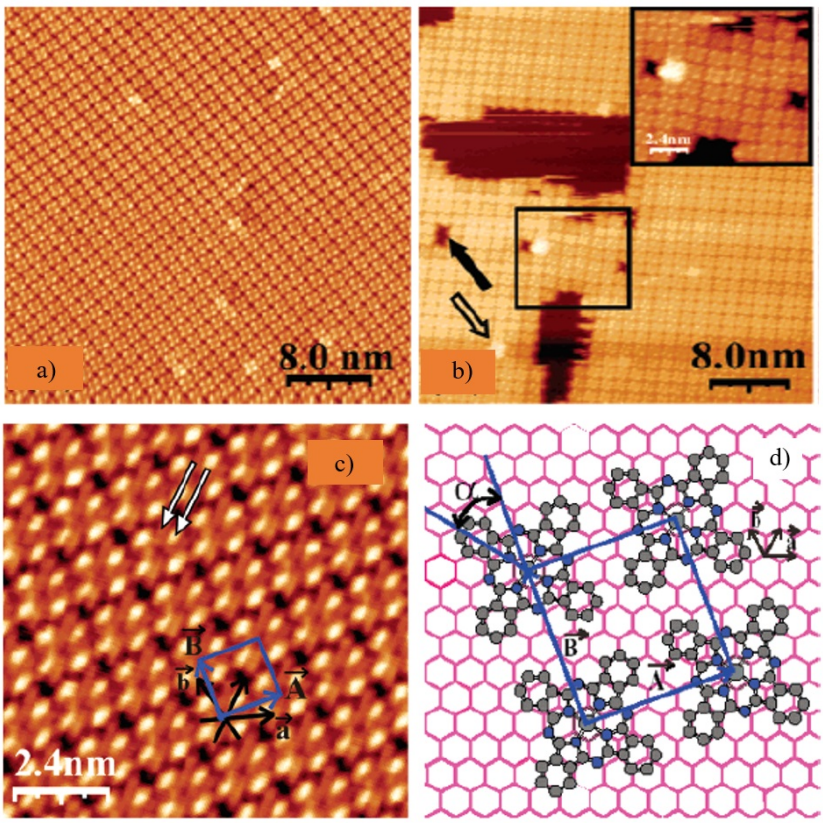


Figure 2.7: (a, (b),and (c) STM images of the PdPc monolayer on graphite. The inset in (b) shows the area within the black square with a higher magnification. The unit cell is represented by a blue square in (c), and is shown schematically in (d) for a PdPc monolayer on graphite. The ($\vec{A}$,$\vec{B}$) represent the PdPc unit cell vectors while ($\vec{a}$,$\vec{b}$) represent the vectors of the graphite sheet [50].

These observations of such molecules on various surfaces have catalysed the focus in the existing study which centres on studying metal-free phthalocyanine molecules sublimated onto hBN/SiO_2 surfaces as discussed in further detail in chapter 4.

2.3.2 PTCDI

Perylene is a molecule comprising 20 sp^2 hybridised carbon atoms that make up a π-conjugated system. This molecule is made up of five covalently bonded benzene

rings terminated by hydrogen atoms. The functionalisation of perylene can be achieved through the addition of anhydride groups to the *peri*-positions of the molecule to produce perylene tetracarboxylic dianhydride (PTCDA) [51]. It can also be functionalised by adding imide groups, to form perylene tetracarboxylic diimide (PTCDI). Figure 2.8 illustrates the structures of perylene, PTCDA and PTCDI.

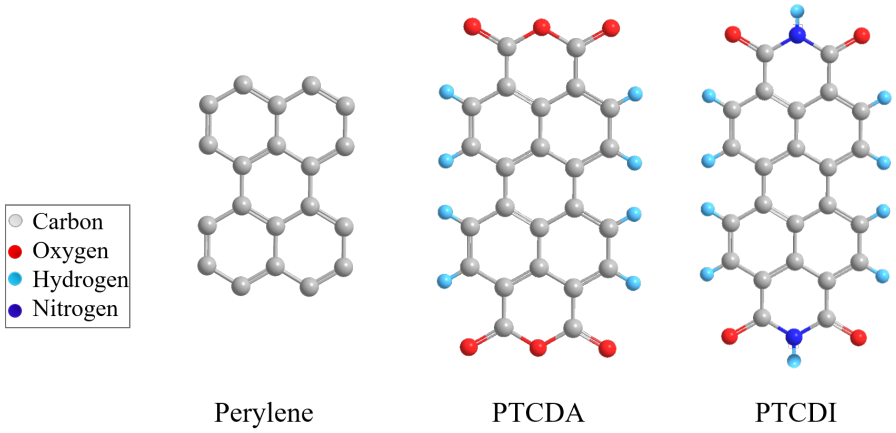


Figure 2.8: Chemical structure of perylene, PTCDA, and PTCDI are shown.

PTCDA, PTCDI and their derivatives were initially utilised as synthetic dyes, however, they are currently also frequently utilised in organic electronics. There are ongoing extensive studies of perylene derivatives as a result of their optical and electronic characteristics. There have also been investigations into the morphology of thin films of these molecules on a variety of substrates by means of both STM and AFM. It is possible to use the synthesis of molecules with a particular arrangement for the direction of their self-assembly into a number of 2D packing structures [52]. In such a way, one could utilise the templating of the arrangement of a molecular thin film to adjust a film's morphology and functional characteristics. It is also possible that the packing of fluorescent molecules within a thin film may have an effect on its optical features.

The Nottingham Nanoscience Group have used STM in UHV conditions to study both PTCDI and PTCDA onto the Ag-Si (111)-$\sqrt{3} \times \sqrt{3}$ surface [53]. There have also been extensive research efforts of PTCDI through the use of both STM and AFM on a range of substrates [53–56], along with several other investigations conducted on PTCDI derivatives. When on two dimensional surfaces, including highly oriented pyrolytic graphite (HOPG) and molybdenum disulphide (MoS_2), it has been found that PTCDI molecules can create a canted arrangement. In this structure, there is an alignment of PTCDI molecules in rows where molecules are counter rotated by 12° from the intra-row lattice vector for the maximised impact of intra-row hydrogen bonding. The rotation of the alternating rows occurs in the opposite direction, thus offering more packing efficiency, as shown in Figure 2.9 [54].

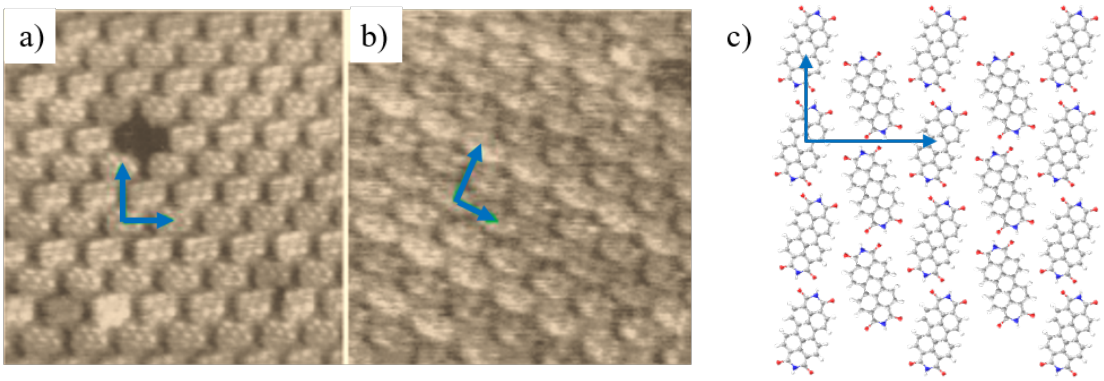


Figure 2.9: STM images of 10×10 nm PTCDI canted molecular packing arrangement on; a) MoS_2, and b) HOPG surfaces. c) schematic diagram of this molecular arrangement in rows to maximise intra-row hydrogen bonding, with adjacent rows counter rotated by ± 12° from the row direction. (a and b taken from [54]).

When co-deposited with melamine, PTCDI can also form a bi-component supramolecular network [8]. A junction between one melamine molecule and three PTCDI molecules is stabilised by hydrogen bonding between melamine and PTCDI molecules on the surface. This junction provides the basis of the PTCDI-melamine honeycomb net-

work, which takes place because of a stronger coupling between PTCDI and melamine (hetero-coupling) than between two molecules of a similar species (homo-coupling), as shown in Figure 2.10.

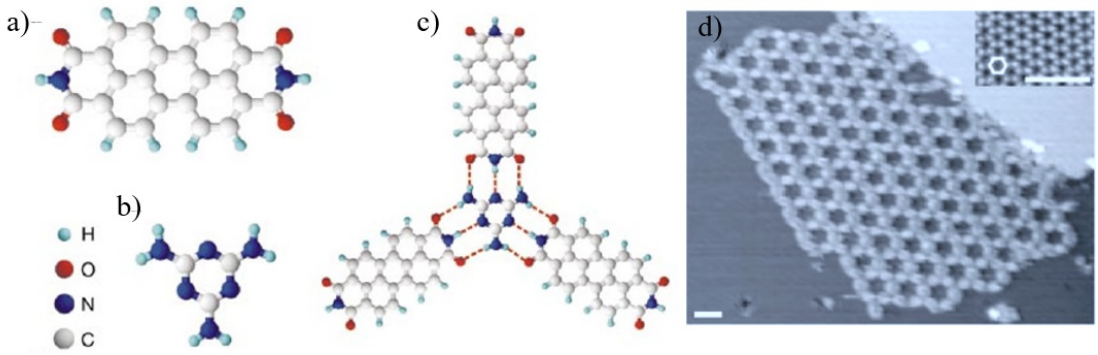


Figure 2.10: Building blocks of ; a) PTCDI, b) melamine, and c) the hydrogen bonding formed network between three PTCDI molecules and melamine , and d) STM images of hexagonal PTCDI-melamine supramolecular network formed on Ag/Si (111) surface, the scale bars 3 nm [8].

All previous studies have been carried out using STM requiring a conducting substrate. For insulating substrates AFM must be used. Other fairly recent studies by the Nottingham Nanoscience Group include the deposition of the PTCDI-melamine network from solution onto HOPG, molybdenum disulphide and hexagonal boron nitride (hBN) [57]. In addition, the Nottingham Nanoscience Group has acquired high resolution AFM images to explore the topography of PTCDI and PTCDA. Kerfoot el al. successfully achieved the solution deposition of monolayer thin films of PTCDI-melamine, PTCDI, and PTCDA on hBN as shown in Figure 2.11. The different molecular arrangements resulting from these thin films influence their fluorescence properties when adsorbed on an insulating surface [16].

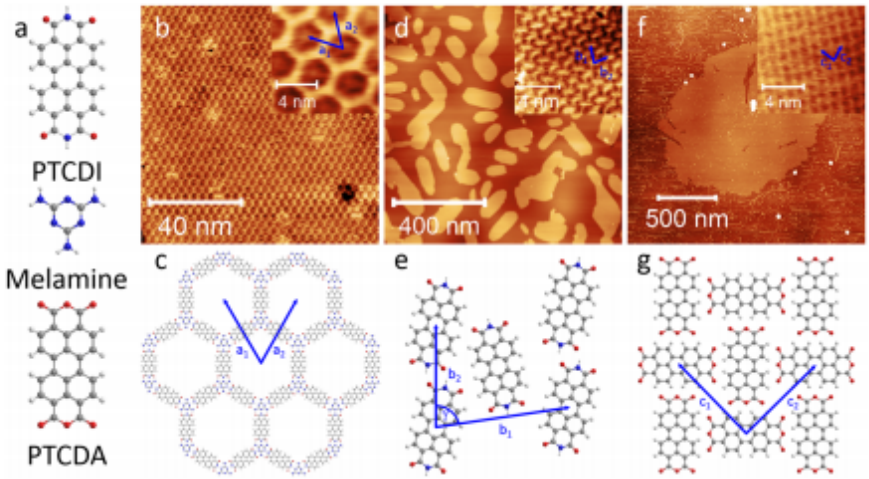


Figure 2.11: (a) building blocks of molecular structure. (b) AFM image of PTCDI-melamine network deposited from solution onto hBN. (c) schematic diagram showing the molecular honeycomb arrangement. (d) AFM image of PTCDI deposited from solution onto hBN. (e) schematic diagram showing the molecular arrangement in canted phase. (f) AFM image of PTCDA deposited from solution onto hBN. (g) schematic diagram showing the molecular arrangement in square phase [16].

2.3.3 NTCDI

A smaller analogue structure to PTCDI is naphthalenetetracarboxylic diimide (NTCDI) which is produced from the parent naphthalene via an intermediate compound naphthalenetetracarboxylic dianhydride. NTCDI contains two benzene rings, four carboxyl groups and two anhydrides. NTCDI is a solid organic compound and one of the simplest naphthalenediimides. The chemical structure of naphthalene and NTCDI are shown in Figure 2.12.

The Nottingham Nanoscience Group have also studied and used ultra-high vacuum (UHV) STM to deposit NTCDI and NTCDI-melamine onto the Ag-Si(111)-$\sqrt{3} \times \sqrt{3}$ surface [58, 59]. The STM images of NTCDI are shown in Figure 2.13 (a,b). Close

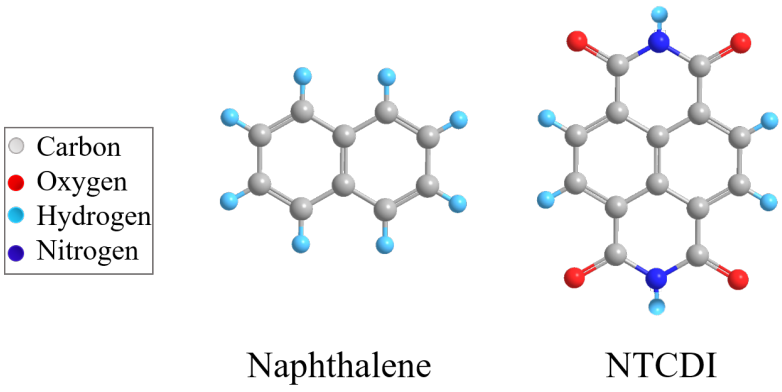


Figure 2.12: Chemical structure of naphthalene, and NTCDI are shown.

packed islands of NTCDI were observed (see Figure 2.13 for proposed molecular arrangement). The structure of NTCDI-melamine shows mixed phases as shown in Figure 2.13 that include; (d,e) triangular, (f,g) star, and (h,i) melamine taypes. Recently, and in addition to STM, NC-AFM has been used in UHV to deposit NTCDI on Si(111)-7×7 [60, 61]. NTCDI has also been deposited on Au(111) [62].

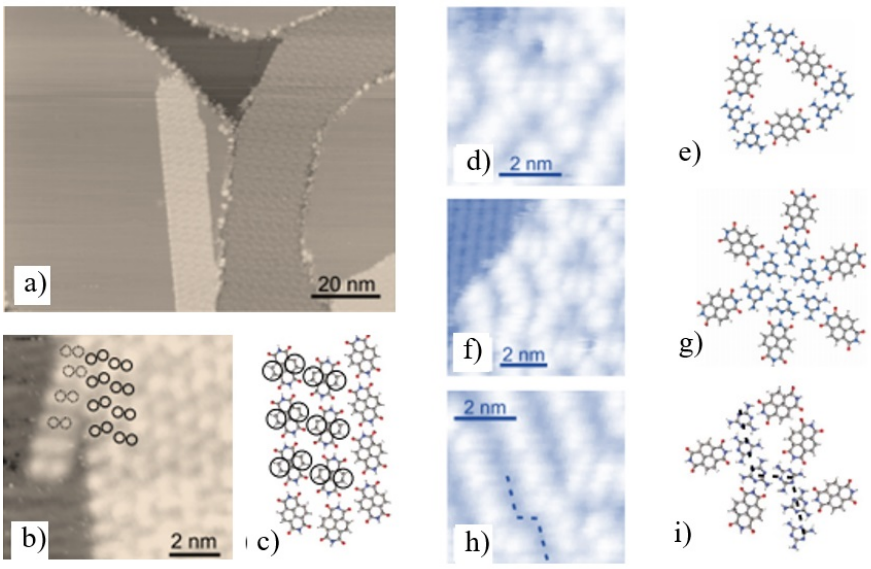


Figure 2.13: NTCDI and NTCDI-melamine deposited on Ag-Si(111)-$\sqrt{3} \times \sqrt{3}$ surface where; (a,b) STM images of NTCDI molecules packed with canted arrangement, c) schematic diagram of these molecules, (d,f,h) STM images of NTCDI-melamine, and (e,g,i) schematic diagrams of these molecules [58].

2.3.4 PCDA

Polydiacetylene is a conducting polymer closely related to polyacetylene. A monomer that can form a polydiacetylene polymer is 10, 12-pentacosadiynoic acid (PCDA) shown in Figure 2.14. These molecules have a general formula *R*-*C*≡*C*-*C*≡*C*-*R*′, where *C*≡*C*-*C*≡*C* is the diacetylene moiety. $CH_3(CH_2)_{11}$ is *R* and $(CH_2)_8COOH$ is *R*′, both corresponding to the substituent groups. These monomers and polymers have potential applications in biosensors, as pathogenic agents, and in optical and electrical devices [63].

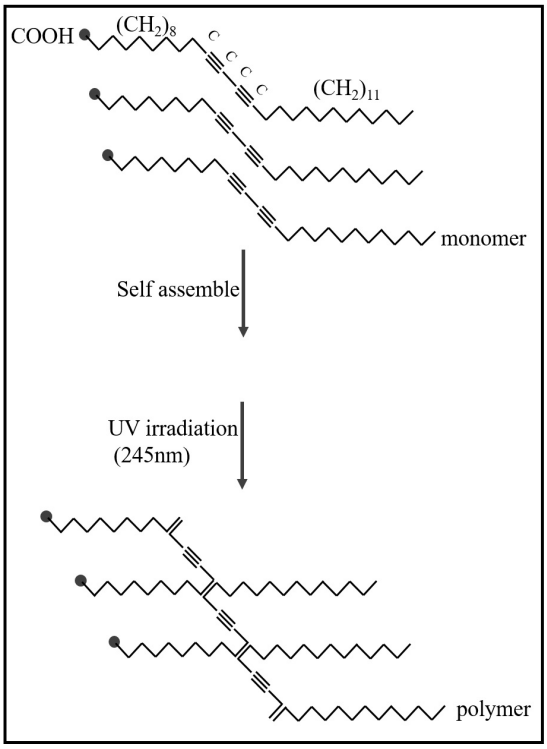


Figure 2.14: Chemical structure of 10, 12-pentacosadiynoic acid (PCDA) and the polymerization proceeds via UV irradiation of monomer units to produce the final conjugated polymer product.

The polydiacetylene polymer derived from PCDA monomers has alternative double and triple bonds which are generated when PCDA is exposed to UV light or external

stimuli, such as thermal, chemical and mechanical, as shown in Figure 2.14. The microstructure of these polymers were first reported by Wegner in 1969 [64]. These materials have remarkable properties which include uniform dimensional structures and responsive chromic characteristics that can be utilized as is, within a solution, or self-assembled onto various substrates, such as silica, polymer, and metal surfaces. Various attempts have been made to control the diameters and lengths of nanotubes formed from these monomers by changing chemical modifications and fabrication methods of amphiphilic diacetylene lipids. Fabricating well-defined diacetylene nanotubes of high purity has been a key interest among scientists who are studying biosensors, microelectronics, and drug delivery system [65].

The polymer links neighbouring PCDA molecules and forms a backbone with alternating double and triple bonds, (see Figures 2.15 (a-e) for detailed reaction) [66–70]. The AFM images in Figure 2.15 (f,g) show the polymerization reactions that occur after irradiation exposure of 5s (f), and after an additional 5 s (g).

An alternative method to form these polymers chains is to use electrical pulses from a STM tip [68, 71, 72]. Details of this method are shown in Figure 2.16. The STM image in Figure 2.16 (b) shows polymerization on HOPG surface, with the polymerized region highlighted by a green arrow.

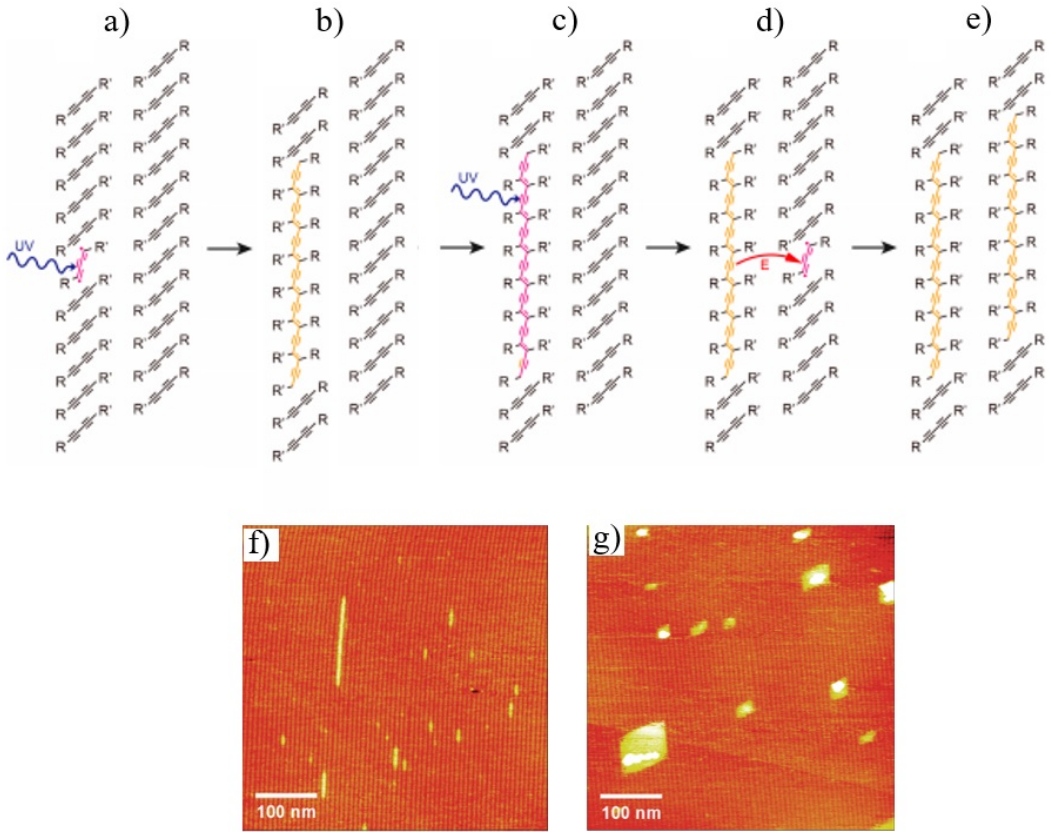


Figure 2.15: Schematic diagram illustrating the reaction details of PCDA self-assemble on hBN. a) the polymerization occurs when the layer is exposed to UV light and one of the molecules is excited, b) the chain is formed, c) when there is further irradiation the molecule adsorbs the additional energy, e) this energy is transferred to the neighbouring molecules, e) this result in polymerization, f) the AFM image of diacetylene on hBN after 5 s irradiation exposure, and g) after an additional 5 s [67].

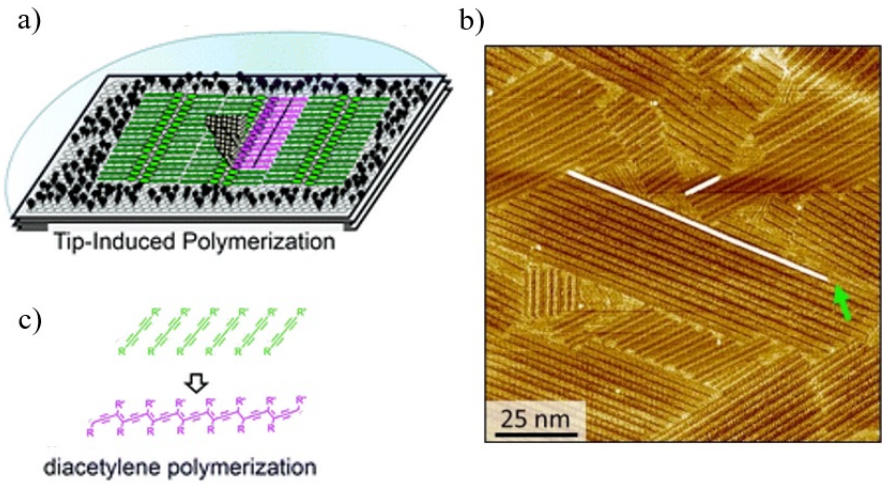


Figure 2.16: (a) supramolecular self-assemble of PCDA and use of STM tip to induce polymerization at a liquid-solid interface formed on HOPG, (b) the STM image demonstrating the polymerization indicated by the green arrow, (c) the model of the 1D diacetylene polymerization reaction [71].

2.4 Substrate materials

To acquire high resolution images of sub-nm structures using AFM, a highly ordered supporting substrate is required. In the following section the structure of some substrates used throughout this thesis are discussed.

2.4.1 HOPG

Graphite is a crystalline allotrope of carbon, it is made up of an sp^2 hybridised honeycomb array of covalently bonded carbon atoms with a bond length of 0.142 nm [73]. This unique structure gives graphite its exceptional transport and mechanical properties [74, 75]. Illustrated in Figure 2.17 is the crystal structure of a graphite sheet. In Figure 2.17 (a) the unit cell of graphite is shown, made up of two carbon sublattices, labelled A and B, acting as a rhombic unit cell that forms the arrangement of the bulk

hexagonal structure with a lattice constant of 0.246 nm. Van der Waals forces hold together stacked planes of carbon atoms, which are separated by a spacing of 0.34 nm, see Figure 2.17 (c).

Highly-ordered pyrolytic graphite (HOPG) refers to a level of graphite whereby the typical angular deviation between the sheets in the crystal is very low. One of its common uses is as an SPM substrate since it is stable under ambient conditions and due to its ease of preparation. The process of exposing a clean atomic plane of HOPG is relatively basic and corresponds to the removal of the top layers with adhesive tape, known as mechanical exfoliation, which results in a highly ordered surface which can be used as a substrate for molecular self-assembly experiments [76] .

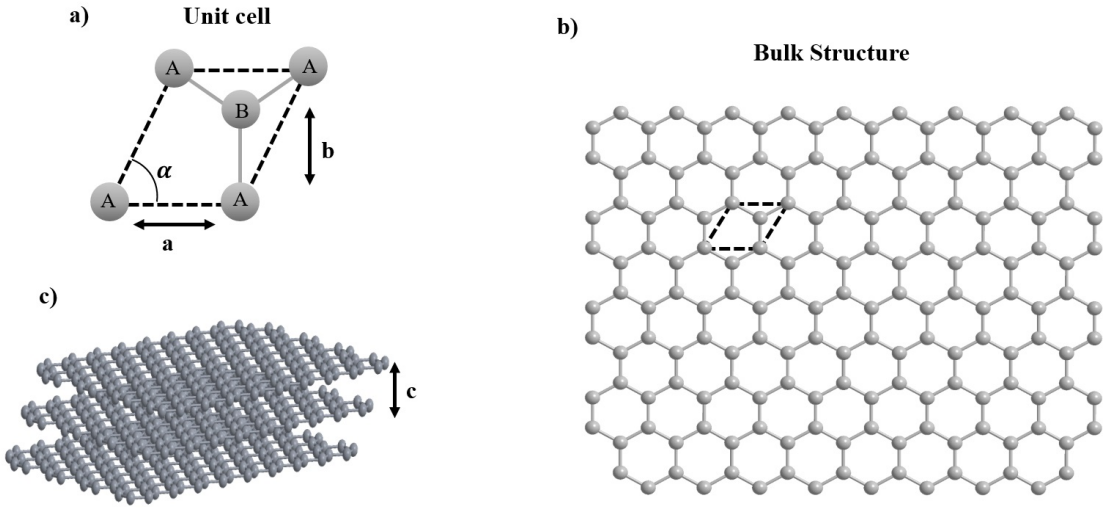


Figure 2.17: An illustration of graphite showing; a) the unit cell structure where a= 0.246 nm, b= 0.142 nm, and the angle α= 60 °, b) honeycomb crystal structure of a single graphite sheet (graphene) where the unit cell from a is marked with dashed black line, c) interlayer separation of the graphite sheet is, c= 0.34 nm.

2.4.2 Hexagonal boron nitride

Boron nitride, with the chemical formula (BN), consists of two elements: boron and nitrogen. Boron nitride can have different forms, hexagonal boron nitride (hBN), cubic BN and wurtzite BN. In the hexagonal form of boron nitride, alternate boron and nitrogen atoms are linked in a honeycomb arrangement, similar to the carbon atoms in graphite as shown in Figure 2.18 (b). The boron and nitrogen atoms are covalently bonded with separation of 0.145 nm and a lattice constant of 0.252 nm, while the layered structure is stabilised by weak van der Waals forces and separated by 0.33 nm as shown in Figure 2.18 (a,c) [77]. hBN is very interesting because of its remarkable physical properties and its chemical stability. hBN has been explored as a substrate for graphene [69, 78] and other 2D materials as well as for its integration into van der Waals heterostructures, where 2D materials layers are vertically stacked to fabricate novel electronic devices. hBN is a dielectric material with a large band gap of 6.0 eV [79, 80] and has a dielectric constant similar to silicon dioxide. One of its important uses is as a substrate because it has an atomically smooth surface which is free from dangling bonds and charge traps [81]. By micromechanical cleavage a single atomic plane of hBN, or flakes with thicknesses in the range 1 - 100 nm can be extracted from a bulk crystal. The hBN gives visible contrast on most substrates [82]. Figure 2.19 shows optical images of hBN flakes on SiO_2.

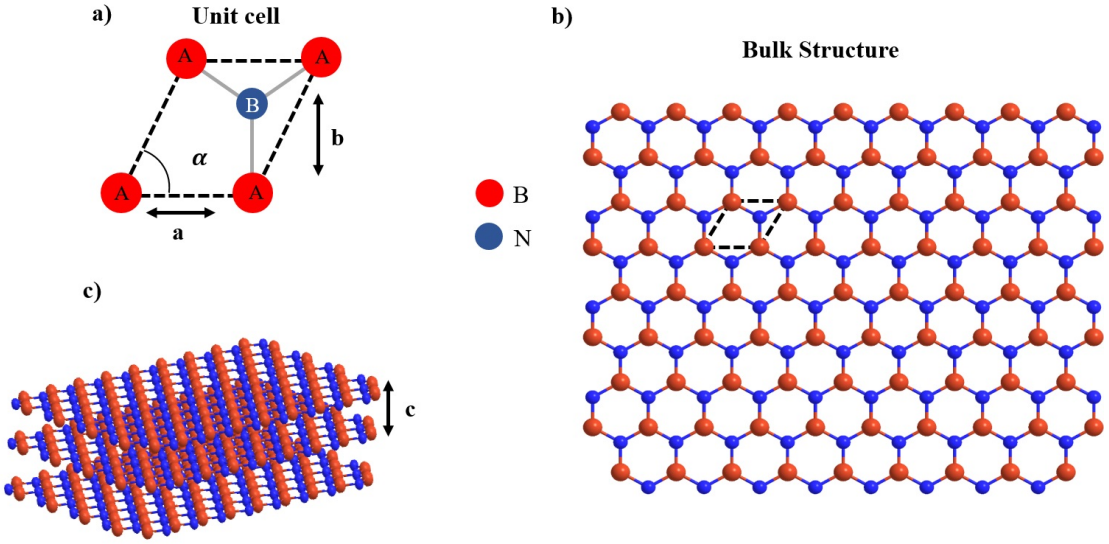


Figure 2.18: Hexagonal boron nitride (hBN) showing; a) length of the unit cell bond a= 0.252 nm, b = 0.145 nm, and the angle α= 60 °, b) the structure of the hBN sheet where the unit cell shown in a is marked with dashed black line, c) interlayer separation of hBN sheets is, c= 0.33 nm.

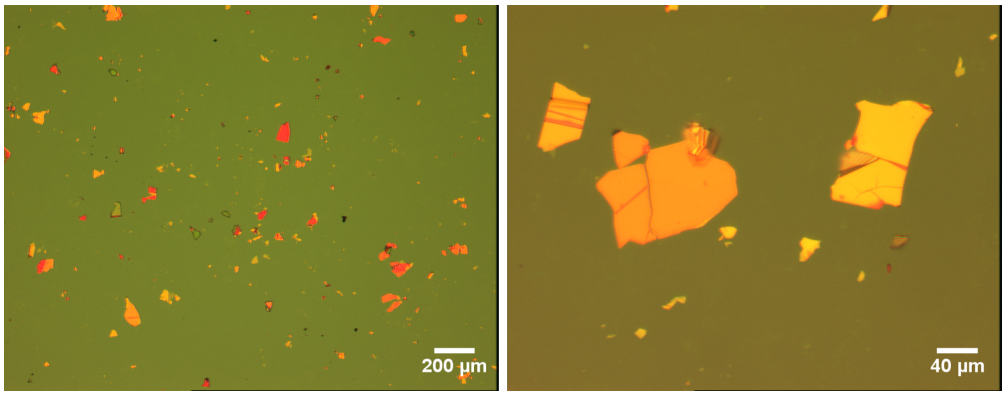


Figure 2.19: Optical microscopy images of hBN flakes deposited by mechanical exfoliation on 300 nm thick SiO_2 on Si wafer.

CHAPTER 3

Experimental techniques, methodology and sample preparation

Nanoscientists employ a wide range of imaging techniques to investigate the structure of materials at the nanometre scale. Such techniques have enabled unique investigations into the properties of structures in bulk materials and at the nano-scale. This chapter begins with descriptions of scanning tunnelling microscopy and atomic force microscopy including the theory behind their principles of operation. Optical microscopy and photoluminescence are discussed next, followed by a brief explanation of sample substrates and their preparation. Vacuum deposition systems are also described. The chapter concludes with a full description of heterostructure fabrication, stamp preparation, and flake alignment.

3.1 Scanning probe microscopy (SPM)

To explore structures at the atomic or molecular level, scanning probe microscopy (SPM) is widely used. SPM can provide high resolution images on the nanometre scale and can operate under atmospheric conditions, liquid, vacuum, and at different temperatures [83, 84]. Images are formed which depend on the interaction between a probe and the sample surface. In 1981 Binnig and Rohrer reported the invention of the scanning tunnelling microscopy (STM), which was the first SPM technology for which nanometre scale resolution was demonstrated [85]. The researchers were awarded the Nobel Prize in 1986 for this discovery. Although the STM is not the primary focus in this study, it laid the foundation for all scanning probe microscopies that were developed later. There is no doubt as to the importance of the STM instrument to science. However, it can only be used to image surfaces of conducting or semiconducting materials [86].

Soon after, in 1986, Binnig et al. addressed this limitation and the atomic force microscope (AFM) was developed upon the basis that recent STM advancements had made [87]. Since the birth of this innovation, the use of AFM has attracted not only physicists and chemists, but also biologists. The benefit that samples can be measured, which are either insulating or conducting, without special surface preparation, at ambient pressure, vacuum, or in liquid, is perhaps the greatest advantage for using AFM [88]. This instrument characterises the morphology, such as roughness or height distribution, of a sample surface.

3.1.1 Scanning tunneling microscopy (STM)

The STM is an instrument for imaging surfaces at the atomic level. STM scanning utilizes a flow of current, therefore it requires a conducting or semiconducting substrate. Quantum tunnelling is central to the concept of STM operation. When examining the sample surface, a conducting tip comes very close to the surface and a voltage difference is applied between the tip and the sample. The resulting tunnelling current depends on the tip position, applied voltage, and the localized states of the sample under investigation. A tunnelling current occurs when an electron has a finite probability of passing through a potential barrier. This is in contrast to a classical picture, where electrons are unable to move through a barrier because they do not have enough energy. This phenomenon can by analysed using the 1D (z direction in this case) time-independent Schrodinger equation [85]. The wave function,ψ, is shown in Equation 3.1

$$\frac{-\hbar^2}{2m}\frac{d^2\psi(z)}{dz^2} + V(z)\psi(z) = E\psi(z) \tag{3.1}$$

where $\frac{-\hbar^2}{2m}\frac{d^2\psi(z)}{dz^2}$ is the kinetic energy of the electron, $V(z)$ is the potential energy, E is the total energy of the electron.

In region (a) of Figure 3.1, the wave function for the electron has a solution of the form

$$\psi_T(z) = Ae^{i\mu z} + Be^{-i\mu z}$$

where $e^{-i\mu z}$ is the incident wave and $e^{i\mu z}$ represents the reflected wave, A and B are constants, and μ is the wave vector of the electron defined as $\mu = \sqrt{2mE/\hbar^2}$, where,m, is the electron mass.

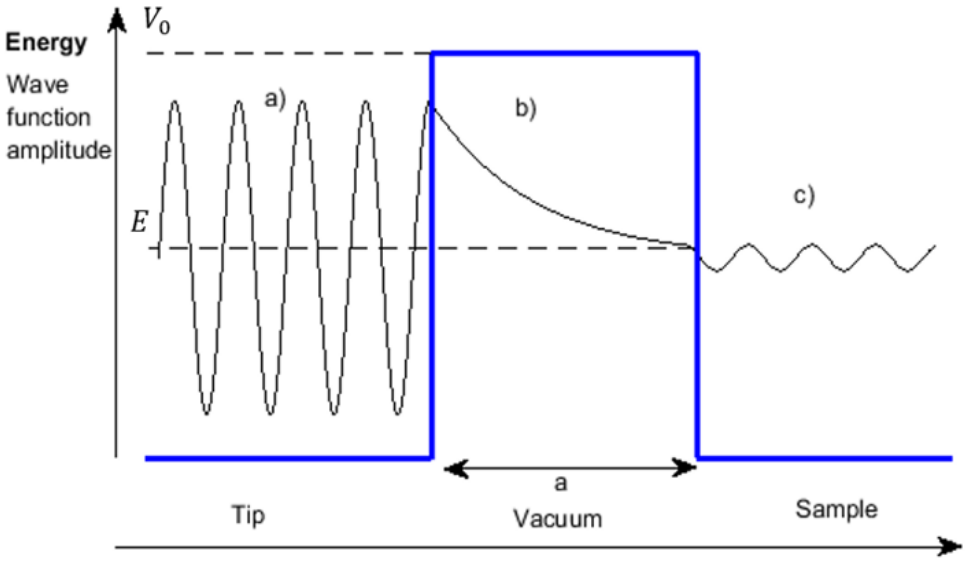


Figure 3.1: Schematic diagram showing a wave incident on a one-dimensional barrier taking the form in region: a) of a travelling wave, in region; b) an exponentially decaying wave function, and in region; c) a travelling wave.

In region (b) in Figure 3.1 (classically forbidden) the wave function has a solution of the form

$$\psi_{Barrier}(z) = Ce^{Kz} + De^{-Kz}$$

where,K, is the decay constant. We approximate,$K = \sqrt{2m(V_0 - E)/\hbar^2}$, where V_0, is the height of the potential barrier, and we assume V_0-E = φ, the work function defined as the minimum work or energy needed to extract an electron from the bulk to the vacuum level.

In region (c), the wave function has the form $\psi_S(z) = F\, e^{-i\mu z}$. This is the transmitted wave moving to the right. The electron has a finite probability to tunnel through the barrier given by T, the transmission coefficient which is the ratio between the transmitted wave (region c) and the incident wave (region a)

$$T = |\frac{F^2}{A^2}| = \frac{16K^2\mu^2}{(K^2+\mu^2)^2}e^{-2Ka}$$

Assuming $Ka >> 1$, $T \propto e^{-2Ka}$

From the equation above, the electron has a finite probability to decay exponentially through the potential energy barrier. Assuming that the tunnelling current, I, is directly proportional to the transmission coefficient

$$I \propto e^{-2Ka}$$

Taking typical values of work functions value for materials used in STM experiments the tunnel current changes by approximately one order of magnitude for every change of 0.1 nm between the tip-sample [85].

Figure 3.2 shows the aligned Fermi level for a tip-sample system for zero applied voltage where no tunnelling current flows through the tip-sample vacuum barrier.

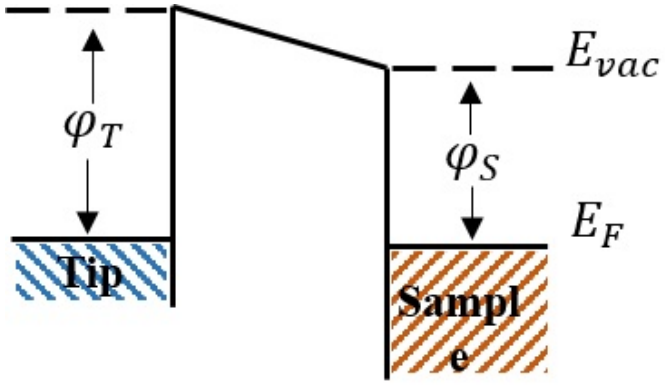


Figure 3.2: A schematic diagram showing and aligned Fermi level for both tip and sample (equilibrium condition) when no current flows between tip and sample.

A voltage bias is required to allow tunnelling current to flow between the tip and the sample [83]. In this case, if the sample is negatively biased, the electrons tunnel out of

the occupied sample states and into the tip. In contrast, if the sample is positively biased, the electrons tunnel into unoccupied states in the sample from the tip, as depicted in Figure 3.3.

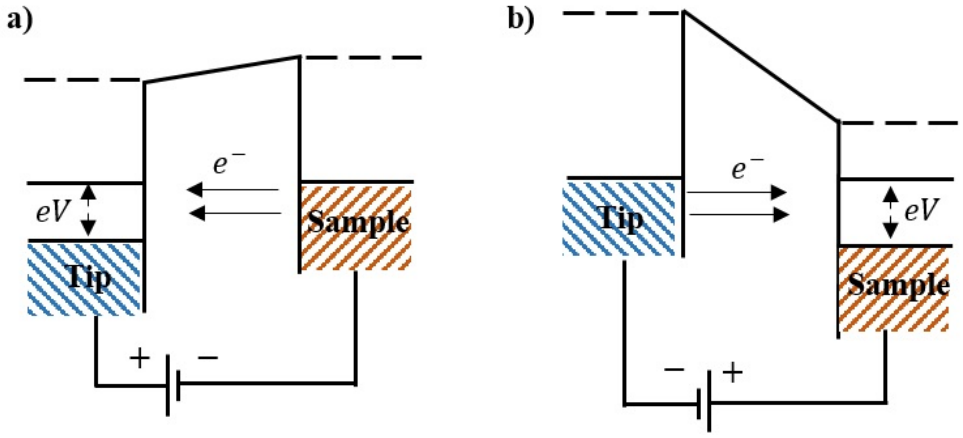


Figure 3.3: A schematic diagram showing when tunnelling occurs and electrons move from: a) sample to tip with a negatively biased sample; b) from the tip to the sample with a positively biased sample.

An STM consists essentially of three parts as shown in Figure 3.4. The first is an atomically sharp tip, usually made of Pt-Ir (Platinum-Iridium) or W (tungsten), formed by chemical etching or cut from a thin metal wire using a cutter. The second part of the STM is the piezodrive which is connected to the tip and typically composed of three perpendicular piezoelectric transducers; x-piezo, y-piezo and z-piezo. When experiencing a voltage a piezoelectric transducer contracts or expands, depending on the polarity of the voltage. The tip can scan across the x-y plane when applying a saw tooth voltage on the x-piezo (acting here as the fast scan direction) and a voltage ramp on the y- piezo (the slow scan direction). The final part is the base for the sample. All of them connect to a PC to provide visual feedback of sample topography [88, 89].

The following methods may be used to acquire images of the surface as shown in Figure 3.5. Firstly, in constant current mode, the piezo drive adjusts the height between the tip

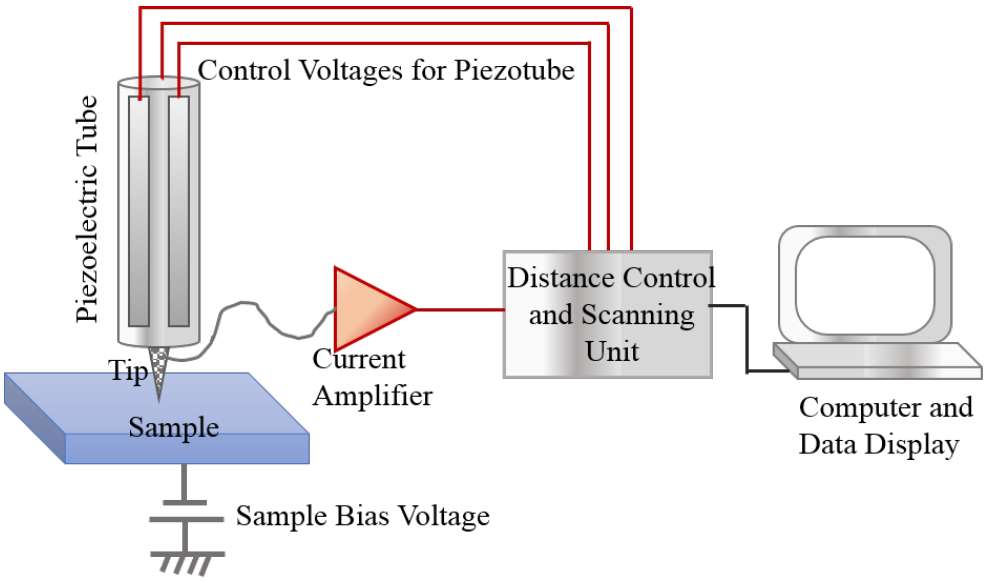


Figure 3.4: A schematic diagram for Scanning Tunnelling Microscopy (STM).

and the sample to keep the current constant. This means the tip will adjust its position as it moves across the surface resulting in a topographic scan of the sample as shown in Figure 3.5 (Left). Secondly, in constant height mode, the height of the tip does not change and the user records current variation across the surface. This method allows results to be collected quickly, because the piezodrive does not need to adjust the height of the tip. In other words, the tip is scanned parallel to the surface as shown in Figure 3.5 (Right).

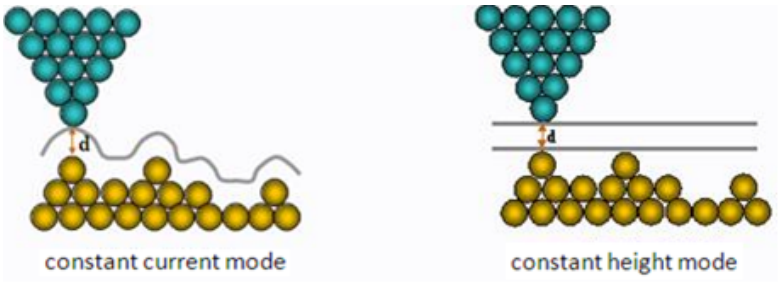


Figure 3.5: Diagrams illustrating the two STM modes of operation (Left) constant current mode or (Right) constant height mode.

An example STM topographic image is shown in Figure 3.6 (a and b) of cyanuric acid-melamine and highly ordered pyrolytic graphite (HOPG) respectively.

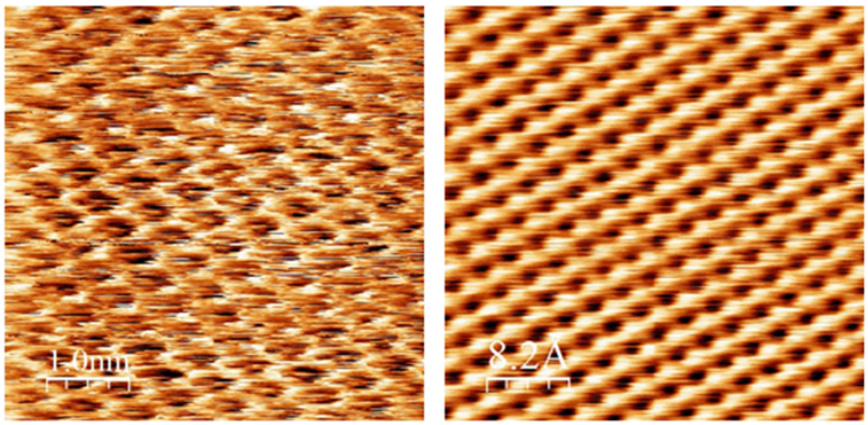


Figure 3.6: STM images of the first successful attempted of; a) cyanuric acid-melamine, and b) highly ordered pyrolytic graphite (HOPG).

3.1.2 Atomic force microscopy (AFM)

Although the STM provides extremely high resolution (up to atomic resolution), it has the significant limitation that it can only be used to image conducting or semiconducting surfaces. This limitation led to the invention of AFM by Binnig, Quate and Gerber [90, 91]. The primary advantage of the AFM is to acquire a topographic image of the surface by measuring forces between a sharp probe and surface with a nanometre scale probe-sample separation. The AFM measures the forces acting on the sharp tip of an AFM cantilever and the tip is scanned over the sample surface to generate a 2D image of the surface topography. Importantly, the AFM is compatible with insulating surfaces. The first AFM became available in 1989. Figure 3.7 depicts the Asylum Research MFP-3D, which was used in this work.

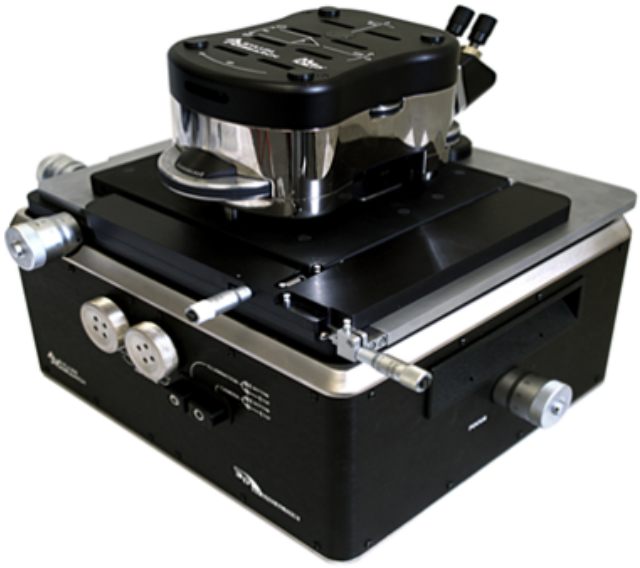


Figure 3.7: Asylum Research MFP-3D stand-alone, AFM unit used in ambient conditions [92].

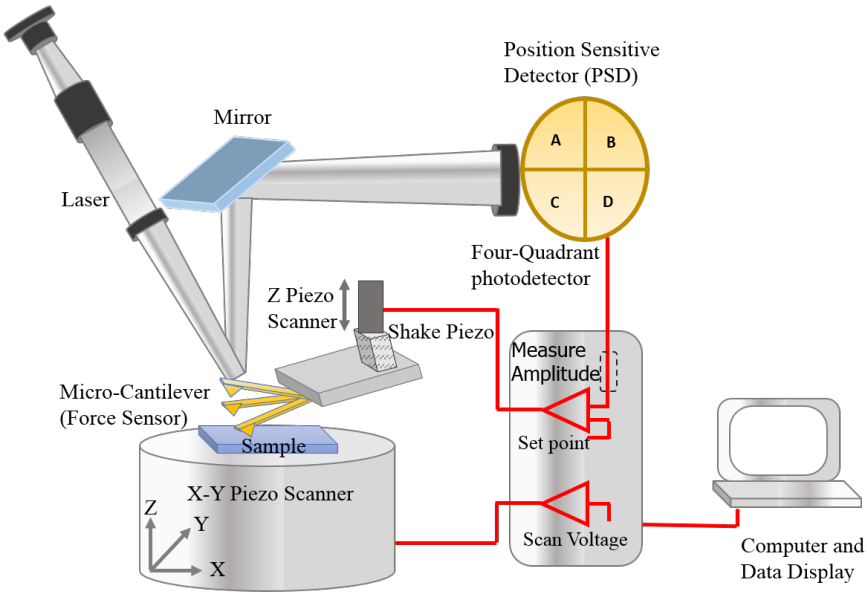


Figure 3.8: A schematic diagram showing the major components of an AFM

In contrast to STM, the AFM uses a more complicated system including a micro-tip connected to a cantilever (explained below) combined with optical deflection or fibre interferometry on piezoresistive materials to detect the tip deflection with nanometre scale precision. No current flow between the tip and the sample is required.

In this case, the AFM maps the surface topography by sensing attractive (including chemical, van der Waals (vdW), and electrostatic) and repulsive forces between a micro-tip on a cantilever and the sample surface. These forces have different effective ranges and magnitudes; depending on the tip-sample distance, the dominant force may change.

The vdW forces are ubiquitous and can arise from interactions between, two permanent dipoles (known as the Keesom interaction), a permanent dipole and an induced dipole (the Debye interaction), or induced dipoles (the London dispersion force). These long-range forces are caused by fluctuations of the dipole moment of atoms. The vdW interaction between two atoms separated by distance, r, scales as $1/r^6$.

The net interaction between the tip and the sample can be given as a combination of forces (attractive and repulsive) which obey a Lennard-Jones potential, approximating the interaction between tip and sample, and is given by

$$V(r) = E_0[(r_0/r)^{12} - 2(r_0/r)^6] \tag{3.2}$$

where,E_0 is the depth of the potential well and, r_0 is the point at which the potential reaches its minimum. The $(1/r^6)$ term describes the long-range attractive forces which, as the distance decreases will reach the equilibrium point where $V(r)$ becomes repulsive (Pauli repulsion) described as short-range by the $(1/r^{12})$ term. In Figure 3.9, a Lennard-Jones potential gives a simple representation of the relationship between the tip and sample.

To determine the vdW interaction between two nanoscale objects (tip and sample) taking account of all intermolecular interactions, a Hamaker approach can be used [93]. As shown in Figure 3.10 the interaction between a spherical tip of radius, R , at a tip-sample distance, r, and a semi-infinite surface can be calculated to give

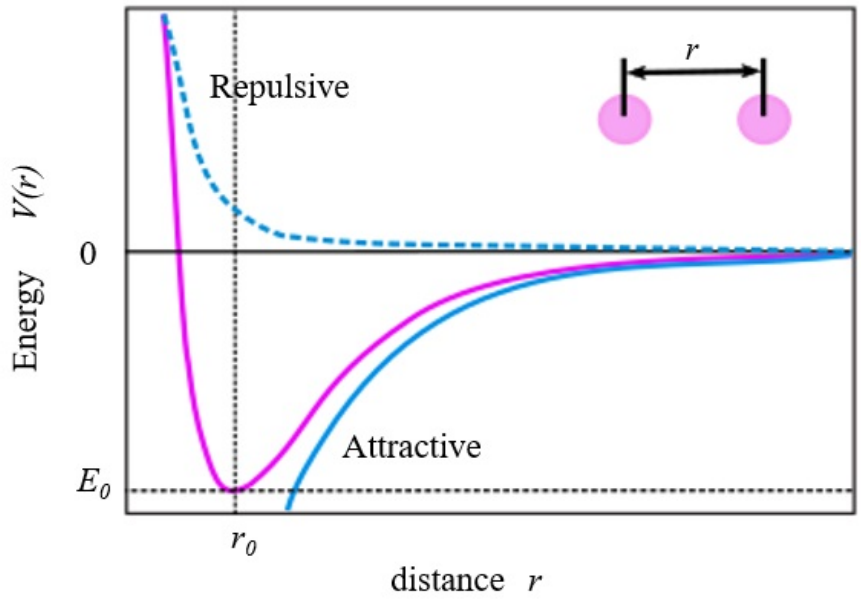


Figure 3.9: Lennard-Jones potential (solid pink line); repulsive (dashed blue line); and attractive (solid blue line) interaction between two bodies (tip-sample) separated by distance r as shown in inset.

$$F_{vdW} = -\frac{HR}{6r^2} \tag{3.3}$$

The AFM measurements can be implemented in two modes, based on measurement of either static cantilever bending resulting from the interaction force between the tip and the sample (static AFM or contact mode) or by using the resonant properties of the cantilever (dynamic AFM or non-contact mode).

3.1.3 Static AFM (contact mode)

In contact mode as the tip comes close to the surface, it will experience a net attractive force up to a certain point. Here the total force becomes repulsive due to Pauli exclusion or the Coulomb interaction. The displacement of the cantilever due to the tip-sample

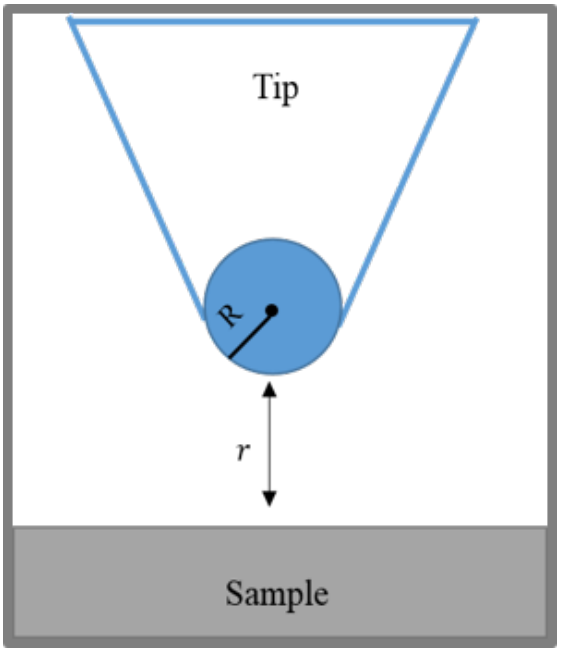


Figure 3.10: The tip-sample interaction for a tip with sphere of radius, *R*, at distance, *r*.

interaction (cantilever deflection) δ_z, is shown in Figure 3.11 and is proportional to the interaction forces between the tip and the surface [94].

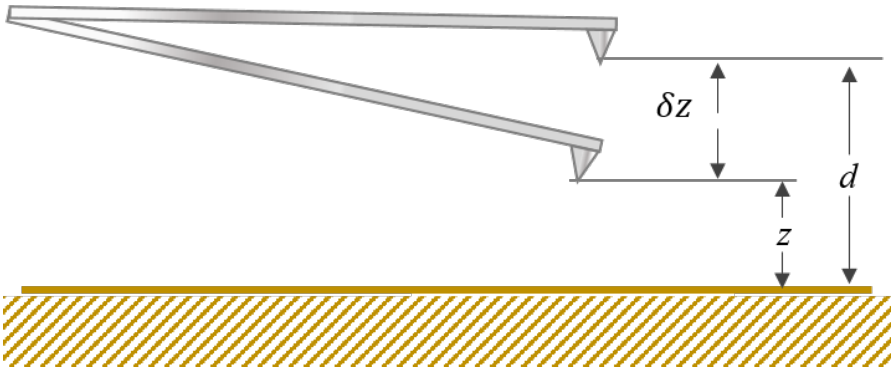


Figure 3.11: Shows the parameters of tip-sample distance for static AFM mode where, *z*, is defined as the tip-sample distance, d, is the real distance between the tip-sample, δ_z, the displacement of the cantilever due to the tip-sample interaction.

The cantilever deflection, δ_z, is determined by Hooke's law, as the force divided by its spring constant is given by

$$F(z) = -k\delta_z \tag{3.4}$$

where *F(z)*, is the tip-sample force,δ_z the deflection of the cantilever due to the tip-sample interaction. The cantilever spring constant is defined by $k = Ywt^3/4L^3$ where Y is the Young's modulus of the material and w, t, L are the dimensions of the cantilever.

The cantilever spring constant determines the cantilever sensitivity. It can vary from 0.1 to 100 N/m, depending on the cantilever shape and material. For low stiffness the cantilever has very high sensitivity and large bending. However, there is a limitation for low stiffness that the cantilever due to thermal fluctuations. To keep the cantilever deflection, δ_z, larger than the thermal fluctuations, the spring constant, k, must satisfy $k > k_B\ T/\left\langle \delta_z^2 \right\rangle$, where, T, is the temperature and, k_B, is the Boltzmann constant.

Static AFM images are simply a map of the surface height profile measured with a constant cantilever deflection, i.e. a constant force. Due to instability in the attractive regime where tips may snap to the surface, contact mode AFM is operated in the repulsive region. The stable position of a tip at any height above the surface can be derived by considering $\delta_z = d\text{-}z$ [94]

$$F(z) = k(z - d)$$

where, d , is the height of the undeflected cantilever. As shown in Figure 3.12 (a), with the tip far away from the sample (line 1), *F(z)* is close to zero at the intersection point, α. As the tip starts approaching the sample, the measurable value of the intersection point occurs at β for line 2 as δ_z is negative indicating an attractive force. At this point the cantilever is bent toward the surface and unstable as there are multiple solutions for line 2 (jump to contact). For line 3, with the intersection point, γ, the only solution

will be a positive value of the deflection which corresponds to repulsive force and a stable solution. Finally, as the tip is retracted (line 4), at the intersection point δ, there are multiple solutions. At this point the tip will separate from the sample (jump off contact). All these processes are shown in Figure 3.12 (b).

As a result, the final approach/retract tip movement toward the surface and vice versa (Figure 3.12 (b)) at line 2 and 4 show hysteresis due to instability occurring at different tip sample separation. It is dependent on the cantilever stiffness; when the cantilever stiffness is large, the lines in Figure 3.12 (a) will be steeper, reducing the unstable region and hysteresis.

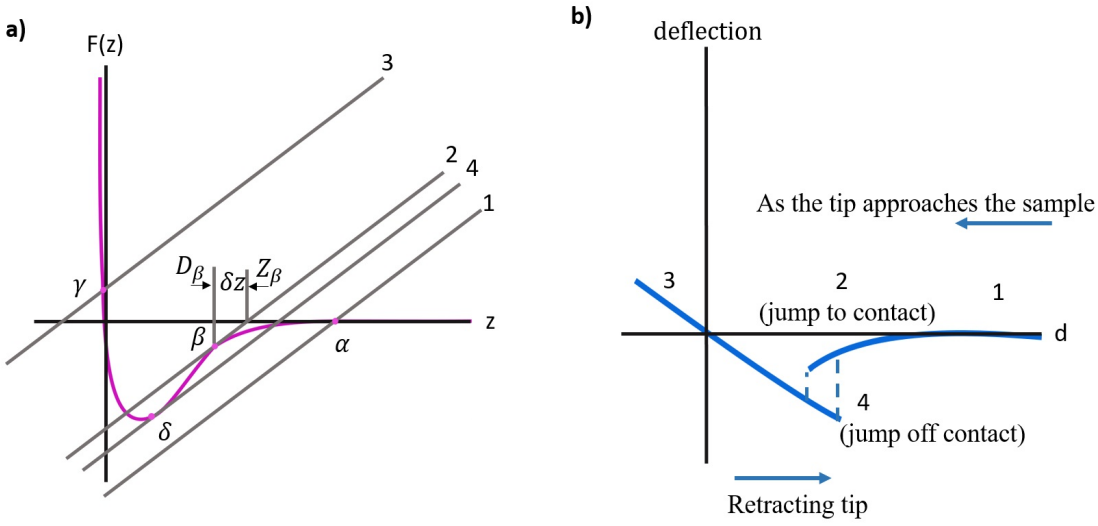


Figure 3.12: (a) the typical curve of tip-sample interaction force with intersections of lines 1-4 shown by $(\alpha, \beta, \delta, \gamma)$; (b) the interaction force as a function of distance z showing the jump to contact determined as δ_z in (a).

In contact AFM mode the tip is moved gradually towards the surface and the deflection is measured as a function of the tip displacement. In this case the surface may be deformed and damaged resulting from pressing the tip into the surface. When intentional, such an operation is referred to as nano-indentation lithography. In this

operation the tip is driven at a higher set point and the tip moved on the surface in predesigned pattern on a deformable substrate (e.g. a polystyrene coated glass slide). Then, the AFM can be operated in tapping mode to allow the resulting pattern to be imaged, as shown in Figure 3.13.

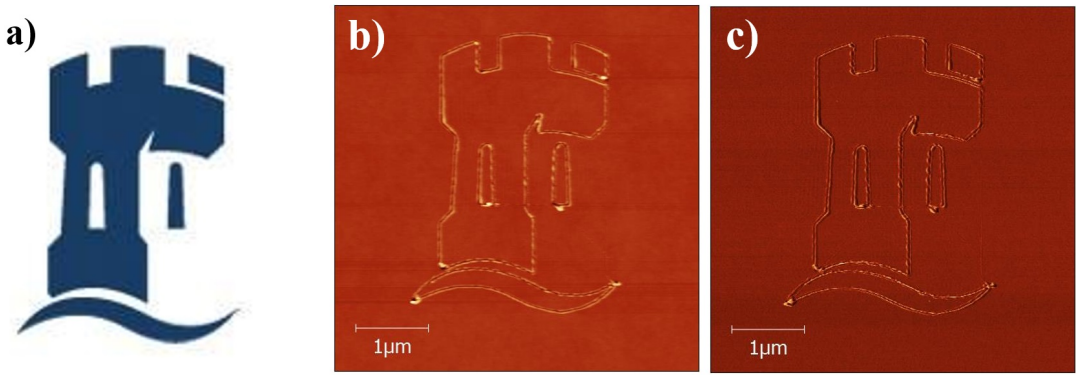


Figure 3.13: An example for one of AFM modes (contact mode) of nano-indentation lithography using a thin spin coated film of polystyrene on a glass slide: (a) University of Nottingham logo which is used as an input image to generate a path for the AFM tip to trace; (b) and (c) tapping mode height retrace and phase retrace respectively.

3.1.4 Dynamic AFM (non-contact mode)

In the non-contact AFM mode (NC-AFM) of operation the cantilever is treated as a resonant system allowing one to estimate the interaction between the tip and the sample from a change in the resonant frequency of the cantilever. The force gradient is measured in this approach rather than the force. The cantilever is excited by applying an oscillating voltage to a piezoelectric transducer when the cantilever is in close proximity to the surface of the sample. This can be understood by modelling the system as

a 1-dimensional driven harmonic oscillator [94–96] as shown in Figure 3.14, so can be described the system by

$$m\ddot{z} + \gamma\dot{z} + k(z - d) = F(z) + F_0 \cos(\omega t) \tag{3.5}$$

where m is a constant related to the cantilever mass, γ is the damping of the system (γ= $m\,\omega_0/Q$ where Q is the quality factor of the cantilever) and ω_0 is the cantilever resonant frequency. The $F_0 \cos(\omega t)$ term is the driving force, F_0 is the amplitude and ω is the angular frequency of the drive signal. Assuming that the tip is away from the surface and there is no interaction between the tip and the sample, F(z)= 0.

In the absence of the driving force, the cantilever undertakes a static deflection so that the condition $F(z_0) = k(z_0 - d)$ is satisfied as explained in the previous section. The time dependence can be modelled by considering small oscillations around the equilibrium position so that $z \to z_0 + z'(t)$ which gives

$$F(z) \approx F(z_0) + z'(t)\frac{dF}{dz} + ... \tag{3.6}$$

Substituting into Equation 3.5 and simplified to gives

$$m\ddot{z'} + \gamma\dot{z'} + (k - \frac{dF}{dz})z'(t) = F_0 \cos(\omega t) \tag{3.7}$$

This is the equation for a driven oscillator with a modified spring constant of $k_{eff} = k - \frac{dF}{dz}$ which results in a modified resonant frequency

$$\omega_0(z) = \sqrt{\frac{k_{eff}}{m}} \approx \omega_0 - \frac{\omega_0}{2k}\frac{dF}{dz} \tag{3.8}$$

There is a shift in resonant frequency which is proportional to the force gradient in the limit $k \gg \frac{dF}{dz}$

$$\Delta\omega_0(z) \propto -\frac{dF}{dz} \tag{3.9}$$

This shift can be measured using two approaches either amplitude modulation (AM-AFM) or frequency modulation (FM-AFM).

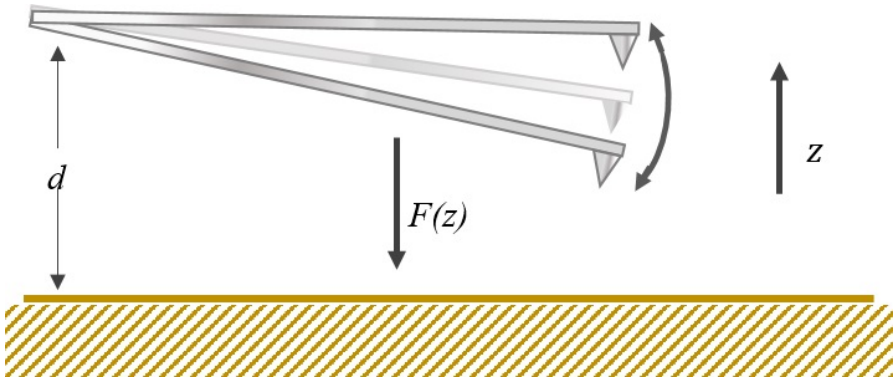


Figure 3.14: Shows the parameters of tip-sample distance for dynamic AFM mode where the cantilever is undergoing oscillatory motion.

Amplitude modulation (AM-AFM)

In non-contact AFM mode (NC-AFM), the principle of operation of AM-AFM occurs when the cantilever tip is oscillated near its resonant frequency with $\omega = \omega_d$, a fixed frequency as shown in Figure 3.15. When the tip is near the surface, the interaction causes a change in the amplitude and the phase of the cantilever. The vibration amplitude is used as the feedback signal for topographic imaging in order to keep the tip-surface distance constant by changing the height of the tip with a piezoelectric actuator.

The change of the amplitude of oscillation occurs on a time scale, $\tau_{AM} \approx \frac{2Q}{f_0}$, which is dependent on the quality factor, Q, where f_0 is the resonant frequency. This is considered a disadvantage to AM-AFM as it limits the possible scan speed.

When the cantilever is in vacuum and the quality factor of the cantilever is very high, a very slow scan speed must be used for the feedback mechanism to work properly [95].

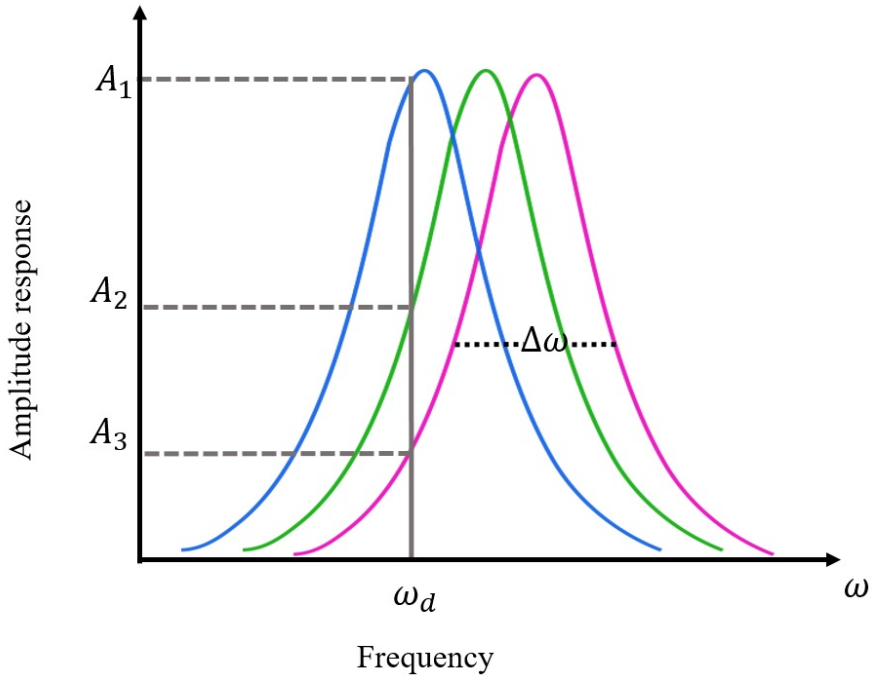


Figure 3.15: Shows the change in vibration amplitude induced by the frequency shift where A_1, A_2, A_3 are the measured amplitude at fixed drive frequency,ω_d. The dashed line labelled as $\Delta\omega$, represents the full width at half maximum which is related to Q, the quality factor of the cantilever.

Frequency modulation (FM-AFM)

In FM-AFM the amplitude is not measured directly. The cantilever is driven with fixed amplitude at its resonant frequency. Then, the frequency is observed by measuring the phase response,$\varphi(\omega)$, of the cantilever which is described as in Equation 3.7 relative to the driving term.

$$z'(t) = z'_0(\omega)\cos(\omega t - \varphi(\omega)) \tag{3.10}$$

where $\varphi(\omega)$, is the phase lag between the response and the driving term, and $z'_0(\omega)$ is the amplitude of oscillation. The FM-AFM method is often preferred, because the time scale response, in contrast with AM-AFM method, is faster where f_0, is the resonant frequency.

$$\tau_{FM} \approx \frac{1}{f_0}$$

3.2 Impact of AFM tip termination

AFM has different limits of resolution depending on the directions of scanning process, vertical and lateral. The resolution for scanning in vertical direction is restricted by the slightest change in the strength of the surface interaction the cantilever could detect. This is related to mechanical and thermal noise present in the system as well as sensitivity of the probe. Meanwhile, lateral resolution limit is based on the radius of the tip curvature. The images will be broadened significantly when lateral features are of same size or smaller than the radius of the tip curvature.

In general, it is not possible to track state of the tip used during AFM measurements carried out under ambient conditions. Specifically, interactions between the tip and the sample could lead to the presence of material at the tip apex which could change during imaging.

3.3 AFM cantilever configurations

Similar to STM, AFM also uses a sharp tip to map the topography of the surface. A probe, referred to a micro-cantilever, provides a force sensor and a force actuator. The micro-cantilevers that were used in this work (Multi75Al, Multi75Al-G) are commercially available from Budget sensors. This cantilever is important and very crucial to effective and efficient AFM operation. The cantilever is micro manufactured using the technologies used to fabricate integrated circuits such as photolithography and etching procedures. Most AFM micro-cantilevers are made of either silicon or silicon nitride. The upper side of the cantilever can be coated with a metallic film to optimise reflection of the optical lever. The micro-cantilever design can either be V-shape or rectangular, depending on the intended use. It has a wide range of properties designed for different application purposes. Figure 3.16 shows an optical image of a micro-cantilever with its nanoscale tip. The Multi75 probe that has been used in this work is shown in Figure 3.17, the typical dimensions of the chip holder are 1.6 mm, 3.4 mm, and 0.3 mm for width, length, and thickness respectively. The probe has typical dimensions of 28 μm, 225 μm, and 3μm for width, length, and thickness.

3.4 Optical microscopy

Optical microscopy is a useful tool that uses visible light and a system of lenses. The basic principle of the optical microscope is shown in Figure 3.18.

The resolution limit of optical microscopy depends on the wavelength of light used, and for visible light the wavelength (λ) ranges from 390 nm to 700 nm [97] . The maxi-

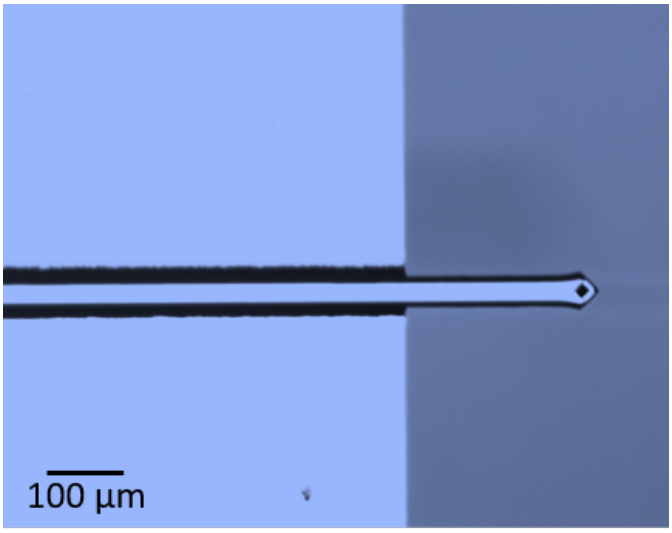


Figure 3.16: Optical image of a micro-cantilever with attached probe that used in this work.

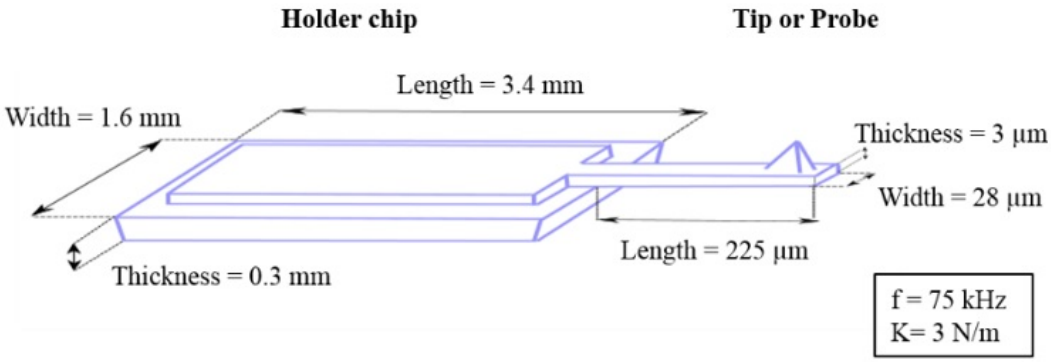


Figure 3.17: Schematic diagram of Multi75 probe and chip holder and associated geometry for the cantilevers used in this study. The probe has a radius less than 25 nm.

mum achievable spatial resolution, or the minimum separation of two distinguishable features ($\Delta\chi_{min}$), can be calculated using the Rayleigh criterion (Equation 3.8)

$$\Delta\chi_{min} = \frac{1.22\lambda}{n\sin\theta} \tag{3.11}$$

Here n, is the refractive index of the medium through which the light propagates and θ is half the angle from which light can enter the lens [98]. This form of microscopy uses an objective and eyepiece lens to resolve the object and create a virtual image of the sample. In this process, the sample is illuminated with white light through the objective lens, which is used in both illumination and imaging. The light is reflected and transmitted by the glass reflector, which is placed in the optical path at 45°. When the light interacts with the object, some of it is adsorbed, scattered and reflected, depending on the interaction. A fraction of the light that has interacted with the object then passes through the imaging lens system, which is used to give clear visual images of the object.

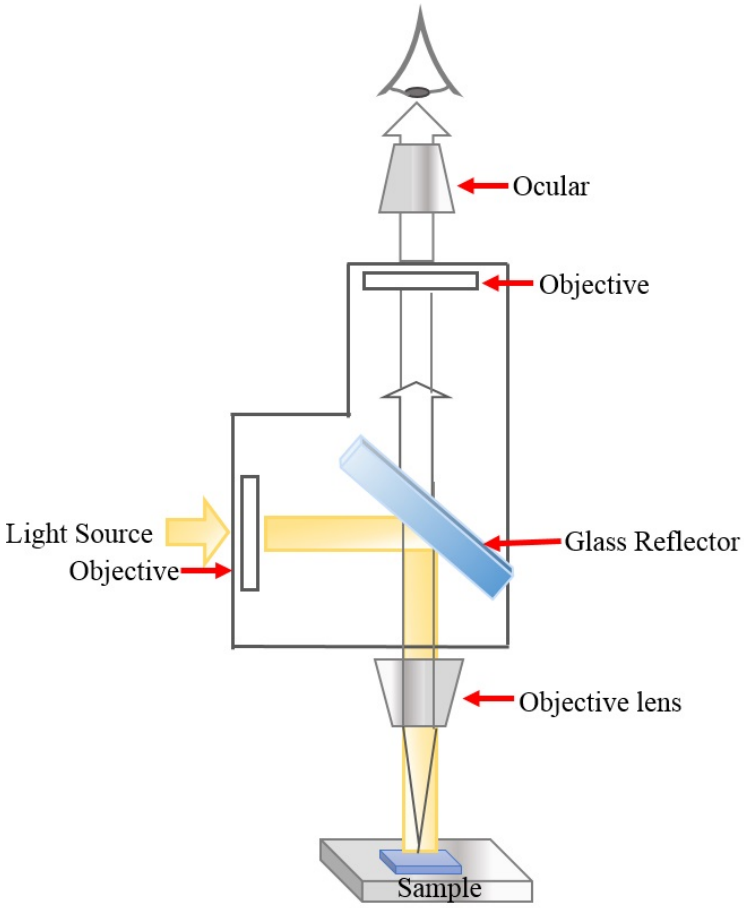


Figure 3.18: A schematic diagram of an optical microscope

3.5 Fluorescence

Fluorescence occurs for materials which absorb light at a particular wavelength and emit this light with a longer wavelength [99, 100]. The emission of photons resulting from an electronic transition can be detected. In a photoluminescence microscope as shown in Figure 3.19, an electron absorbs and is excited into a higher electronic state. Then the molecules lose energy by relaxing to the lowest singlet excited state. When the electron returns to the ground state a photon is emitted and its wavelength can be measured. The basic principle of fluorescence can be illustrated using a Jablonski diagram as shown in Figure 3.20. Since the technique of fluorescence spectroscopy relies on the interaction of light (as well as infra-red and ultra-violet radiation in some cases) it is compatible with conventional optical microscopy and is often incorporated into the same system in order to generate fluorescence spectra from a small, selected area of the sample and also to map spectra across the sample surface by rastering the laser spot used to excite the sample.

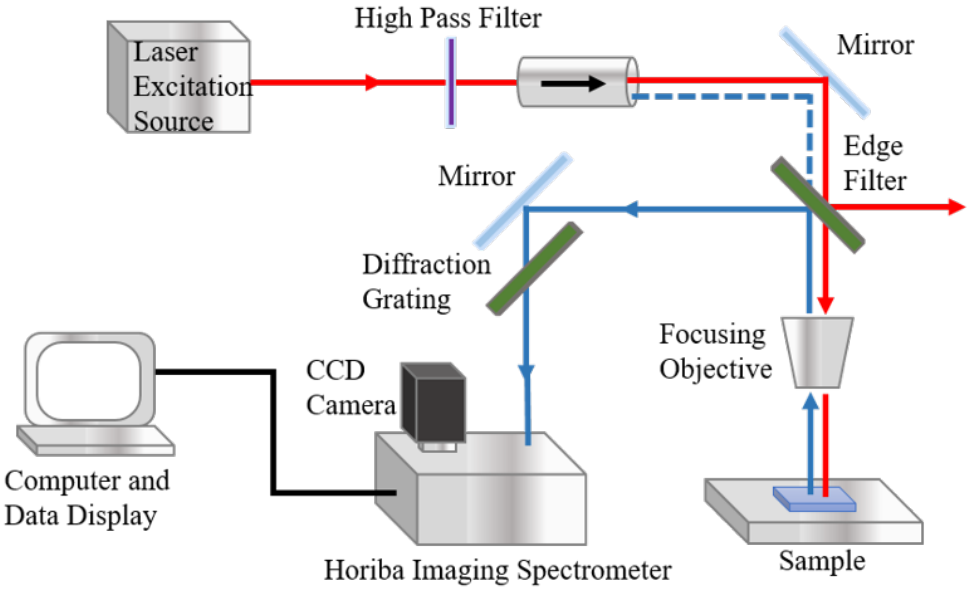


Figure 3.19: Schematic diagram of photoluminescence microscopy.

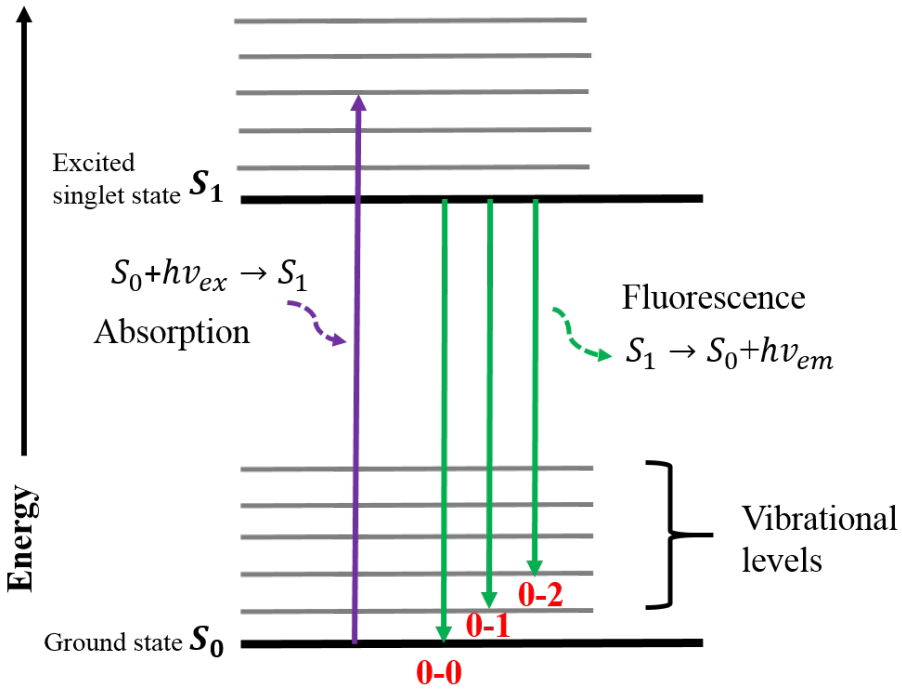


Figure 3.20: Fluorescence spectroscopy is used to measure the transitions from an excited electronic state to the electronic ground state.

In this work, fluorescence measurements were acquired using both Horiba LabRAM (excitation wavelengths: 325, 532, and 660 nm) and Horiba Micos (excitation wavelength: 405 nm) systems, both of which use an objective lens to project a laser spot 1-2 microns in size onto the substrate and collect the subsequent photoluminescence signal as shown in Figure 3.21.

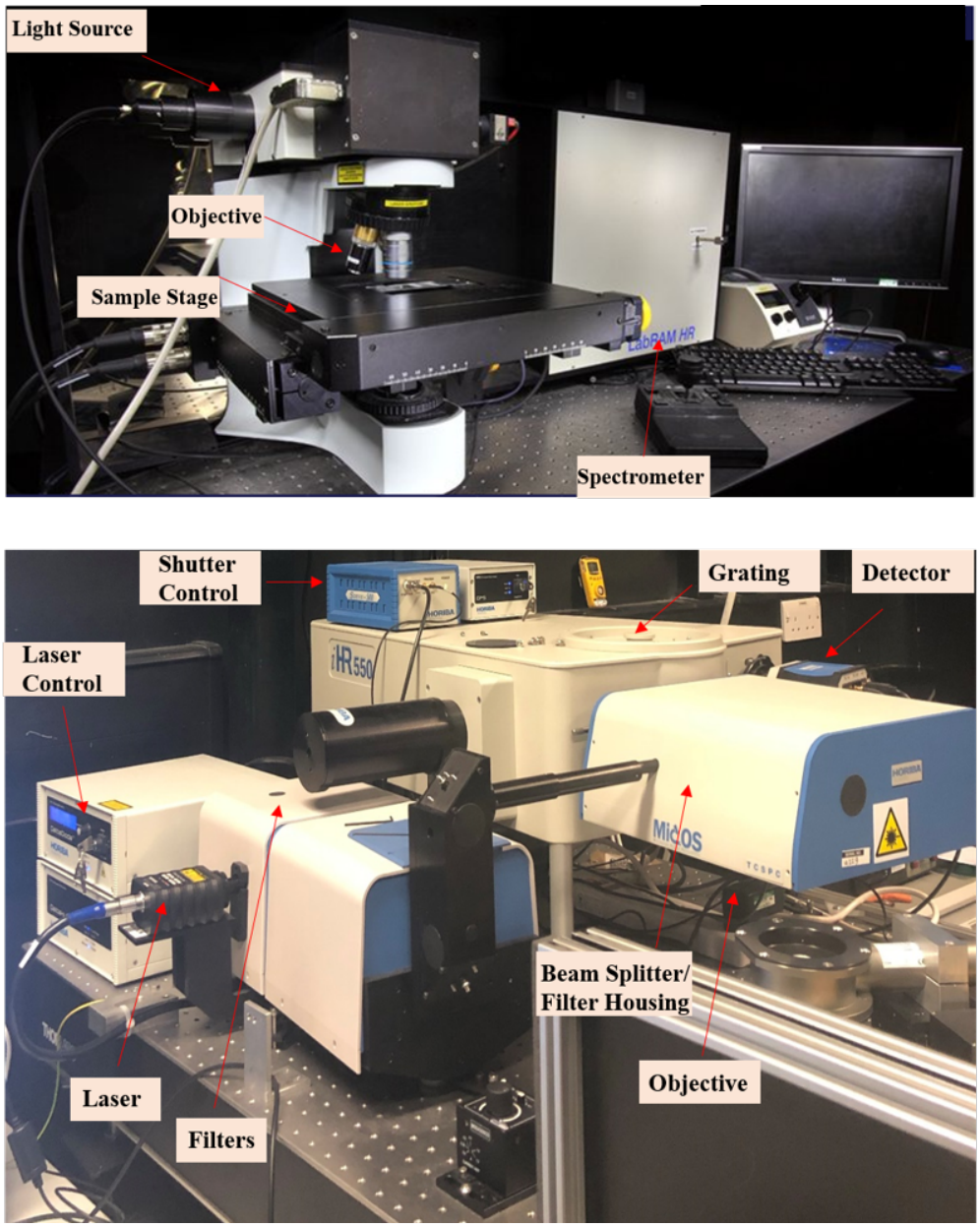


Figure 3.21: The fluorescence spectroscopy systmes used in this study; Horiba LabRAM (top) and, Horiba Micos (down).

3.6 Sample preparation

3.6.1 SiO_2 substrate

In this work, hBN flakes are exfoliated onto a Si/SiO_2 substrate (see section 3.4.2). The Si/SiO_2 wafers are purchased from Si-Mat silicon and have a 300 nm film of SiO_2 ther-

mally grown on a polished silicon substrate. This wafer was then scribed to a specific size (eg 5mm x 5mm chips). These substrates were then cleaned using the following solvents: ethyl lactate, acetone, methanol and isopropanol in an ultrasonic bath for 7-10 minutes each. After drying the substrates using a nitrogen gun, they were checked by optical microscopy to make sure there was no contamination on the surface.

3.6.2 Exfoliated hBN

In order to transfer hBN flakes onto these substrates, hBN crystals were placed on a strip of sticky tape. The strip with attached hBN flakes was then applied onto the surface of a clean SiO_2 substrate and pressed down carefully. The tape was then removed very slowly to leave a number of flakes adhering to the SiO_2 surface. When the tape is removed, the SiO_2 chips with hBN flakes were immersed in toluene for 24 hours to remove any residual organic material. After 24 hours, the samples are removed from toluene and dried using a nitrogen gun. Figure 3.22 outlines this preparation process. The substrates are then placed in a quartz tube furnace at 400°C for 8 hours in flowing H_2/Ar (5:95), to remove any residual organic contamination from the hBN surfaces. The furnace tube is shown in Figure 3.23.

Finally, to measure the topography of the sample surface and to observe any contamination, optical microscopy and AFM are used.

3.7 Vacuum deposition system

In this study films of organic semiconductors are deposited by sublimation in a vacuum deposition system. This approach was used to provide high quality molecular thin films. Two vacuum systems were employed in this work to perform thin film sub-

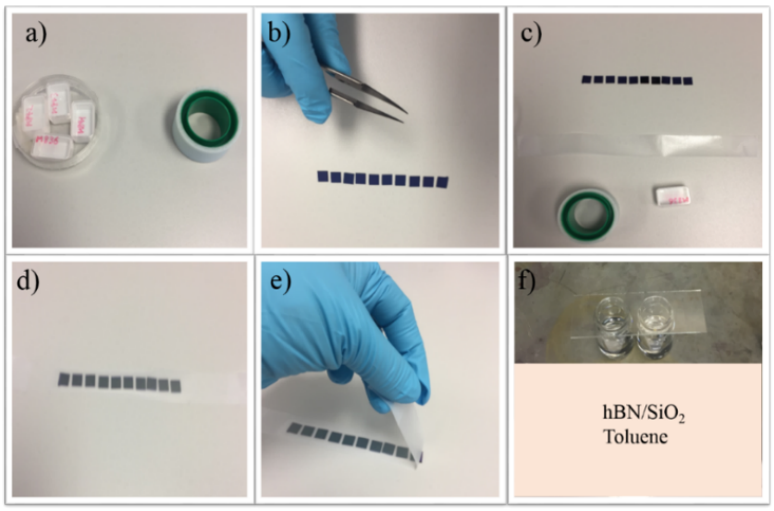


Figure 3.22: The steps of producing clean hBN on SiO_2 are shown above: (a-c) hBN crystal is placed on adhesive tape and exfoliated; (d,e) the tape is applied to SiO_2 and removed from the surface very slowly leaving a number of hBN flakes; (f) the hBN on SiO_2 substrates are immersed in toluene for 24 hours then removed and dried with a nitrogen gun.

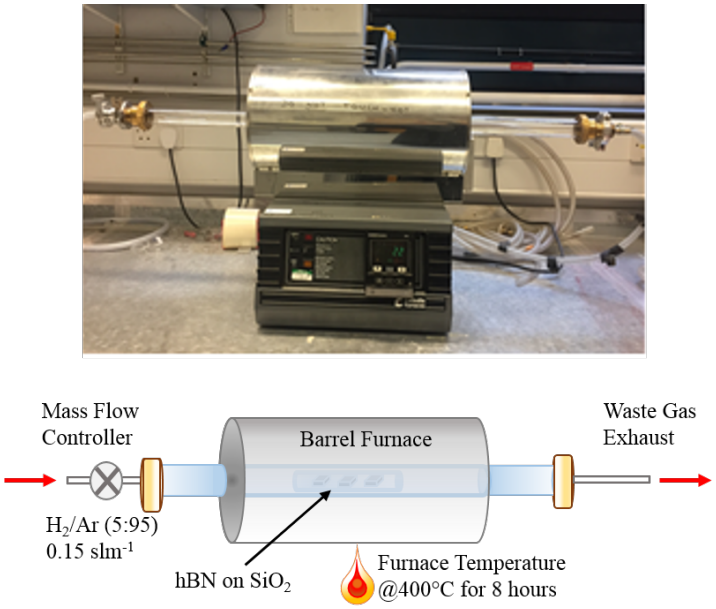


Figure 3.23: Substrates are loaded into the barrel furnace for annealing process in H_2/Ar gas.

limation as shown in Figure 3.24 and Figure 3.25. In general, both systems work with the same principle, but one system has a turbo pump with a base pressure of 1x10^{-7} mbar (Figure 3.24), whereas the other has an ion pump with a base pressure of 1x10^{-8} mbar (Figure 3.25).

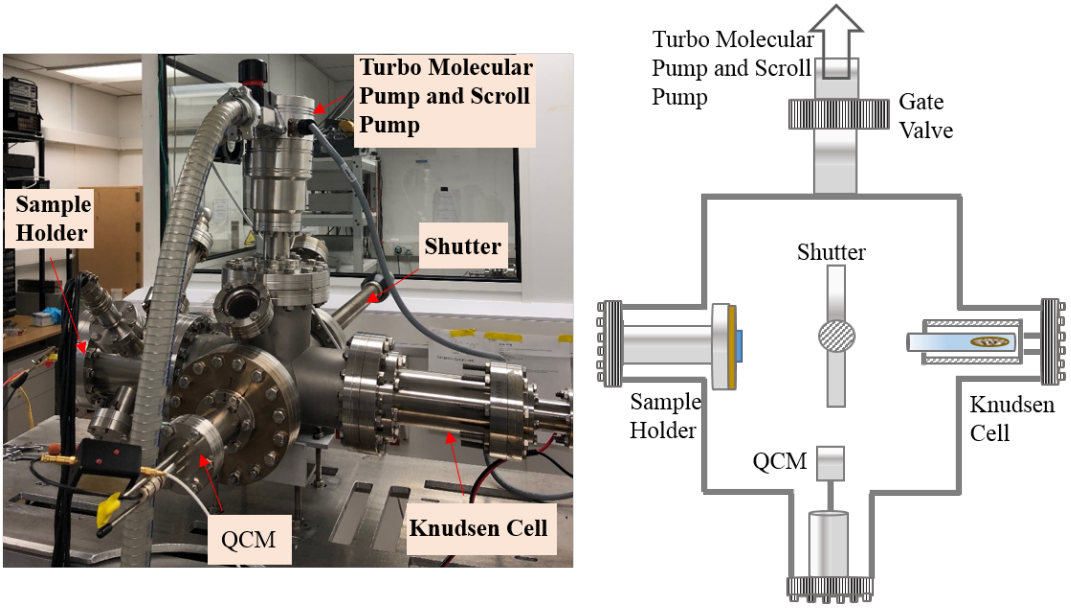


Figure 3.24: schematic diagram of the vacuum deposition system.

The organic material to be deposited is placed in a quartz crucible that is surrounded by a heater element and a heat shield in a Knudsen cell (K-cell). The temperature of the K-cell is controlled by an external power supply unit. The substrate temperature is monitored by a K-type thermocouple and heated before deposition to around 540°C to remove any adsorbed material on the surface. When the molecular deposition rate was stabilised at the required value, a shutter was opened and molecules sublime onto the sample. The molecular deposition rate was monitored by a quartz crystal thickness monitor alongside the sample holder. The shutter was opened once the deposition rate reached the required level. Figure 3.26 depicts schematics of (a) the sample holder, and (b) the K-cell.

For each molecular species, a thick molecular film >10 nm, was deposited onto a 300 nm SiO_2 substrate with the substrate partially covered by a shadow mask. The step height of the film at the mask edge was extracted from AFM images and used to calculate a tooling factor, the absolute thickness of material deposited on the substrate per thickness as measured by the QCM.

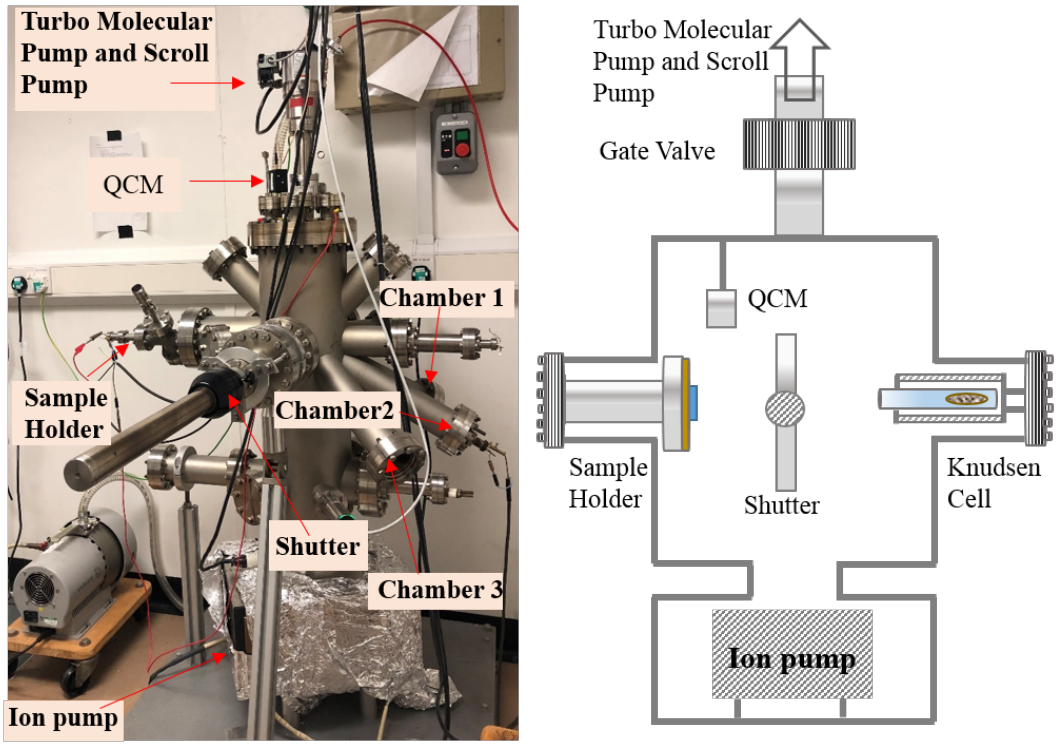


Figure 3.25: Schematic diagram of the vacuum deposition system with ion pump.

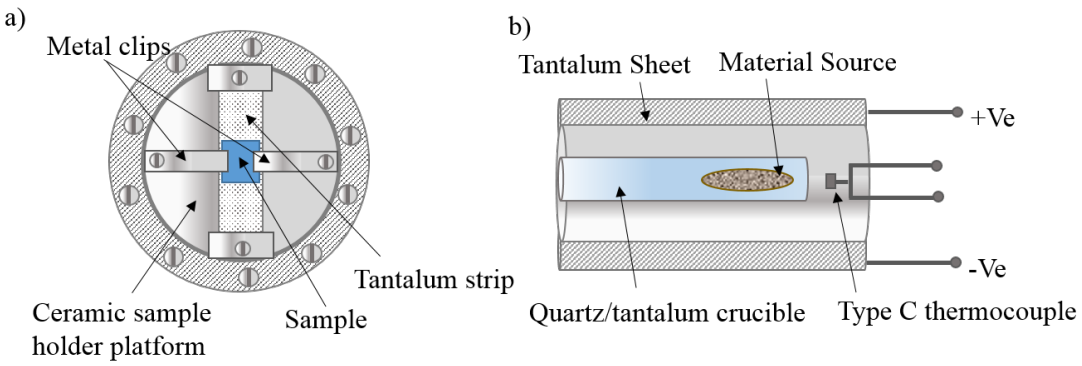


Figure 3.26: General schematic diagram of a) sample holder; b) K-cell

3.8 Heterostructure fabrication using stamping

To pick up exfoliated flakes of hBN, graphene, or other 2D materials and deposit them at a specific location on a substrate, stamping techniques were used. In this study heterostructures were fabricated using a stamping process.

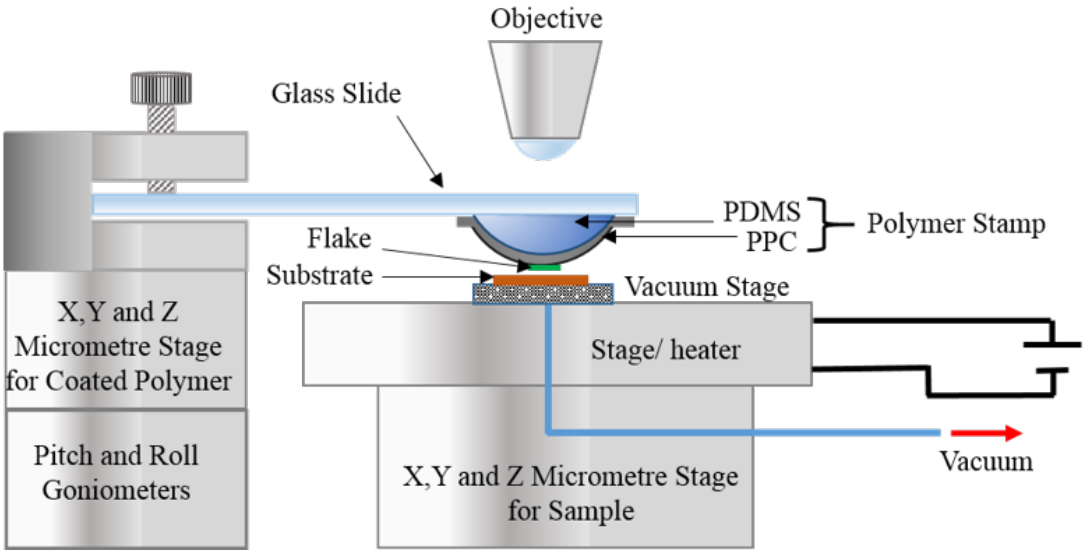


Figure 3.27: The stamping apparatus outline is depicted where the sample is placed on a micrometre stage with x,y and z motion, connected to a heater and vacuum chuck. The polymer stamp is clipped facing down, above the sample with its own micrometre stage to fully control the alignment. The sample and the polymer stamp can be viewed using the optical microscopy objectives above them.

hBN flakes were exfoliated onto a Si/SiO_2 wafer (SiO_2 thickness 300nm) and flame annealed before being placed on a micrometre stage. This stage is equipped with a vacuum chuck to hold the substrate in place and it is connected to a heater to control the substrate temperature. A polymer stamp composed of a polypropylene carbonate (PPC) film on a polydimethylsiloxane (PDMS) dot on a glass slide is used to pick up the chosen material. The preparation of the stamp is described later in section 3.7.1. The stamp is placed facing down and positioned above a target substrate on another micrometre stage. The micrometre stages are equipped with *x*,*y* and *z* direction movements and different optical microscope objectives for more precise alignment. The configuration of a stamping apparatus is shown in Figure 3.27.

3.8.1 Polymer stamp preparation

To prepare the polymer coated stamp, a mixture of PDMS elastomer and curing agent are used. The components are mixed at a 10:1 (elastomer:curing agent) ratio. The mixture is allowed to settle for 10-15 minutes at room temperature to let air bubbles escape. Following this, a drop of the mixture is placed on top of the microscope glass slide. Then the glass slide is placed in a furnace at 110 °C for 10 minutes. Once the glass slide has cooled down, it is exposed to an O_2 plasma for 3 minutes at room temperature. Immediately, and before taking the glass slide out of plasma chamber, PDMS is coated with a solution of PPC using a pipette. Next, the glass slide is placed on a hotplate at 80°C for 5 minutes to dry. This flat contact area and transparency are crucial in allowing the hBN flake to be aligned during the stamping process [101, 102]. Once it has cooled down, it is ready to use. These processes are shown in Figure 3.28.

3.9 Summary

This chapter provide a summary of techniques that are used in the remaining chapters in this thesis. Firstly, the principles of SPMs are described including the theory behind both STM and AFM. Optical microscopy and photoluminescence are then introduced. Then, the sample substrate of hBN preparation is explained in addition to a brief description of vacuum deposition system which was used for organic thin films growth by sublimation in UHV. Heterostructure fabrication, and stamp preparation are finally described.

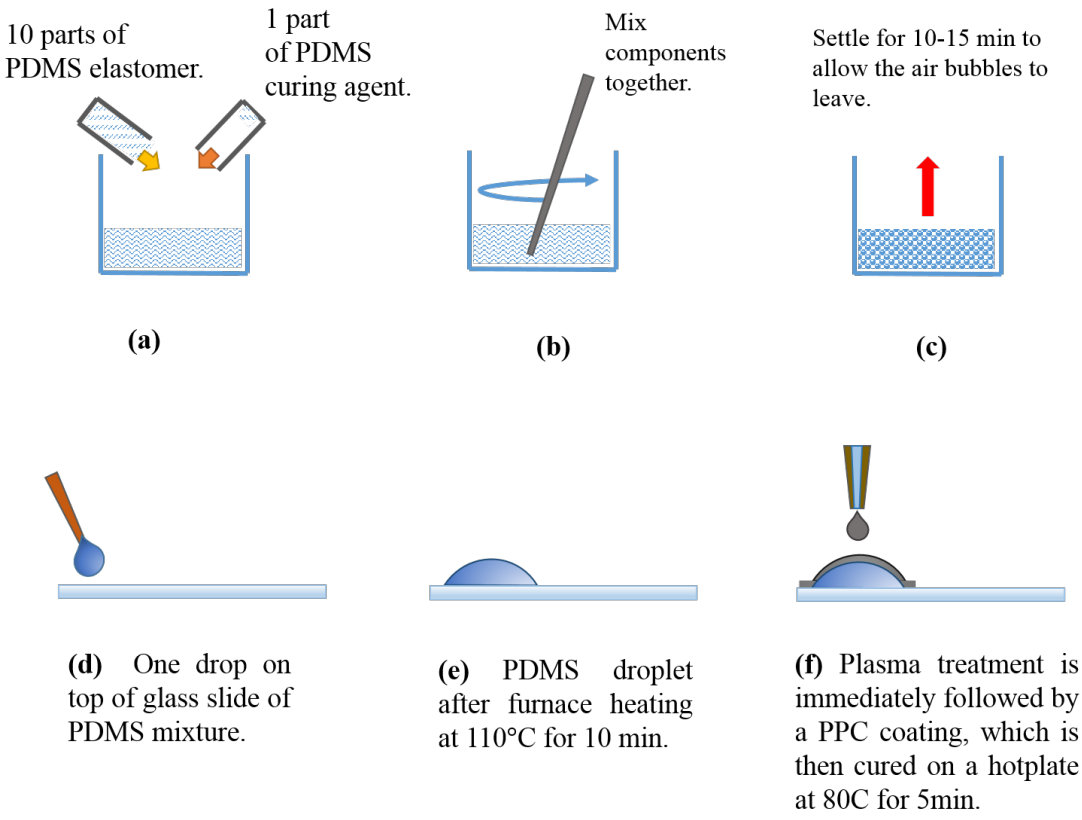


Figure 3.28: Process steps for PDMS stamp preparation and coating with PPC adhesive polymer on glass microscopy slide.

CHAPTER 4

Phthalocyanine on hexagonal boron nitride

The structural and functional properties of organic materials is an area of great interest within supramolecular chemistry and material science [9, 103]. In this chapter the influence of surface organisation on the fluorescence of free-base phthalocyanine (H_2Pc) is investigated. Phthalocyanines, both free-base and metallated variants, as shown in Figure 4.1 (a and b), are widely exploited in organic electronics and gas-sensing, and represent a prototypical example of an organic semiconductor on which many fundamental studies have been undertaken [41–45, 104–108].

In this chapter, the deposition of H_2Pc and zinc phthalocyanine (ZnPc) onto hBN/SiO_2 by sublimation will be discussed. The morphology of H_2Pc on hBN will be shown for sub-monolayer coverages grown at room temperature. The growth of H_2Pc thin films will then be discussed in two sets of results: firstly, a set of samples which were grown at room temperature with varying film thicknesses from 1 nm to 32 nm; then a series of samples grown at different substrate temperatures, ranging from room temperature

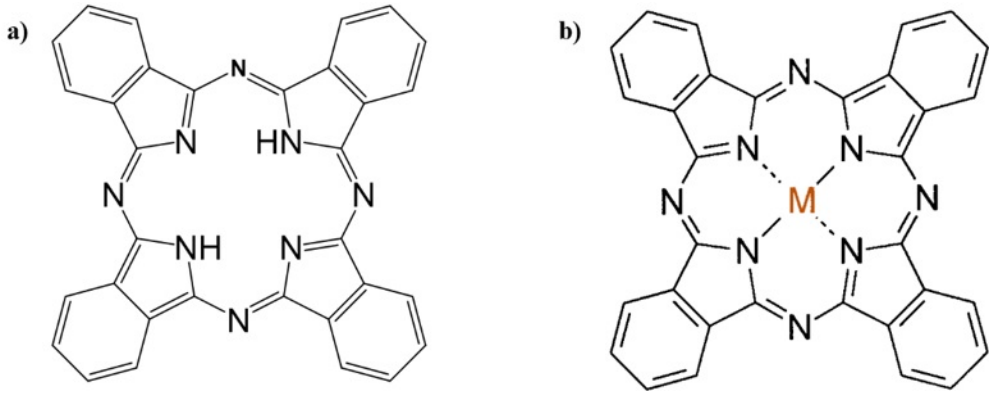


Figure 4.1: The chemical structure of: a) free-base; b) metalled phthalocyanine where M= Fe, Ni, Zn, Co, Mn.

up to 520°C. For all samples, the deposition rate was fixed at 0.5 monolayers/min. Finally, the growth of ZnPc films onto hBN/SiO_2 by sublimation in vacuum will be discussed. hBN is chosen as a substrate since it is compatible with the formation of 2D supramolecular layers and the acquisition of images with molecular resolution using atomic force microscopy (AFM) under ambient conditions. Since hBN is an insulator the fluorescence of the adsorbed molecular layers may also be measured, facilitating investigations of the correlation between morphology and optical properties [16, 19].

4.1 Growth of phthalocyanine thin films

4.1.1 Growth of H_2Pc monolayer

H_2Pc powder was purchased from Sigma-Aldrich and sublimed under vacuum conditions onto hBN flakes, which had been exfoliated and transferred to a supporting Si/SiO_2 substrate then cleaned following the procedures summarised in Section 3.5 [18]. Thin films were prepared by sublimation of H_2Pc under vacuum conditions at a typical base pressure of 1 x 10^{-7} mbar. The powder was heated to 300°C , resulting in

a deposition rate of approximately 0.5 monolayers/min, which was held constant during the deposition process. A quartz crystal microbalance (QCM) was used to monitor the deposition rate and thickness. The substrate temperature was controlled using an ohmic heating element and measured using a type K thermocouple.

Figure 4.2 (a) shows the thin film morphology of a 0.7 ML coverage of H_2Pc, deposited on hBN while the substrate was held at room temperature. Rectangular islands are observed with typical lengths ranging from 0.3 μm to 2 μm, and widths ranging from 0.2 μm to 0.4 μm.

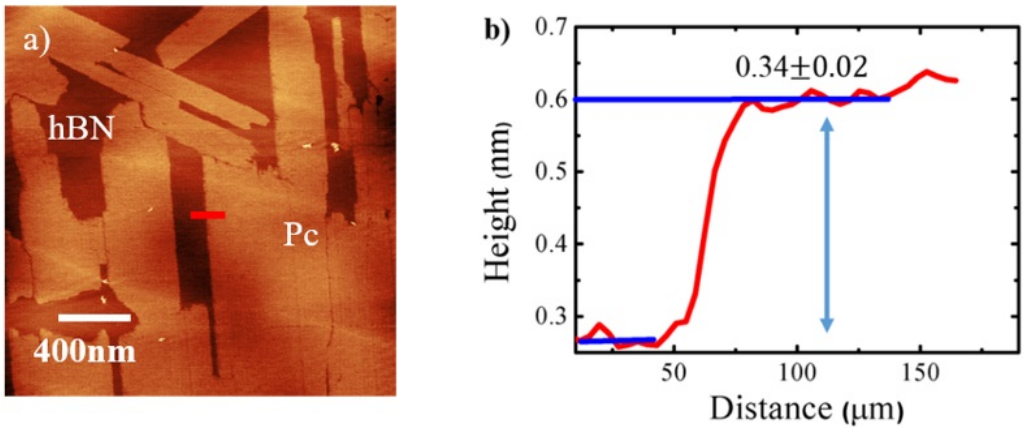


Figure 4.2: a) AC mode AFM image of 0.7 ML of H_2Pc on hBN; b) the height profile of an island along the red line marked in panel (a) which indicates that the molecules are co-planar with the surface.

The height of the islands estimated from the profile in Figure 4.2 (b) is 0.34 ± 0.02 nm, and is consistent with the formation of a monolayer of H_2Pc with the molecular plane lying parallel to the surface. Also, it can be observed that the elongated island facets of the H_2Pc monolayers are oriented along specific directions. Island orientations were extracted by manually defining the direction and length of islands using the measuring distances and directions between points tool in Gwyddion and plotted as a histogram,

as seen in Figure 4.3 [109]. The three peaks in the histogram separated by 60° suggest that the major axes of the H_2Pc islands are aligned with a high symmetry axis of hBN.

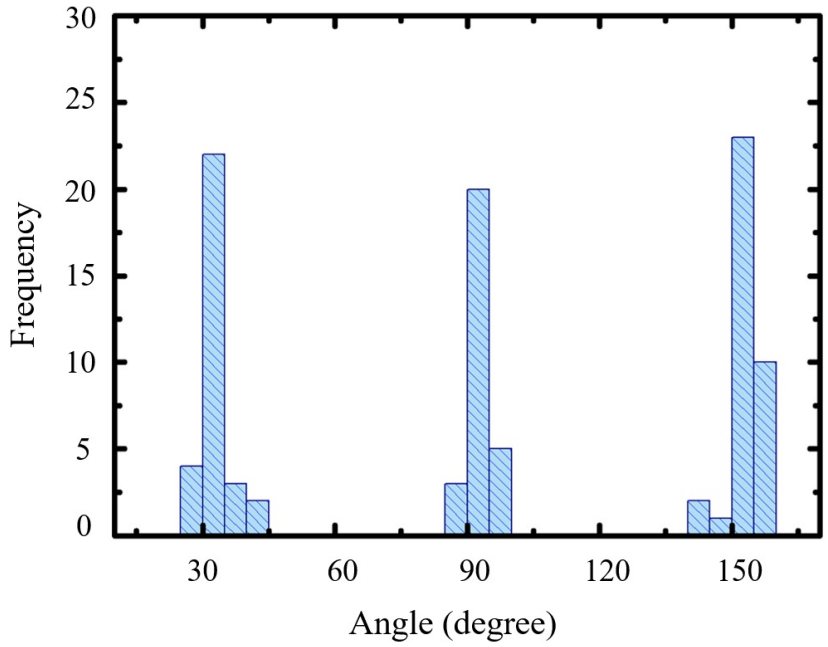


Figure 4.3: A histogram of the facet islands orientation of H_2Pc grown on hBN on SiO_2 at room temperature is shown. The distribution taken values extracted from AFM images using Gwyddion.

When the substrate temperature was increased (discussed later in detail) to 300°C, or higher, the growth self-terminated after the formation of a monolayer. The resulting islands have lateral dimensions of a few microns. Figure 4.4 shows an AFM image of a sub-monolayer coverage of H_2Pc grown on hBN/SiO_2 at 300°C. Rectangular islands are observed with typical lengths ranging from 0.3 μm to 2 μm, and widths ranging from 0.1 μm to 0.4 μm similar to the thin film grown at room temperature shown in Figure 4.2 (a). The profile in Figure 4.4 (b) shows the island height which is 0.34 $\pm$ 0.03 nm. Similar to room temperature islands in Figure 4.2 (a), these islands have elongated island facets which are oriented along specific directions with the underlying substrate.

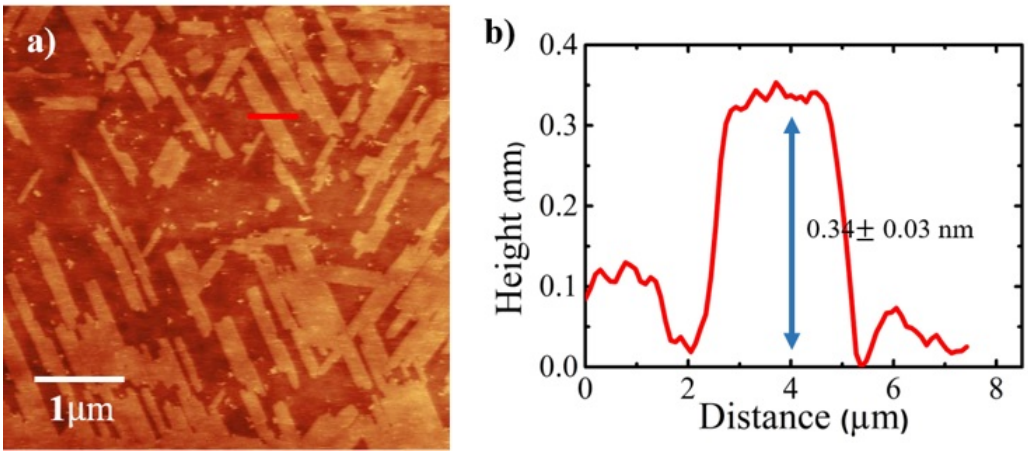


Figure 4.4: a) AC mode AFM image of a partial H_2Pc monolayer on hBN grown at 300°C; b) height profile of an island across red line in (a), which indicates that the molecules are co-planer with the surface.

Molecular scale resolution AFM images of 0.7 ML H_2Pc on hBN grown at room temperature are shown in Figure 4.5. The unit cell vectors of H_2Pc are marked by red arrows and were found to be a_{Pc}= b_{Pc}= 2.2 $\pm$ 0.03 nm, subtended by an angle θ= 86°.

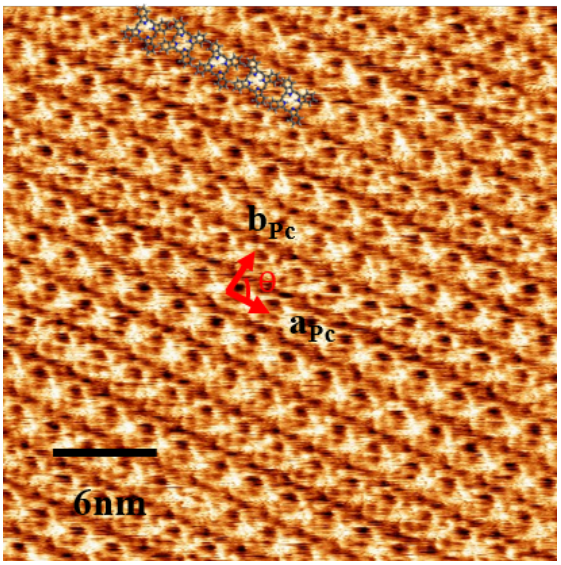


Figure 4.5: High resolution AFM image of H_2Pc grown on hBN/SiO_2 at room temperature; the unit cell vectors of the free-base phthalocyanine are a_{Pc} and b_{Pc} and they are subtended by an angle θ. Image acquired with the assistance of Dr.V. Korolkov.

Figure 4.6 (a, b and c) shows high resolution AFM image of the molecular scale resolution for partial monolayer grown of H_2Pc on hBN at 300°C. Similar ordering to the films grown at room temperature is observed. Once the molecular lattice of H_2Pc was observed the same area was imaged after switching to contact mode. In this procedure, the AFM tip is brought closer to the surface and the set point changed until the hBN lattice is resolved. The molecular layer removed from this area of the sample allows for a determination of the orientation of the layer relative to the hBN.

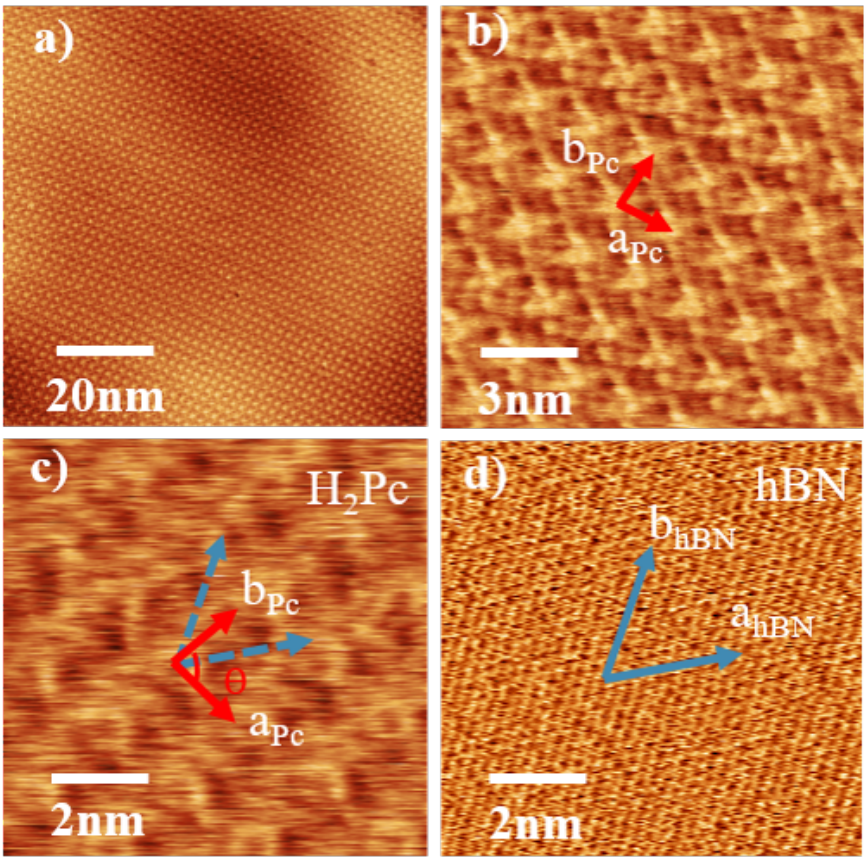


Figure 4.6: (a,b) High resolution AFM images showing the arrangement of H_2Pc on hBN at 300°C. (c,d) shown high resolution AFM images of the same area which allows a determination of the alignment of the molecular layer with the underlying substrate. Image taken with the assistance of Dr.V. Korolkov.

In these AFM images, the H_2Pc molecules appear as topographically bright features with a 'crosslike' shape similar to the features shown in Figure 4.5. The lattice vectors of H_2Pc, marked in Figure 4.6 (b) were extracted and found to be a_{Pc}= b_{Pc}= 2.18 $\pm$ 0.05 nm, subtended by an angle θ= 86°. The orientation of the lattice vectors (red arrows) of the H_2Pc monolayer and the hBN (blue arrows) were determined by comparing AFM images of the H_2Pc and the hBN lattices (see Figure 4.6 (c and d)). The lattice vectors of hBN were resolved in Figure 4.6 (d) (parallel to the blue arrows) and are overlaid on the H_2Pc molecules in Figure 4.6 (c). From these images it is determined that the lattice vector b_{Pc} is aligned at angle of 30° to both hBN lattice vectors, one of the high symmetry directions of the hBN substrate, consistent with the histogram shown in Figure 4.3.

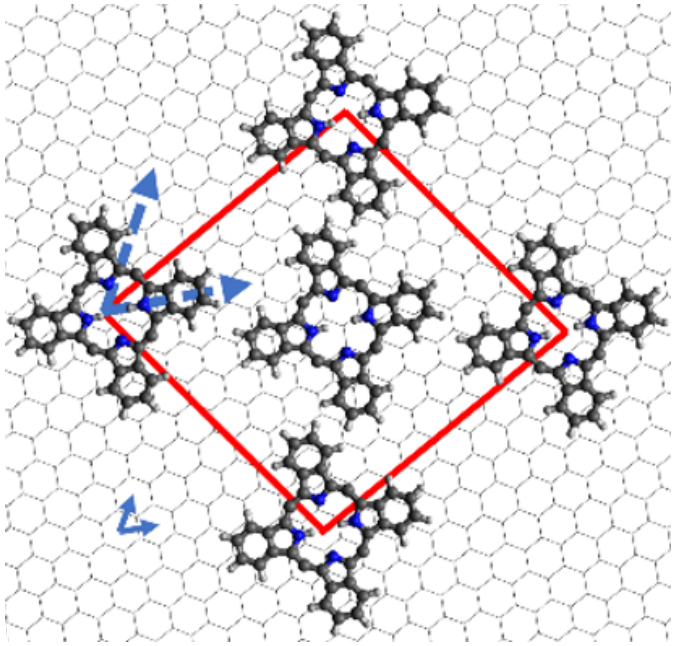


Figure 4.7: Proposed schematic structure of H_2Pc on hBN; the unit cell vectors of the free-base phthalocyanine are a_{Pc} and b_{Pc} and they are subtended by an angle θ; the blue arrows denote the directions of the hBN lattice vectors, which the lattice vectors a_{Pc}= b_{Pc}= 2.2 $\pm$ 0.03 nm and the angle θ= 86°.

Figure 4.7 shows the proposed schematic structure of deposited H_2Pc at 300 °C extracted from a high resolution AFM image as shown in Figure 4.6. The schematic structure of the H_2Pc layer overlaid on hBN as shown in Figure 4.7 and the blue arrows denote the directions of the hBN lattice vectors.

The axes of the H_2Pc molecules (parallel and perpendicular to the C–H bonds within the central ring of the macrocycle) are misaligned from the hBN lattice vector by approximately $4 \pm 2°$. The molecules appear alternately bright (at the corners of the unit cell in Figure 4.6 (b)) and dark (at the centre of the unit cell). The different AFM contrast of molecules is most likely due to a variation in adsorption site; in previous studies of molecular overlayers on hBN, the Nottingham group has reported the appearance of moiré patterns [18] in AFM images arising from a mismatch in lattice constants, and thus variations of local adsorption site. The H_2Pc unit cell is similar to that previously reported on other substrates [110–113].

The adsorption energy and geometry of H_2Pc were calculated by Dr. Anton Nizovtsev using density functional theory (DFT) through a collaboration with the Chemistry department in the University of Nottingham. The atomic positions of a model hBN monolayer flake consisting of 65 boron atoms and 65 nitrogen atoms were initially optimized and frozen in subsequent calculations. The optimized structure for a single H_2Pc molecule on hBN is shown in Figure 4.8 and confirms a planar adsorption geometry with a molecule-surface separation, d= 0.33 nm and adsorption energy, E_A= 3.35 eV. In common with our images the calculations show the molecular axis misaligned with the hBN lattice vector, but by a larger angle, 13°. We attribute this difference to a combination of a low barrier for rotation and the role of intermolecular interactions [114].

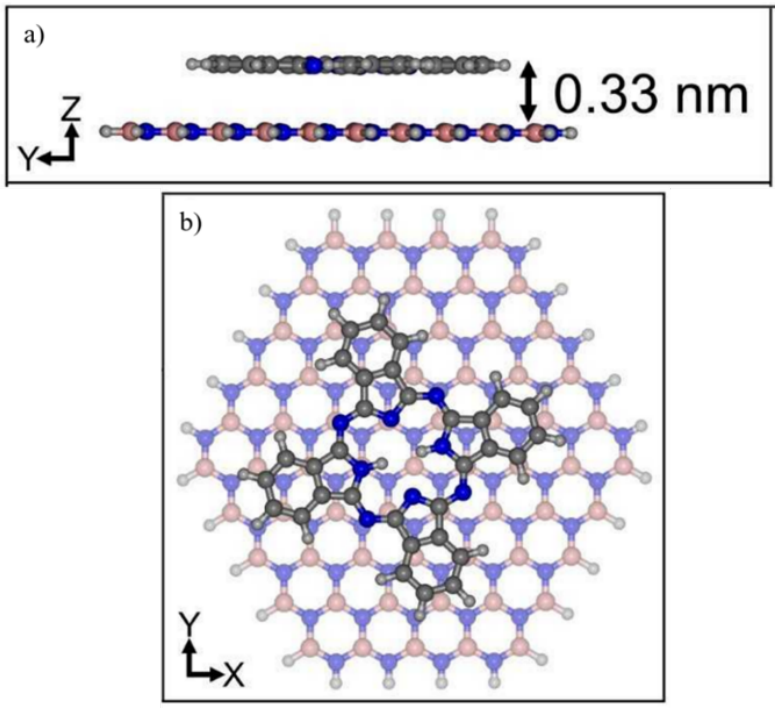


Figure 4.8: Calculated adsorption geometries for H_2Pc on hBN; (a) Cross-sectional view illustrating planarity of adsorption geometry and molecule-substrate separation. (b) Top view of H_2Pc on hBN.

4.1.2 The morphology of H_2Pc thin films on hBN: coverage dependence

A series of samples of H_2Pc films were grown on hBN at room temperature with thickness ranging from 1 nm to 32 nm equivalent thickness (the equivalent thickness is the thickness averaged over the surface assuming a film of uniform height is formed; the actual thickness may differ for an inhomogeneous surface at high temperatures when the sticking coefficient is less than 1; 1 nm is equivalent to 3 ML surface coverage). Figure 4.9 shows AFM and optical microscopy images of the same hBN flake, after the deposition of material with an equivalent thickness of 1 nm at room temperature. In these and thicker films, inhomogeneous growth with several large islands (identified by arrows) of around 25 nm height is observed following the deposition of H_2Pc and these islands can be resolved using optical microscopy as shown in Figure 4.9 (b) for the

same hBN flake imaged using AFM and shown in Figure 4.9 (a). Interestingly, the islands indicated with red and blue arrows in Figure 4.9 have a direction which is locally correlated and oriented in one of three directions subtended by 60°.

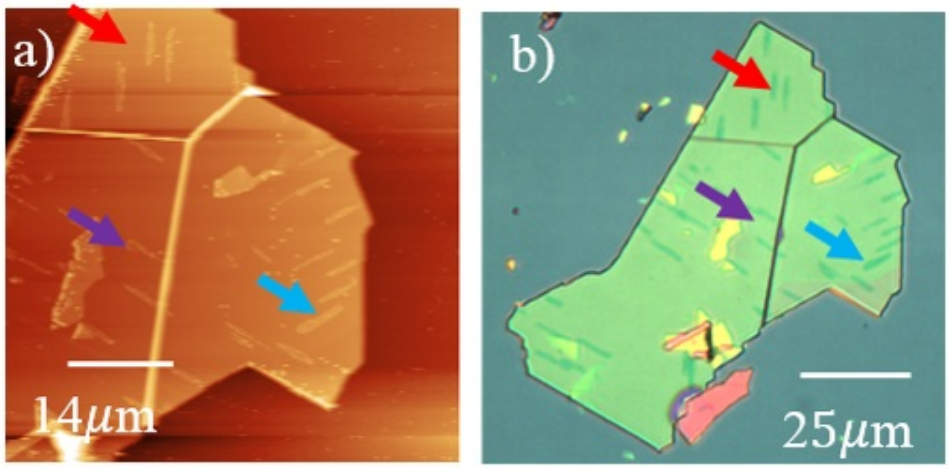


Figure 4.9: (a) AC mode AFM image of an equivalent thickness of 1 nm thin film of H_2Pc on hBN; (b) the optical microscopy image for the same flake. Both images illustrate one-dimensional island formation and the arrows with same colours show the same islands in both optical and AFM images.

Equivalent thickness of 1 nm H_2Pc on hBN is found to cover around 10% of the surface. In Figure 4.10 (a), a high resolution AFM image shows islands are aggregated in a quasi-ordered array of one-dimensional crystallites. The height profile in Figure 4.10 (b) shows the typical height of these formations is 24 $\pm$ 3 nm (average over 17 islands) and the island length is 5-10 μm.

At higher coverages, monolayers of phthalocyanine are present between aggregated 3D islands, and form a uniform and compact monolayer without step edges. Due to the height of top islands, these monolayer could not be observed using AFM images.

Figure 4.11 shows islands observed both with AFM and optically for an equivalent thickness of 2 nm. The percentage coverage of this sample was greater, around 20

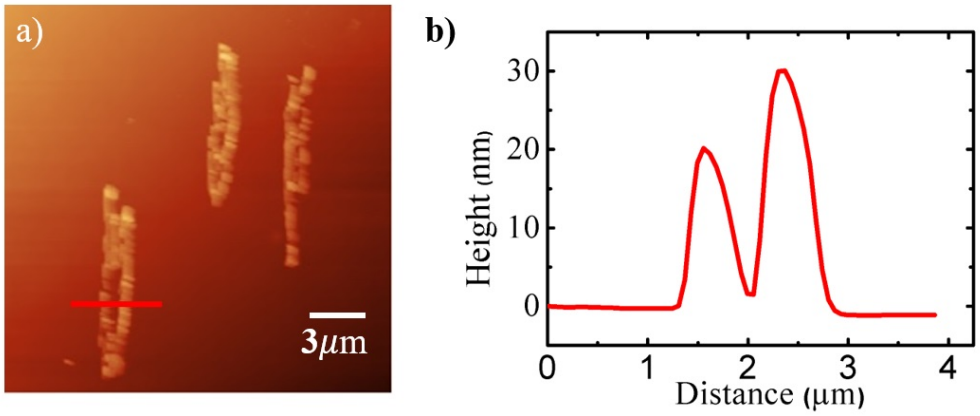


Figure 4.10: (a) AFM image of an equivalent thickness of 1 nm thin film of H_2Pc on hBN; (b) the height profile of an island shown by a red line in image (a), indicates that the molecules are aggregated in one-dimensional islands.

% of the surface. The islands are oriented parallel locally similar to the sample with an equivalent thickness of 1 nm. As shown in Figure 4.11 (a-d), the typical length of the islands, 10-20 μm, is approximately twice as large compared with the sample of 1 nm coverage. However, the typical island height is 24 $\pm$ 6 nm (average over 27 islands), which is similar with the previous sample. The islands are aggregated in a quasi-ordered array of one-dimensional crystallites as shown in Figure 4.12 (a,b).

A possible reason for the common alignment of the H_2Pc crystallites is that they are nucleated, and grow along step edges. It is thought that the steps on exfoliated hBN run along the armchair direction and can be separated by a few microns. The steps also run at well defined angles to the flake edges. This may explain the formation of linear islands following directions that are at 60° to each other (the angle associated with the armchair hexagonal lattice structure of hBN marked in blue dashed line as shown in the inset of Figure 4.11 (d)). Furthermore, these angles are often observed to be perpendicular to the facet edges of hBN flake, which should themselves be aligned to the hBN lattice. At different areas of the hBN the linear islands switch their most

common direction of growth, although still aligning with one of the lattice directions. This is seen for example past the ∼3 nm step edge seen in the upper left hand side of the inset of Figure 4.11 (a), and additionally for the regions either side of the highlighted BN fold in Figure 4.11 (c).

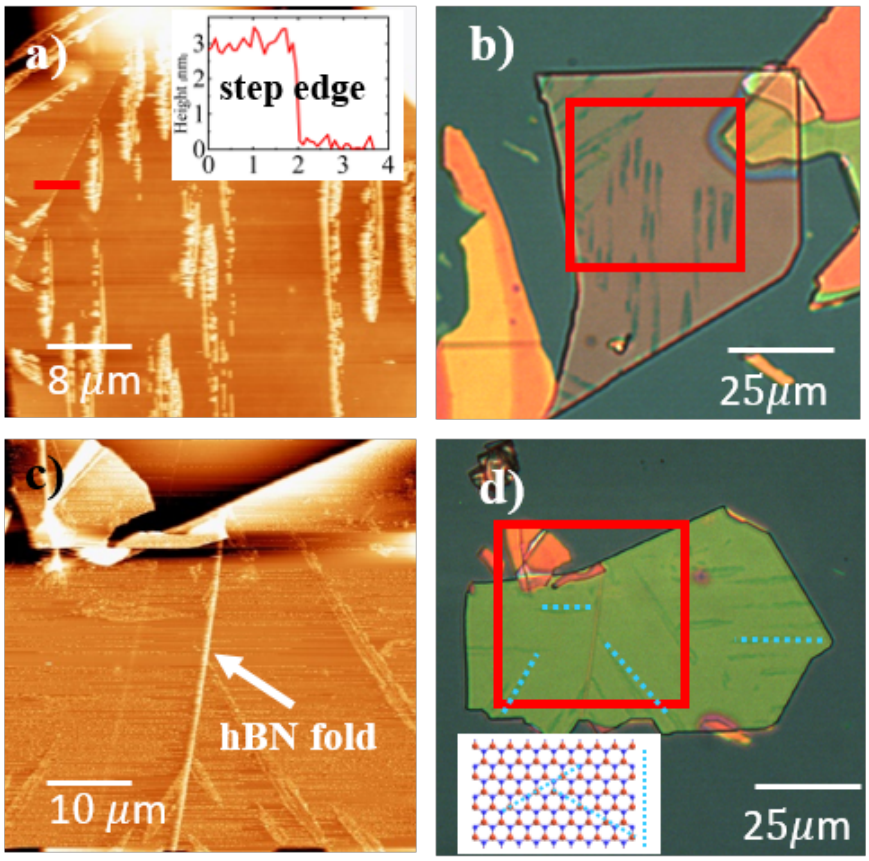


Figure 4.11: (a,c) Morphology determined using AFM of an equivalent thickness of 2 nm thin film of H_2Pc on hBN from different flakes; (b,d) the optical microscopy images for the same flakes in (a,c) respectively. All images illustrate one-dimensional island formation. The inset in (a,d) show the height profile of step edge of hBN marked in (a) with red line and the three armchair lattice directions of hBN marked with dashed blue line respectively.

The exploration of this aspect of growth was problematic since high resolution imaging with AFM was not successful because of high levels of noise related to the island height (∼25 nm).

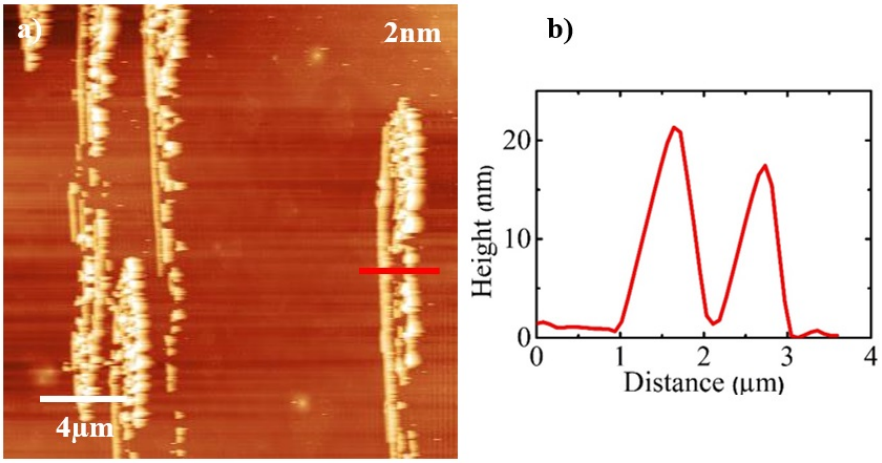


Figure 4.12: (a) AFM image of an equivalent thickness of 2 nm thin film of H_2Pc on hBN; (b) the height profile of an island shown by a red line in image (a), indicates that the molecules are aggregated in one-dimensional islands.

A possible growth mode of H_2Pc is illustrated in Figure 4.13, which is similar to that observed by Plamgren et al. for H_2Pc [115, 116] and iron phthalocyanine [117]. The adsorption of these molecules have also been studied on TiO_2 (110) surfaces. On TiO_2, it has been reported that the first layer of H_2Pc adsorbs flat-laying on the surface and does not form any ordered structures. Within the first layer, the molecules bind strongly to the surface by chemisorption. However, the molecules in the second layer exhibit bulk-like properties. Wang [118] reported an investigation of ZnPc molecules on graphene, they found these molecules also tend to adsorb lying flat to the surface, as is the case with ZnPc on HOPG [110].

Figure 4.14 shows a strong dependence of the mode of growth on the thickness of the film coverage. From the AFM images, as the coverage is increased from 4 to 16



Figure 4.13: Schematic diagram illustrating growth modes, molecular ordering and molecular backing of H_2Pc molecules on hBN/SiO_2 surface deposited at: (a) sub-monolayer thin film;(b) thickness in the range of 1 nm-32 nm.

nm equivalent thickness, the mode of growth changed and disordered islands were formed. The percentage coverage of 4 nm and 8 nm equivalent thicknesses was around 20 $\pm$ 4 %. The coverage of the disordered islands increased to 30 $\pm$ 2% as the total amount of material deposited was increased to 16 nm equivalent thickness. The height profiles of these images show an average height between 20-30 nm for aggregated islands. These aggregated islands are sometimes terminated by a hBN fold, small defect or step edges as shown 4.14 (a).

Figure 4.15, shows images of two hBN flakes acquired with optical microscopy. In this sample the deposited film was increased to an equivalent thickness of 32 nm H_2Pc. It reveals needle-like islands, which merge to cover a greater proportion of the surface and are slightly oriented. The percentage of island coverage of this sample was increased to be around 43 $\pm$ 5 % on surface.

The average island height for equivalent thickness of 32 nm was 26 $\pm$ 4 nm (average over 15 islands) as shown in Figure 4.16 which is similar with previous equivalent thicknesses. Notice that the AFM image shows the growth of H_2Pc islands were terminated at folds and faults of the hBN surface as shown in Figure 4.15 (e).

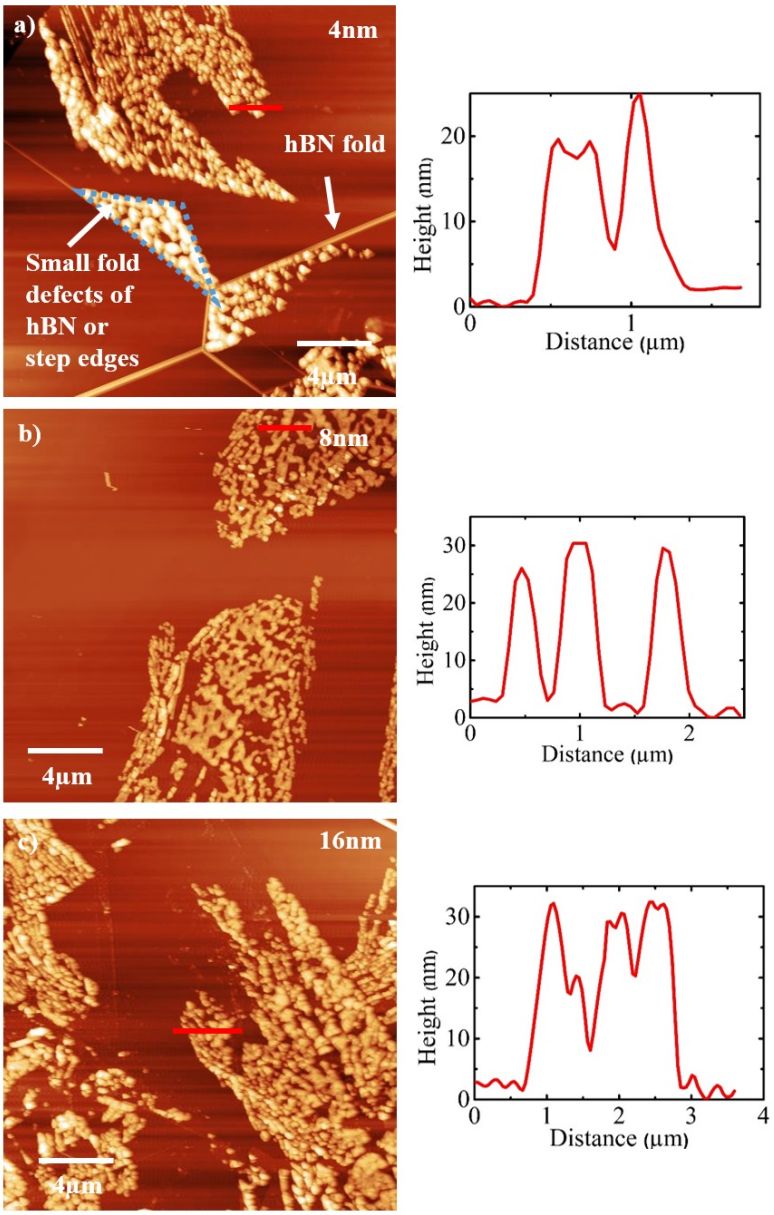


Figure 4.14: Topographic AFM images (right colum) and the height profiles of these images (left colum) showing the crystalline structure of H_2Pc on hBN at equivalent thicknesses: a) 4 nm; b) 8 nm; c) 16 nm.

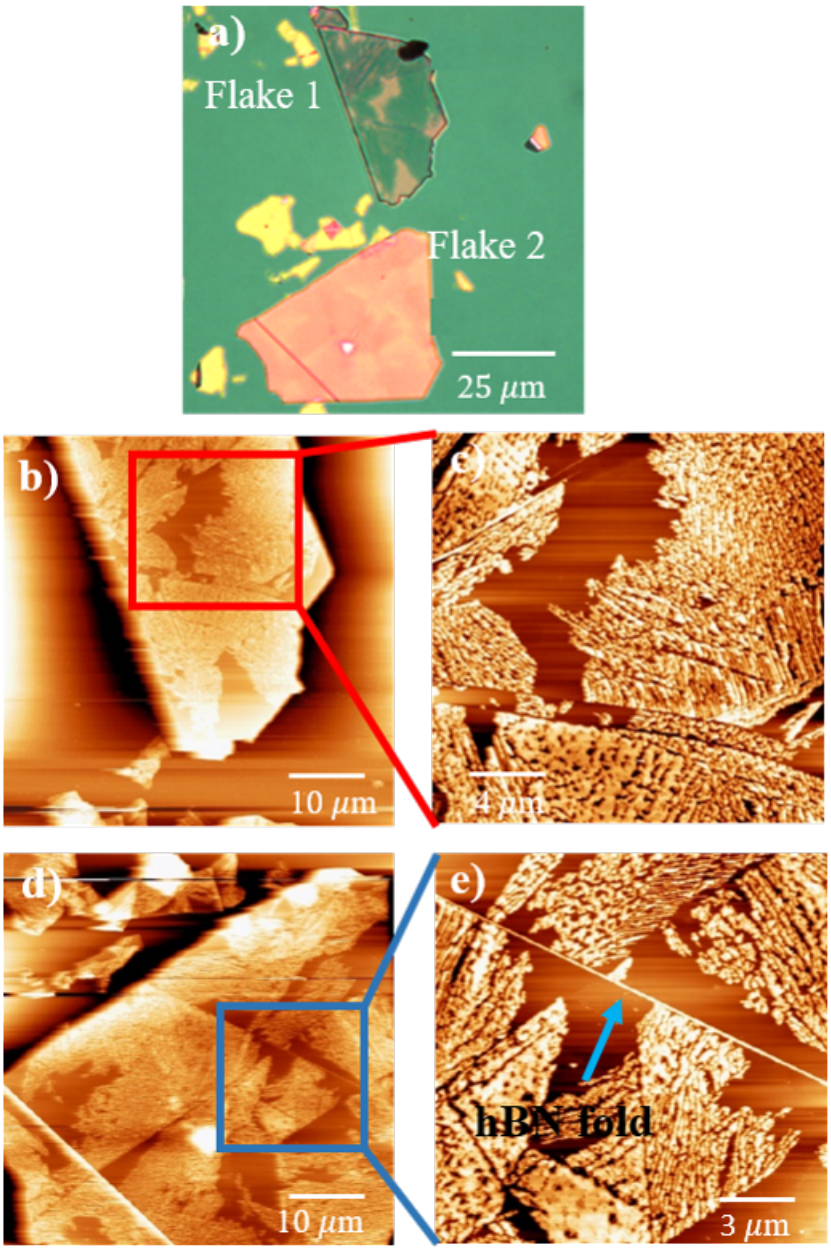


Figure 4.15: (a) the optical microscopy images for flake1 and flake2. (b,c) and (d,e) AFM morphologies of an equivalent thickness of 32 nm thin film of H_2Pc on hBN form flake 1 and flake 2 respectively. All images illustrate one-dimensional island formation.

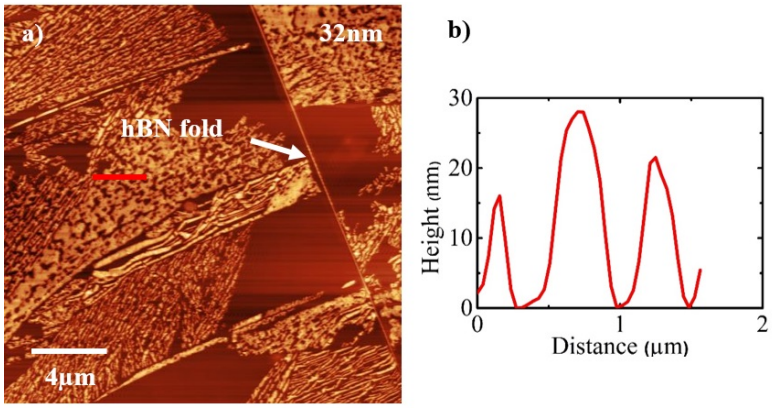


Figure 4.16: (a) AFM image of equivalent thickness of 32 nm thin film of H_2Pc on hBN; (b the height profile of an island shown by a red line in image (a).

Overall the results show an abrupt transition to the growth of three-dimensional crystallites following the completion of a highly ordered monolayer. As discussed previously molecules switch from the flat-lying adsorbed state in the monolayer to a geometry in which the molecular plane is at an angle to the hBN substrate in higher layers, thus forming one-dimensional crystallites in which molecules are co-planar, maximising π–π interactions. Such a switch from a flat-lying to upright morphology has been observed previously in studies of adsorbed H_2Pc [45]. Interestingly, it was not possible to observe the flat lying monolayer in between the aggregated islands using AFM. However, the corresponding PL peak for the monolayer was still measured for all sample thicknesses suggesting that flat-lying molecules are still present on the surface (as seen later in this chapter).

4.1.3 The morphology of H_2Pc thin films on hBN: temperature dependence

In this section, thick films (32 nm) of H_2Pc deposited at range of substrate temperatures, from room temperature to 520°C, are discussed. Films were deposited under vacuum conditions using the same deposition rate as for earlier samples. Figure 4.17 shows op-

tical images of samples grown with increasing substrate temperatures to 90°C, 160°C, and 300°C. In Figure 4.17, the islands are indicated by red arrows. These islands are clearly visible in optical microscopy images for 90°C, and 160°C samples. When the temperature is increased from room temperature (see Figure 4.16 (a)) to 90°C, and 160°C (as shown in Figure 4.17 (a,b)) the contrast of islands increases. At 300°C, these aggregate islands are not present and H_2Pc forms a uniform monolayer on the surface as shown in Figure 4.17 (c). As the substrate temperature increases to 520°C, the optical images for all substrate temperatures show a clean flake surface and the aggregated islands are no longer observed.

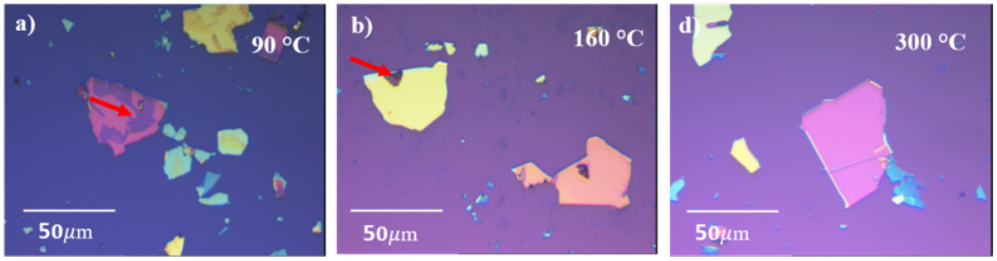


Figure 4.17: The optical images of H_2Pc on hBN into SiO_2 as the substrate temperatures was increased as shown in: (a) 90°C; (b) 160°C; (c) 300°C. The red arrows in a, and b indicate the islands which visible on the optical images while in d, the islands are not present as the temperature is increased.

In Figure 4.18, the percentage of island coverage of 300°C sample is 45 $\pm$ 5 %. As the substrate temperature was increased, the islands growth were increased to be around 61 $\pm$ 7 % and 82 $\pm$ 5 % for the 400°C and 520°C samples respectively.

In these AFM images the islands size increased with increasing substrate temperature, while still following the hBN lattice orientations (60° angles). High resolution images of Figure 4.18 (a) were obtained, shown earlier in Figure 4.6. High resolution images of (b or c) could not be obtained. This may indicate a change in the nature, or break

down of the molecule. This is consistent with PL measurements discussed later in this chapter.

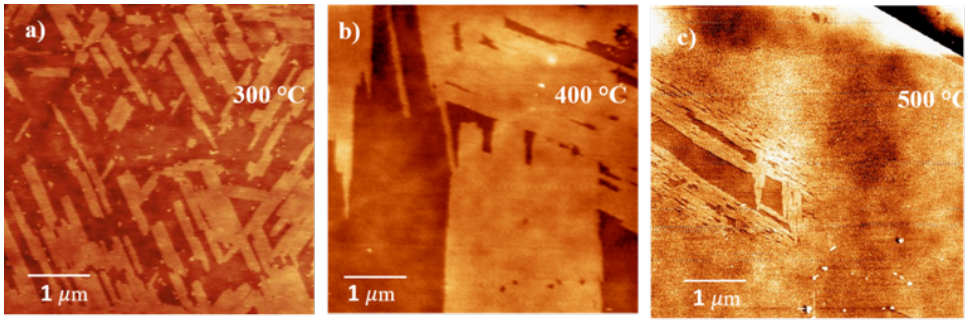


Figure 4.18: The morphology of AFM images of H_2Pc on hBN on SiO_2as the substrate temperatures was increased as shown in: (a)300°C; (b) 400°C; (c) 520°C.

4.2 The Fluorescence of H_2Pc thin films on hBN

The growth of monolayers, thin films, and different film thickness allows us to explore the optical properties of H_2Pc on hBN using fluorescence microscopy (as described in Section 3.4). Electrons in the HOMO upon adsorption of photons of sufficient energy are excited to the LUMO state. Fluorescence occurs when the molecule relaxes back to the ground state by the emission of a photon.

Since hBN is an insulator, the fluorescence of the adsorbed molecular layers is not quenched, unlike for metallic and semiconducting surfaces. This facilitates an investigation of the correlation between morphology and optical properties of the organic film.

In this section we describe the fluorescence of the deposited films described earlier in this chapter. The fluorescence of H_2Pc on hBN was measured using a Horiba LabRAM Raman spectrometer with 660 nm wavelength excitation laser. The spot size (using a $\times 50$ objective) of the red laser was 2 μm^2, and the beam intensity was 8.6 mW μm^{-2}.

Figure 4.19 shows the fluorescence spectra of a H_2Pc submonolayer measured from three different hBN flakes. In each of the measured spectra, there are three peaks centred at 1.75 eV, 1.67 eV, and 1.58 eV. The most intense peak is the (0-0) zero transition at 1.75 eV. The 0-0 peak is red shifted relative to gas phase measurements of H_2Pc fluorescence for which the zero phonon line is centred at 1.879 eV, illustrated in the same Figure by the dashed blue line [119]. The origin of this red shift is due to interactions with both the surface and neighbouring molecules, and is explored in detail below.

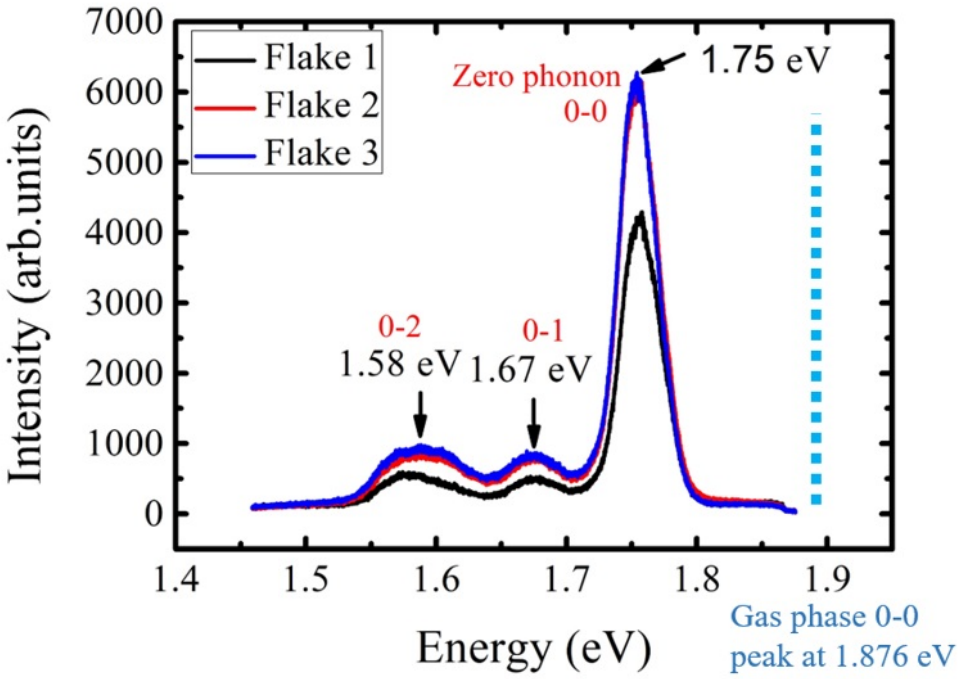


Figure 4.19: The fluorescence spectra of a 0.7ML H_2Pc film. These particular spectra were taken from three different hBN flakes as shown in different lines colours. The gas phase zero phonon line of H_2Pc indicated with blue dashed line.

The additional two peaks at values 1.67 eV, and 1.58 eV arise due to transitions back to excited vibrational states of the electronic ground state of the molecule. In a number of systems, the vibronic side-bonds are less intense because of a reduced overlap between vibrational wavefunctions of the two states that are involved in the transition.

In order to acquire the spectra from the source material of H_2Pc, a small amount of powder was deposited on a glass slide. The spectrum showed a broad peak at 1.42 eV (blue line), as shown in Figure 4.20. The fluorescence spectrum of H_2Pc islands with 1 nm equivalent thickness are also shown in Figure 4.20. Three peaks are resolved in the spectra taken from an area off the island, (black line) at 1.76 eV, 1.67 eV, and 1.57 eV. The main peak at 1.76 eV corresponds to the zero phonon emission line. However, there is an additional peak shown in the spectra taken from an area on the island (red line) at 1.38 eV which is close to the broad peak at 1.42 eV observed in the fluorescence spectra of bulk H_2Pc as shown in Figure 4.20.

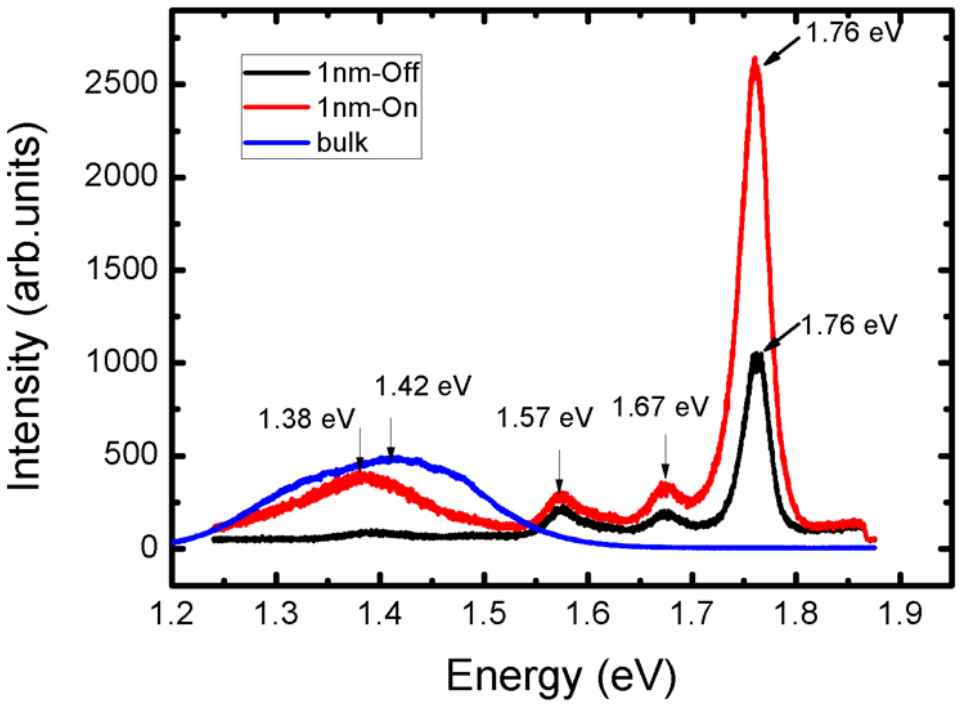


Figure 4.20: The photoluminescence spectra of a 1 nm H_2Pc film. These spectra were taken from the same hBN flake at different positions, on the islands (red line), and off the islands (black line) while the blue line shows the spectrum of bulk H_2Pc.

As the deposition thickness was increased to 2 nm equivalent thickness, the one-dimensional islands become larger and longer as shown previously in AFM images, see Figure 4.11.

The fluorescence peak in Figure 4.21 (a), on the islands (red line) occurs at 1.75 eV which is the zero-phonon peak similar to the peak observed for a monolayer in Figure 4.19. The peak at 1.38 eV corresponding to the bulk H_2Pc taken from an area off islands is less intense than the peak on the islands where all the parameters of the experimental conditions are kept the same. As the thicknesses was increased to 4, 8, and 16 nm equivalent thicknesses the fluorescence spectra taken from areas on the islands (red lines) show that the intensity of the zero-phonon peak (0-0) decreased while the intensity of bulk peaks increased as shown in Figure 4.21 (b,c,d). The fluorescence spectra taken from areas off the islands (black lines), show decreased (0-0) peaks strength with no apparent increase in the intensity of the bulk peaks. Notice that the peak is still present off the islands despite the fact that no molecules were observed using AFM for high temperature. It is possible that the fluorescence arises from molecules which are diffusing rapidly on the surface as reported for α- sexithiophene on silicon dioxide [120].

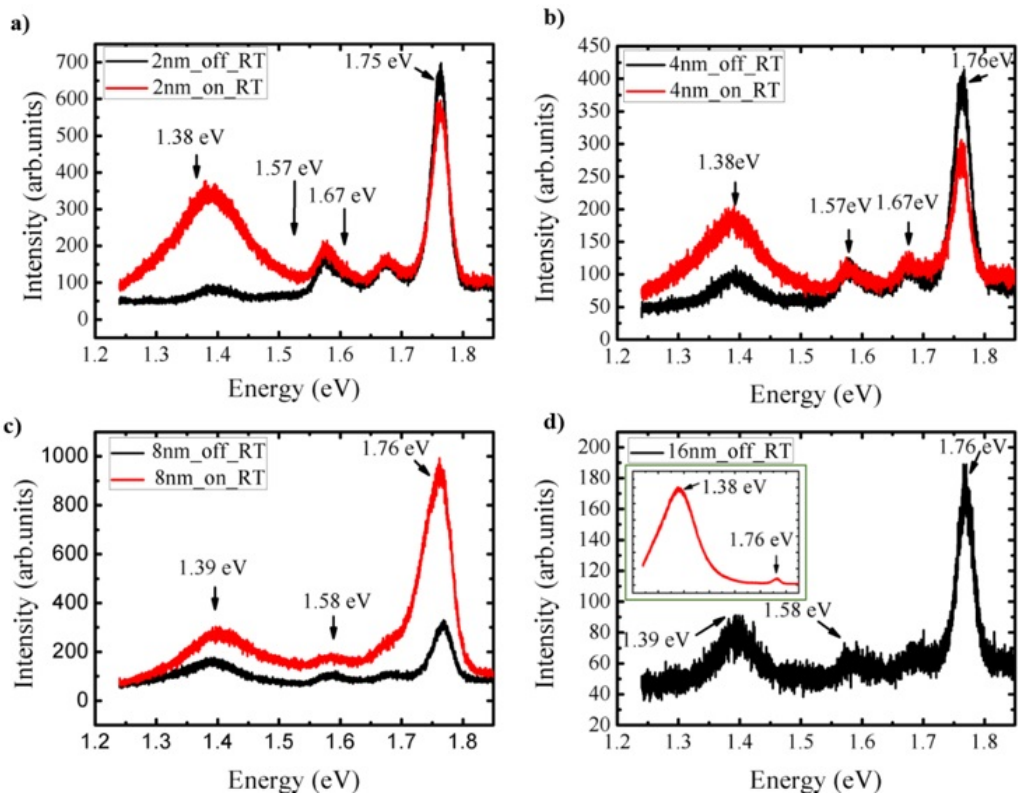


Figure 4.21: Fluorescence spectra were taken from the same hBN flake at different positions on the islands (red line) and off the islands (black line) of H_2Pc thin films on hBN at room temperatures as the coverage was increased: a) 2 nm; b) 4 nm; c) 8 nm; d) 16 nm.

The intensity vs thickness variation plotted in Figure 4.22 which shows the observed decrease in 0-0 peak intensity with increasing material coverage for regions away from islands.

The normalized fluorescence spectra for a range of different thickness taken from the area off the islands is shown in Figure 4.23 and it is reveals the bulk peak appears with increasing thickness (see dark blue line in same figure).

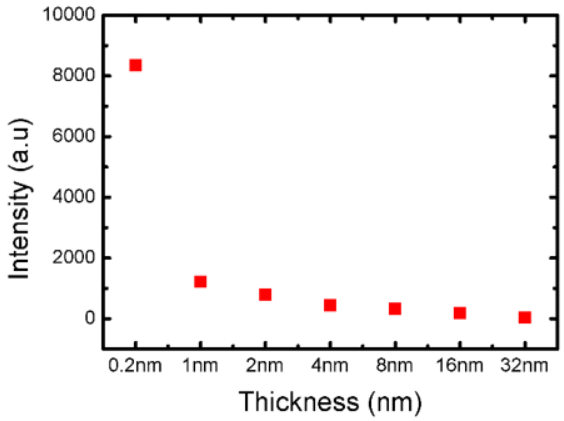


Figure 4.22: Fluorescence spectra were measured for thin films away from bulk islands, with a range of coverages of H_2Pc on hBN grown at room temperature. The data were fitted to a set of lorentzian curves and the intensity for the 0-0 peak was extracted.

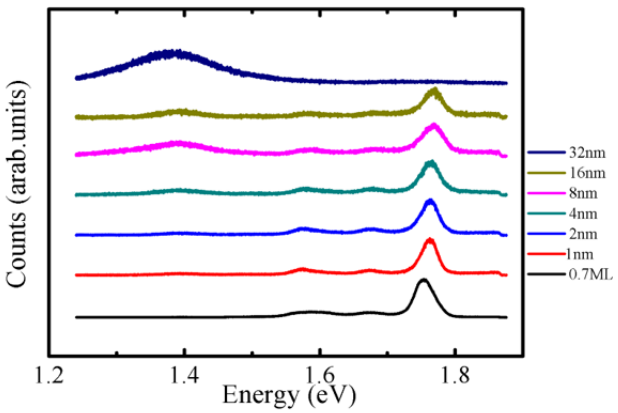


Figure 4.23: Normalised fluorescence spectra of H_2Pc on hBN /SiO_2 for a range of different thickness ranging from sub-monolayer to 32 nm grown at room temperature and acquired using a 660 nm excitation laser. The normalised spectra are shown for the area off the islands.

Figure 4.24 shows the integral ratio of the monolayer peak at 1.73 eV and bulk peak at 1.38 eV against the thickness on-islands (left) and off-islands (right).

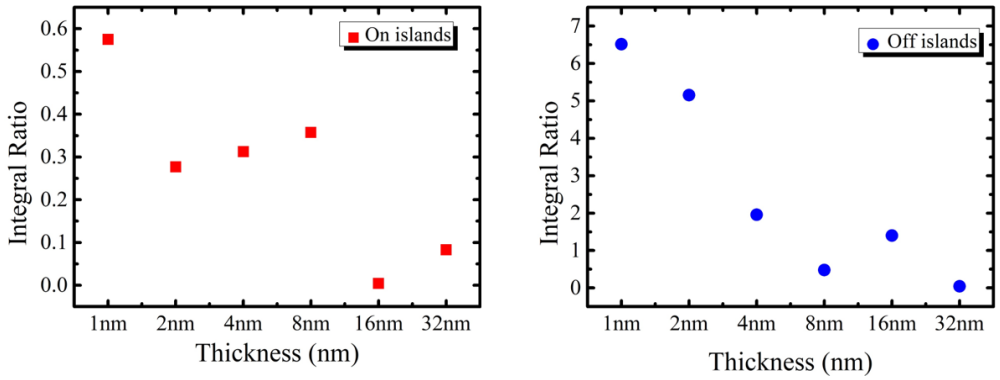


Figure 4.24: The ratio of fluorescence spectra of the monolayer and bulk peak intensities at 1.73 eV and 1.38 eV respectively of different thickness of H_2Pc on-islands and off-islands on hBN grown at room temperature extracted from a fit of lorentzian curves. The fitted curves corresponded to the main fluorescence peak for the thin film and the bulk phase. The intensity and the integrated counts of the fitted curves were then compared to generate the peak ratio which is plotted against the amount of coverage material on the samples.

4.3 The fluorescence of H_2Pc thick films on hBN at different substrate temperatures

This section is linked to previous section of AFM morphology and optical images (section 4.1.3) of sublimed H_2Pc thick films on hBN at different substrate temperatures. Figure 4.25 shows the fluorescence spectra taken from the area on the islands (red line) and the area off the islands (black line) for equivalent thickness of 32 nm film grown at room temperature and different substrate temperatures. The spectra of the thick film for the sample at room temperature, the peak taken from the area of visible islands (red line) is at 1.37 eV, which is similar to the bulk value, while the peak taken from the area off the islands (black line) at two values 1.37 eV as observed on the bulk and 1.73 eV, which is similar to the thin film in the monolayer.

Increasing the substrate temperature to 90°C, the islands are still visible on the optical microscopy image indicated by the red arrow in Figure 4.17. The spectra on the islands have two peaks at values of 1.75 eV and 1.38 eV, which are similar to the energies of the peaks from the monolayer and bulk phase. However, the spectra off the islands are sharp and narrow, at peak at an energy of 1.74 eV. There are two vibronic peaks similar to those in the thin film but no peak associated with the bulk phase. In contrast, the optical image for 160°C shows that the molecules aggregate in dark and intense black areas, see Figure 4.17. The PL spectra on this area shows a peak at 1.39 eV which is similar to the bulk value but the measurements off this area (black line) shows the thin film value but spectra acquired off the islands show negligible emission at 1.39 eV.

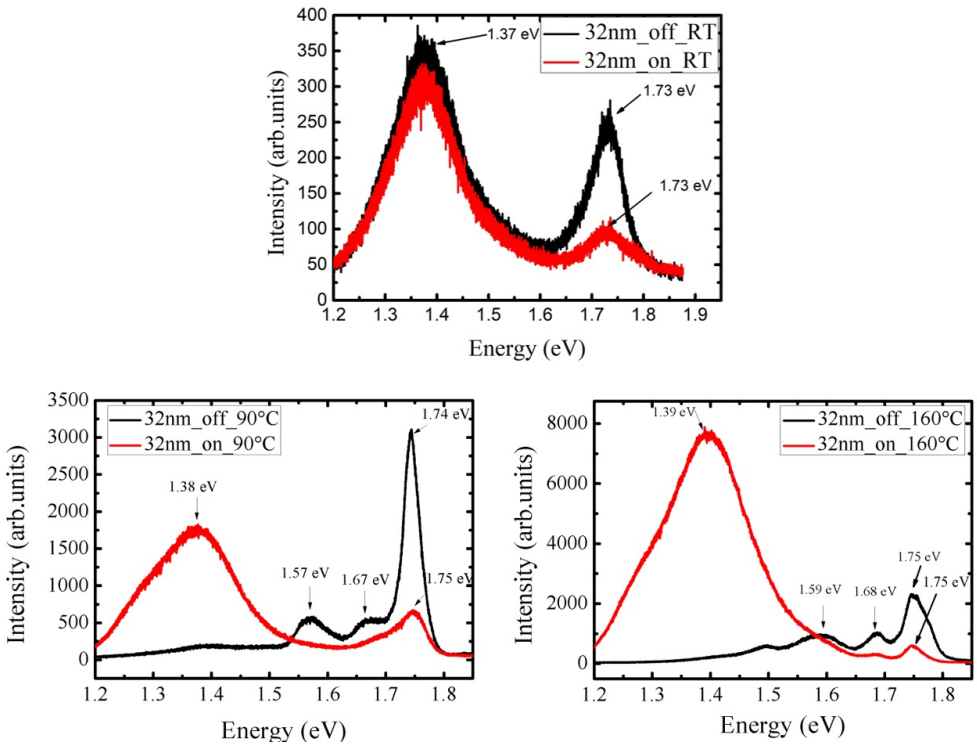


Figure 4.25: The photoluminescence spectra of 32 nm of thick film at different substrate temperatures; RT, 90°C , and 160°C. Theses spectra were taken on the island (red line) and off the island (black line) of H_2Pc on hBN.

When increasing the substrate temperature to 200°C and 300°C, the molecular film grows homogeneously and no aggregated molecules were observed using the AFM or optical microscopy. The spectra for these substrate temperature samples give a sharp peak at 1.75 eV without any bulk peak as shown in Figure 4.26. This confirms that the growth of the molecules on the surface tend to be as a monolayer as shown in AFM previously. For the substrate temperature of 400°C the peaks appear with very low intensity. Up to 520°C substrate temperature, there is no evidence for any active molecules.

The samples examined in Figure 4.26 have been imaged using AFM as shown previously in Figure 4.18. In these images the higher temperature sample appear to have a greater coverage. However, there is a significant drop in the intensity of H_2Pc peaks observed at higher temperature. At 400°C the peak is still present, with a greatly reduced intensity compared to higher temperatures, at 520°C whereas the peak has disappeared entirely. This may be explained as due to molecules partially decomposing or reacting with other molecules [120].

In all spectra, the 0–0 peak for H_2Pc is red-shifted by ΔE= 0.13 eV as compared with a molecule in the gas phase (0–0 peak at 1.876 eV) [121]. This red-shift can be due to the combination of effects arising from interactions at molecules with the substrate and with nearest neighbours as reported previously [16, 19] and [122–124]. A non-resonant contribution to the shift due to the substrate has been calculated using time-dependent density functional theory (TD-DFT) by Dr. Anton Nizovtsev (Nottingham University, Chemistry). The molecule is optimized in the excited (S1) state both on (adsorbed) and off (gas phase) the hBN surface where the transition to the ground state (S0) is calculated in each case. The calculated transition energies for a molecule on the

hBN surface, and in the gas phase are 1.76 eV and 1.87 eV respectively. These values are close to the measured peaks in fluorescence and their difference implies a non-resonant red-shift ΔE_{nr}= 0.11 eV due to adsorption on hBN. Non-resonant interactions arise when there are shifts in molecular energy levels because of surface adsorption, can be calculated using (DFT).

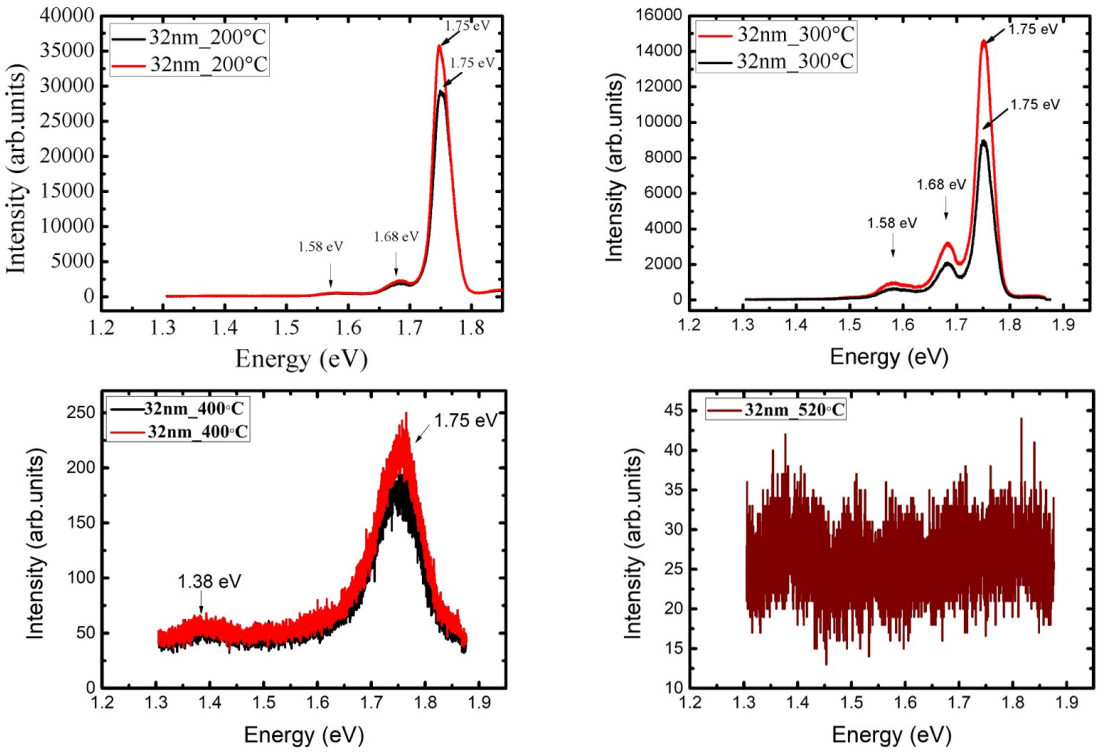


Figure 4.26: The photoluminescence spectra of 32 nm of thick film at different substrate temperatures; 200°C, 300°C, 400°C, and 520°C. Theses spectra were taken on the island (red line) and off the island (black line) of H_2Pc on hBN.

Overall our results demonstrate that the optoelectronic properties of molecules on surfaces depends strongly on their adsorption geometry and environment as determined, using molecular resolution atomic force microscopy. The absorption of H_2Pc in a flat lying geometry results in a narrow intense emission peak, but evolves to a broad emission feature for multilayer samples.

4.4 Growth and fluorescence of ZnPc thin films on hBN at room temperature

In this section, metallated phthalocyanine (ZnPc) molecules were deposited using the previous sublimation process in vacuum system. When the vacuum system had reached its base pressure, the Knudsen cell was heated to 195°C. Figure 4.27 (a,b) show the morphology of a sub-monolayer of ZnPc on the hBN/SiO_2 surface.

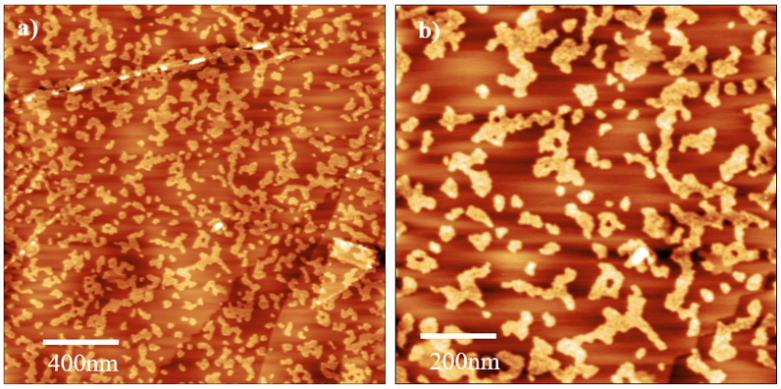


Figure 4.27: a,b) show AC mode AFM image of sub-monolayer thin film of ZnPc on hBN substrate at room temperature on different scale size.

The topography of thin film surface of ZnPc reveals an aggregate with a height consistent with molecules adsorbed in a non-planar geometry. The AFM image, see Figure 4.28 (a), and the profile in (b) shows the height of this island which is around 0.6 $\pm$ 0.1 nm.

Figure 4.29 shows the fluorescence spectra of ZnPc monolayers measured from two different hBN flakes, with the strongest peaks at 1.82 eV. Relative to the 0-0 peak in ZnPc in the gas phase (1.9 eV) [125], the peak was red shifted by ΔE= 0.08 eV. A similar observation was made for H_2Pc.The intensity of PL from these molecules is low in comparison with H_2Pc.

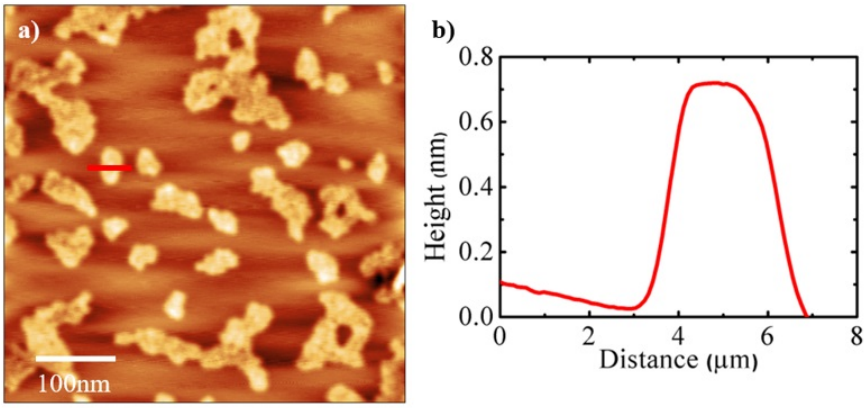


Figure 4.28: a) AC mode AFM image of sub-monolayer thin film of ZnPc on hBN substrate at room temperature; b) the height profile of an islands profile is across red line in (a).

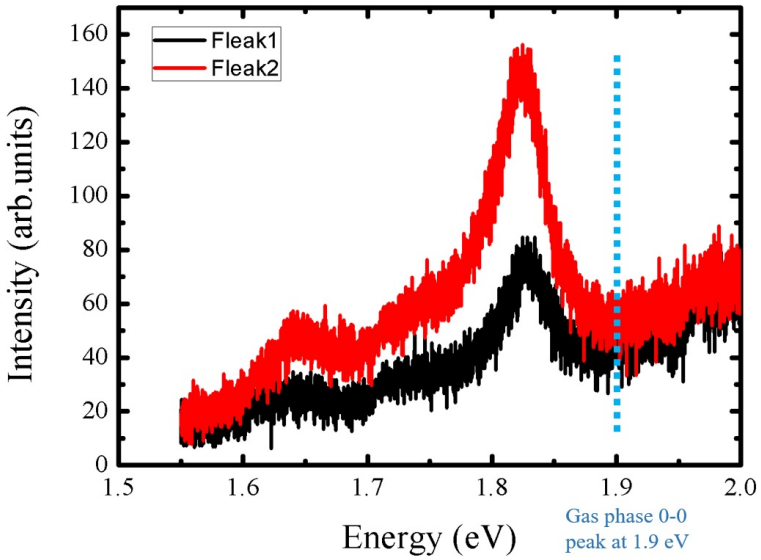


Figure 4.29: The fluorescence spectra of a submonolayer of ZnPc film. These particular spectra were taken from two different hBN flakes as shown in different lines colours.The gas phase zero phonon line of ZnPc is indicated with a blue dashed line.

4.5 Summary

In this chapter, the morphology and fluorescence of sublimed H_2Pc and ZnPc onto hBN/SiO_2 has been investigated. A 0.7 ML coverage of H_2Pc was deposited onto

hBN/SiO_2 for a range of substrate temperatures and was found to form needle like islands both at both room temperature and higher temperature, the molecular packing was also explored using high resolution AFM. The coverage dependence and the effect of increasing the amount of the deposited material from 1 nm to 32 nm equivalent thicknesses was also investigated. The influence of increasing the substrate temperature from room temperature up to 520°C on the morphology was observed. The aggregated islands start to dewet from the surface with increasing substrate temperature. Finally, the fluorescence of sublimed H_2Pc and ZnPc on hBN has been investigated.

CHAPTER 5

NTCDI thin films and heterostructure of organic molecules on hexagonal boron nitride

Naphthalenetetracarboxylic diimide (NTCDI) is a small organic molecule with a planar structure (see Figure 5.1), which is optically active and fluoresces in the blue region of the visible spectrum. This molecule is great interest to the organic electronics community and also has been used in a number of supramolecular chemistry studies [126]. In order to optimise the properties of organic devices containing NTCDI, structural control at a molecular level is an important parameter to engineer. Sequential deposition of different molecular species enables the formation of heterostructures, which represents a promising way to engineer the functional properties of organic devices as well as enabling the growth of model heterointerfaces [18, 127–131]. The characterization of organic heterostructures at the molecular scale using STM has been carried out on graphite and noble metal surfaces. However, effects such as fluorescence

quenching and strong coupling to the substrate lead to difficulties in elucidating the functional properties of such devices, particularly in technologically relevant configurations. However, it can be noted that techniques such as scanning tunnelling luminescence microscopy (STL) differential reflectance spectroscopy (DRS) and scanning tunnelling spectroscopy (STS) of electronically decoupled molecules are powerful techniques which can be used to measure functional properties of molecular assemblies on conductive substrates [132–134]. A more wholesale and technologically relevant approach is to study optical properties of molecular self-assemblies on insulating substrates.

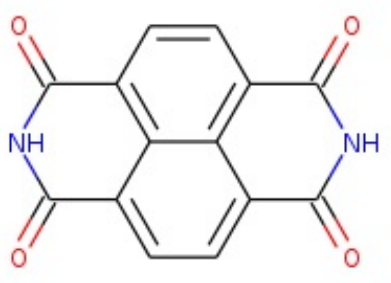


Figure 5.1: The chemical structure of NTCDI.

Molecular nanostructures can be assembled on insulating surfaces, which facilitate fluorescence and other spectroscopic measurements, as recently demonstrated by groups such as those of Peter Grutter (McGill), Moritz Sokolowski (Bonn), Torsten Fritz (Jena) and the Nottingham Nanoscience group [16–19, 57, 122, 135–137]. The approach of the Nottingham Nanoscience group demonstrated that atomic force microscopy (AFM) under ambient conditions can be used to acquire images of molecules on an insulating surface with molecular resolution, allowing for the correlation of supramolecular order and optical properties. Specifically, it will be shown that the fluorescence of monolayer-thick supramolecular assemblies formed on the hexagonal boron nitride (hBN) surface

may be measured as discussed in an earlier chapter [17, 19, 57, 137] and, in a separate study, that epitaxial supramolecular heterostructures may also be formed on hBN [18]. In this chapter, the growth of monolayer and sub-monolayer coverage films of NTCDI on hBN, sublimed under UHV conditions, will be explored at a range of growth temperatures and coverages. The morphology and optical properties of these layers was explored using AFM and fluorescence microscopy.

In addition, heterostructures have been formed by sequentially depositing two species of organic semiconductors; NTCDI on PTCDI, PTCDI on NTCDI. All these heterostructure were grown on hBN. This study builds upon previous investigations of PTCDI on hBN by Kerfoot et al. [17].

The study of NTCDI thin films was conducted in two stages; initially, a series of samples were grown with a coverage of 0.3 ML and increasing substrate temperatures ranging from room temperature up to 120°C. A set of samples were then grown at a fixed substrate temperature of 120°C with coverages of 0.3 ML, 0.7 ML and 0.97 ML. In addition, coverages of 0.3 ML and 0.7 ML were grown at room temperature.

5.1 Growth of sub-monolayer NTCDI at room temperature

In order to explore the growth of sublimed NTCDI on hBN, similar procedures as discussed in chapters 3 and applied in chapter 4 will be followed. In this investigation, NTCDI powder synthesized by the Champness supramolecular chemistry group at Nottingham University was used as source material. Once the vacuum system had reached its base pressure (approximately $1x10^{-8}$ mbar) the Knudsen cell was heated to 190°C. The hBN substrate was also annealed in vacuum to 450°C in order to remove any adsorbed contaminants due to exposure to ambient conditions. The QCM

was used to measure the deposition rate, allowing the dose of material deposited to be controlled.

A sub-monolayer coverage of NTCDI, grown on hBN at room temperature was found to form anisotropic monolayer islands, see AFM images as shown in Figure 5.2 (a), from which a coverage of 0.34 $\pm$ 0.04 ML was extracted. The island height extracted from AFM height profiles was found to be 0.3 $\pm$ 0.1 nm, as shown in Figure 5.2 (b), and confirms that NTCDI islands form monolayers which are co-planar with the hBN surface. The islands have average length and width of 0.4 $\pm$ 0.2 μm and 0.15 $\pm$ 0.04 μm, respectively.

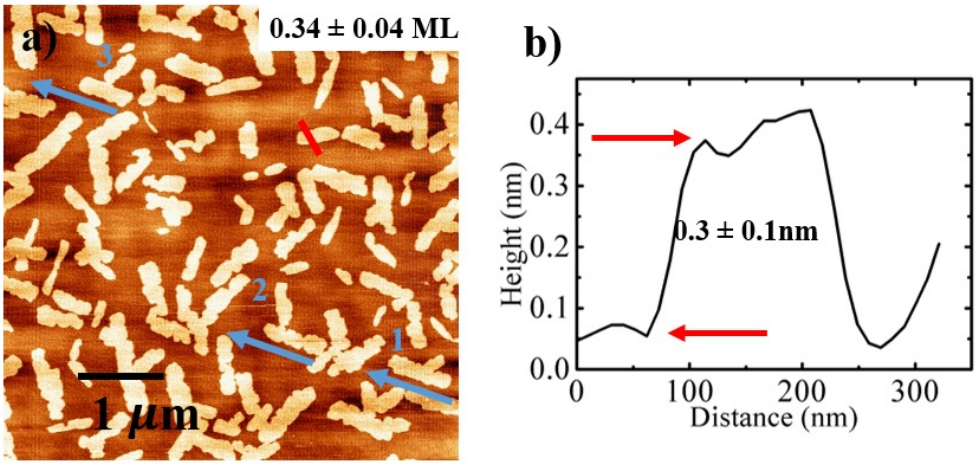


Figure 5.2: a) AFM images of 0.3 ML of NTCDI grown on hBN on SiO_2 at room temperature. The three blue arrows indicate islands which are parallel; b) The height profile was extracted from the region indicated by a red line in (a) which confirms the islands lay flat on the surface.

It was noticed that a number of the anisotropic islands grown at room temperature shared a common orientation; three such islands are indicated by blue arrows in Figure 5.2 (a). The distribution of island orientations have been extracted from the AFM images shown in Figure 5.2 and are plotted as a histogram as shown in Figure 5.3. The

presence of three major and three minor peaks with 60° separations between them in the orientation distribution of NTCDI is indicative of series of preferred island orientations on the crystalline hBN substrate. This result suggests that the molecules in the NTCDI layers adopt preferential registries with the hBN substrate in order to maximise their adsorption energy.

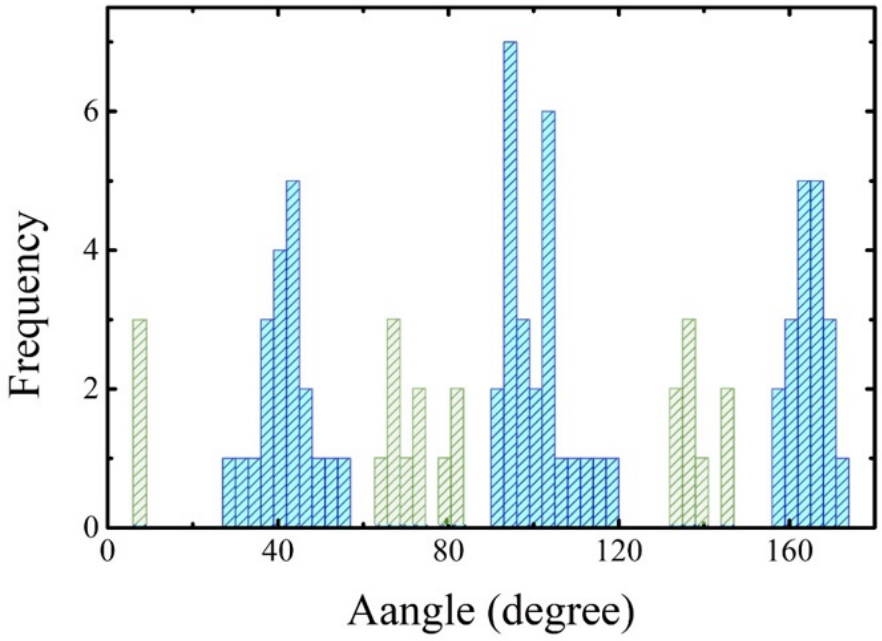


Figure 5.3: The distribution of individual NTCDI islands preferential orientations of individual NTCDI islands was extracted from the AFM image shown in Figure 5.2 using Gwyddion and are plotted as a histogram. The separation between three major and three minor peaks is 60° as expected for the hBN lattice.

5.2 NTCDI on hBN: temperature dependence

In order to investigate the effect of the growth temperature on the morphology of sub monolayer NTCDI films, a series of films were grown on hBN substrates at substrate temperatures ranging from room temperature to 120°C as shown in Figure 5.4. The

dose of sublimed material was held constant across all samples, this corresponded to a coverage of approximately 0.3 ML. For comparison, all the images in Figure 5.4 are of the same size.

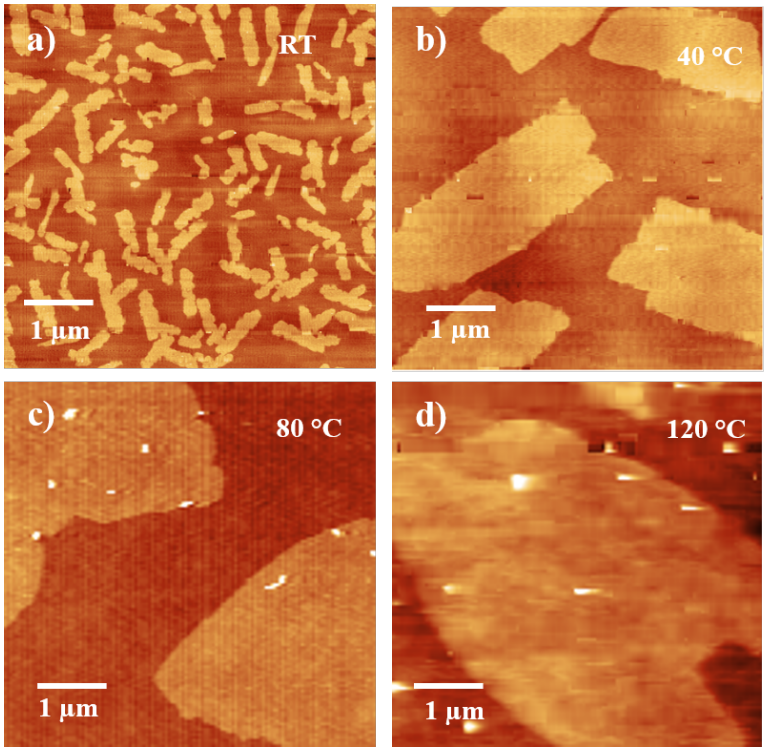


Figure 5.4: AFM images of NTCDI grown on hBN on SiO_2 at substrate temperatures of: a) at room temperature; b) 40°C ; c) 80°C, and d) 120°C.

As previously described, at room temperature the monolayer was observed to grow in islands with an anisotropic shape. As the temperature is increased, the shape of these islands changes from high aspect ratio rectangles towards an unusual shape, as seen in Figure 5.4.

As the substrate temperature during deposition was increased to 40°C, the size of NTCDI islands was found to increase while the appearance of islands did not change. These islands have a length and width of 2.3 $\pm$ 0.8 μm and 1.0 $\pm$ 0.3 μm, respectively.

The profile seen in the Figure 5.5 inset, confirms that these islands are monolayers as shown in Figure 5.5 (a-c).

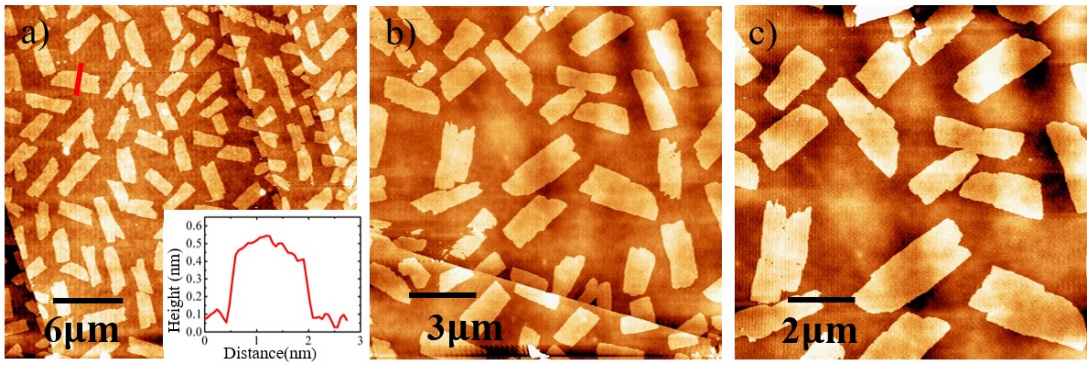


Figure 5.5: (a-c) AFM images of 0.3 ML of NTCDI grown on hBN on SiO_2 at 40°C ; the inset in (a) shows the topography profile along the red line in (a) which confirms the island grown is monolayer.

When the substrate temperature was further increased to 80°C and 120°C, the islands become less elongated, with a lily-pad like appearance, see Figure 5.6 (a and b). The mean length and width respectively of the islands grown at 80°C were found to be 4.0 $\pm$ 0.7 μm and 4.0 $\pm$ 0.9 μm, while values of 5.0 $\pm$ 0.9 μm and 4.0 $\pm$ 0.7 μm were extracted for a growth temperature of 120°C.

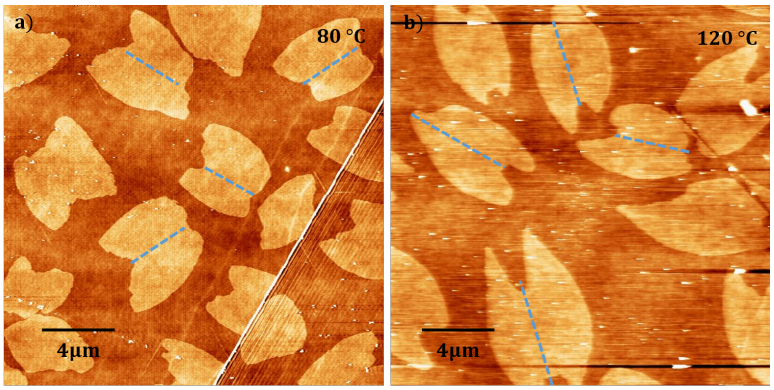


Figure 5.6: AFM images of 0.3ML coverage of NTCDI grown on hBN on SiO_2 at substrate temperatures of: a) 80°C; b) 120°C, both image show the island lily-pad shape. The blue dashed line show the line of symmetry islands.

These lily-pad islands have a plane of approximate symmetry, as seen from the dashed blue line in Figure 5.6. A possible explanation for this symmetry in relation to the crystal structure is described below. For NTCDI we have not been able to acquire images with molecular resolution. However, previous studies of NTCDI, both on surfaces and in the bulk crystal structure have identified a head-to-tail arrangement stabilised by hydrogen bonding. Figure 5.7 (a) shows the arrangement determined for NTCDI adsorbed on Au(111) [62]. Similar arrangements have been reported on other substrates [58–61]. The square-molecular NTCDI network was adapted from reference [19] and a possible arrangement is shown in Figure 5.7 (b). Each molecule is connected to the six nearest neighbours by eight hydrogen bonds, making this a stable arrangement. The angle of the unit cell was calculated to be $\alpha = 88^{\circ}$ [62] as shown by the red rectangle line. We explain this shape as arising from twinning of two crystals on the surface. The continuous blue lines indicates the facet of the islands and the mirror symmetry plane is the blue dashed line. The facet line is reflected on either side of the symmetry line, due to twinning between the different regions. This phenomena of twinning that leads to mirrored domains, and the lily-pad structure, is common in crystal growth where two (or more) different orientations of the same structure leads to similar growth at different angles [62].

In order to quantify the morphology, the island density and size are extracted from AFM images using Gwyddion and plotted against the substrate temperature. In Figure 5.8, the island density is plotted for a range of substrate temperatures during deposition. As expected as the substrate temperature is increased, the island density was found to decrease, see Figure 5.8.

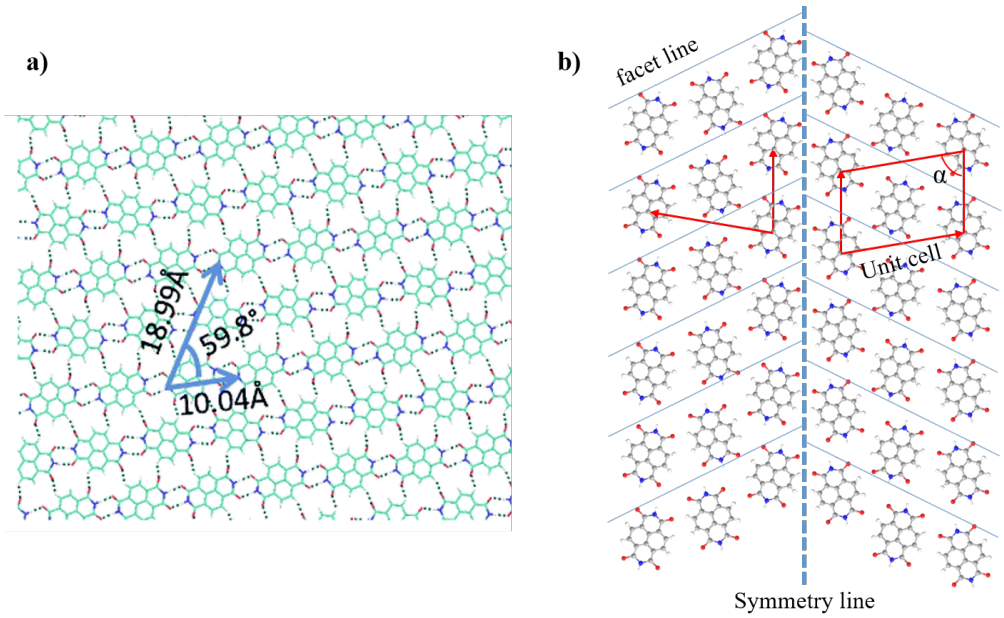


Figure 5.7: (a) The NTCDI molecules deposited on Au(111) substrate [62]; (b) The square molecular arrangement of NTCDI network and the symmetry line (blue dashed) reflected inexactly symmetric islands shape indicated with blue line where the unit cell in rectangle red line with angle $\alpha = 88^{\circ}$ which is adapted from the same reference.

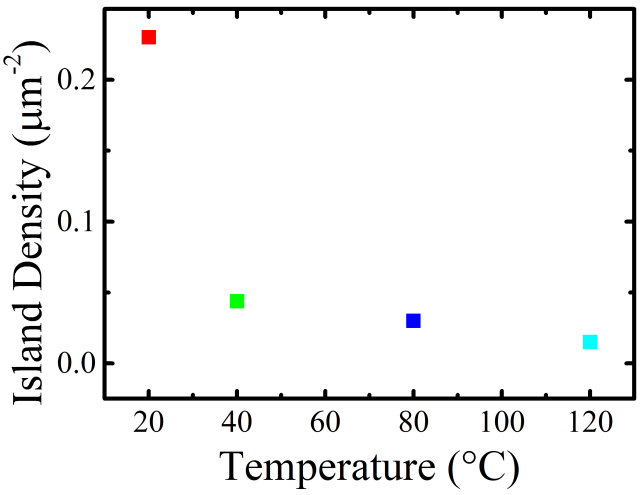


Figure 5.8: The islands density of NTCDI islands grown on hBN on SiO_2 was extracted from AFM images of sample grown at range of temperatures.

5.3 NTCDI on hBN: thickness dependence

In addition to the effect of the substrate temperature during the deposition, the morphology of NTCDI films with increased coverage was also investigated. The morphology of a 0.7 ML film of NTCDI grown at room temperature is shown in Figure 5.9 (a). The morphology of this sample is similar to the 0.3 ML coverage sample although, as expected, the islands were bigger. As for the 0.3 ML sample, see Figure 5.2 (a), the 0.7 ML coverage showed a preferential alignment. Second layers were not observed in AFM images, as confirmed by the height profile of these islands as shown in Figure 5.9 (b).

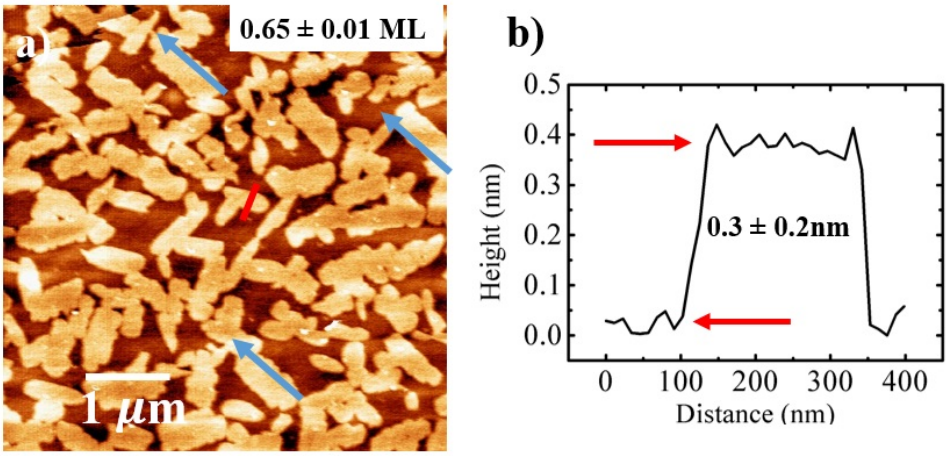


Figure 5.9: (a) AFM image of 0.7 ML coverage of NTCDI grown on hBN on SiO_2 at room temperature with the three blue arrows indicating parallel islands; b) The height profile taken along the red line in (a) which confirms the islands lay flat on the surface.

Another set of samples were grown at fixed substrate temperature of 120°C with a range of coverages. Figure 5.10 shows AFM images of the NTCDI thin films grown at 120°C with coverages of 0.7 and 0.97 ML respectively. The size of the islands has increased, while the island shape is similar to the 0.3ML coverage at substrate temper-

ature 120°C discussed in the last section, Figure 5.6 (b). At coverages up to 0.97 ML, no second layer was observed.

The islands of sublimed NTCDI thin films on hBN have monolayer height at room temperature and continue to be monolayer while increasing the temperature up to 120°C. These large monolayer islands were used as substrates for the growth of PTCDI as described in the next section.

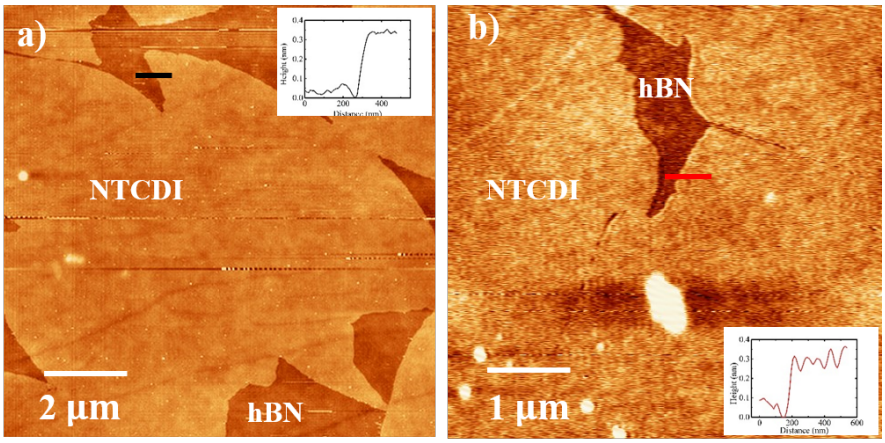


Figure 5.10: AFM images of NTCDI grown on hBN on SiO_2 at 120°C at; (a) 0.7 ML; and (b) 0.97 ML coverage.

5.4 Sequential formation of PTCDI/NTCDI heterostructures

After exploring and investigating monolayer and sub-monolayer coverages of NTCDI deposited on hBN, the formation of molecular heterostructures by deposition of two species of organic molecules was investigated. In this section, the formation of heterostructures produced by sequential deposition of PTCDI on NTCDI, and NTCDI on PTCDI on hBN (structure depicted in Figure 5.11) is discussed. The morphology and fluorescence were characterised using AFM and fluorescence microscopy respectively. A set of three samples were produced as follows: PTCDI deposited on top of

NTCDI with coverages of 0.3ML/0.7ML, 0.3 ML/0.97 ML, and 0.7 ML/0.97 ML for PTCDI/NTCDI respectively, see Figure 5.11 (a). A further sample of NTCDI on top of PTCDI with coverage of 0.7ML/0.97ML (NTCDI/PTCDI) was also grown , see Figure 5.11 (b). Finally, a three layer heterostructure was produced as NTCDI/PTCDI/NTCDI with coverage of 0.97ML/0.7ML/0.97ML respectively.

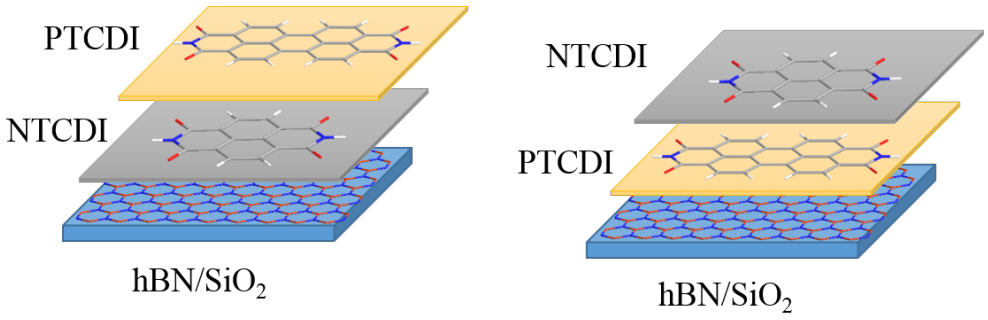


Figure 5.11: Illustration of the process of sequential deposition of distinct species of two organic molecules PTCDI and NTCDI on hBN.

5.4.1 PTCDI on NTCDI

The first heterostructure sample had 0.7 ML of NTCDI deposited on hBN at 120°C, followed by 0.3 ML of PTCDI deposited at substrate held at room temperature. As shown in Figure 5.12 (a), an AFM image of 0.3/0.7 ML of PTCDI/NTCDI, the NTCDI islands can be seen to exhibit the same morphology as seen previously in Figure 5.9 (a) with a lily-pad shape. The PTCDI islands have different morphologies on NTCDI and on hBN. In both cases the PTCDI islands form a flat-laying monolayer which is confirmed by the height profile in Figure 5.12 (c) taken from the red line in (b). These islands have average length of 0.28 ± 0.07 μm whereas the islands grown on hBN have an average length of 0.8 ± 0.2 μm which is consistent with the previously reported length of 1.2 ± 0.3 μm [17].

The distribution of PTCDI island orientations on the NTCDI were extracted from the AFM image shown in the Figure 5.12 (d) and is plotted as a histogram in (e). These islands are on a single NTCDI island. The presence of one major and two smaller peaks at 60° either side in the orientation distribution is indicative of preferred island orientations of PTCDI on NTCDI.

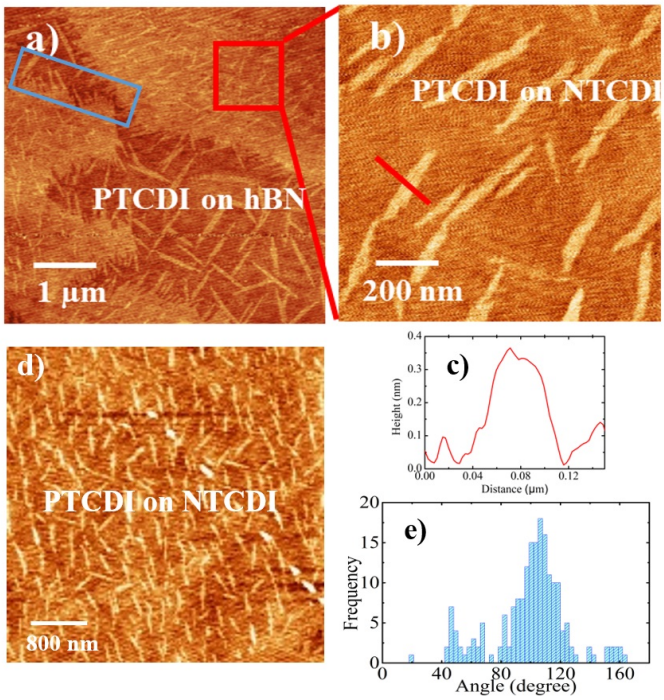


Figure 5.12: (a,b and d) AFM images of the PTCDI/NTCDI heterostructure grown on hBN on SiO_2 with thickness 0.3 /0.7 ML; (c) The height profile taken along the red line in (b) which confirms that a monolayer of the PTCDI islands where grown on top of NTCDI; (e) the orientations of PTCDI islands on NTCDI was extracted from the AFM image in the (d) using Gwyddion and is plotted as a histogram.

The coverage of NTCDI was increased to 0.97 ML, deposited with the substrate temperature held at 120°C, and the second layer of PTCDI kept the same as in the previous sample. As shown in AFM images in Figure 5.13 (a and b), the PTCDI islands grown on NTCDI/hBN have average length of 0.26 ± 0.06 μm which is the same as the previous

sample with the same coverage. The PTCDI island orientation is aligned as it was for the lower NTCDI coverage.

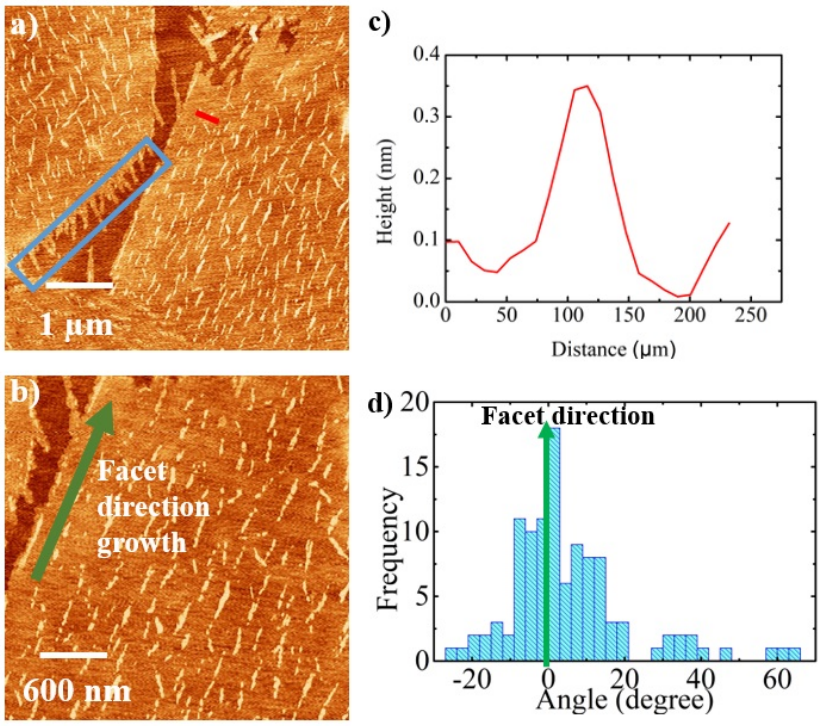


Figure 5.13: (a and b) AFM images of NTCDI/PTCDI heterostructure grown on hBN on SiO_2 where the deposition of these material was 0.3 ML of PTCDI on top of 0.97 ML of NTCDI; c) The height profile taken along the red line in (a) which confirms that a monolayer of the PTCDI islands where grown on top of NTCDI; d) The orientations of PTCDI islands on NTCDI were extracted from the AFM image using Gwyddion and have been plotted as a histogram.

The distribution of PTCDI island orientations was extracted from the AFM image shown in Figure 5.13 (b) and is plotted as a histogram as shown in Figure 5.13 (d). The distribution relative to the facet direction shows a single peak which corresponds to an alignment with the NTCDI facet direction indicated with green arrow in (b, d). The facet edge indicates the row direction which we associate with the direction of molecular rows of NTCDI. The dominant orientation of the PTCDI on the NTCDI is theorised

to be because the PTCDI aligns with the underlying NTCDI to give the islands the same orientation. This is clearest at the island edges, outlined by the blue rectangles in Figure 5.12 and 5.13 where one dimensional crystalline filaments grow. These are not observed along the straight facet in Figure 5.13 (a). The proposed structure for this is shown in Figure 5.14.

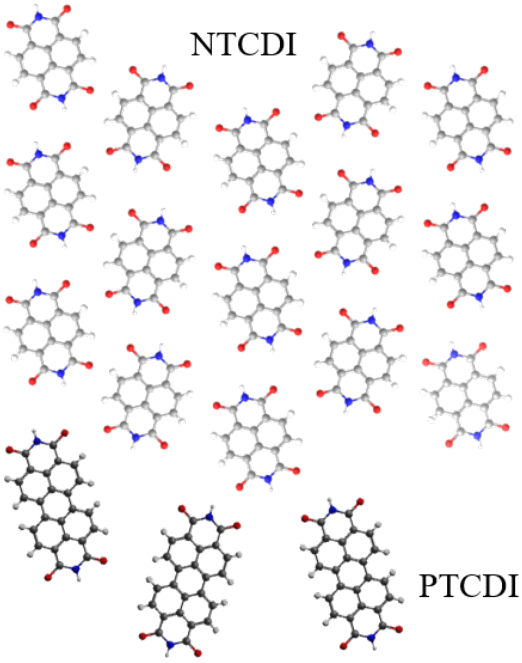


Figure 5.14: Proposed structure showing the alignment of growth for the PTCDI islands and alignment their with the facet edge of NTCDI molecules.

For the next sample, NTCDI coverage was kept the same (0.97 ML at 120°C) and the dose of PTCDI was increased to 0.7 ML. When compared to the 0.3 ML PTCDI sample, the islands are longer and appear higher, see Figure 5.15 (a). The average island length was found to 0.5 ± 0.1 μm, which is almost double the previous island lengths, consistent with this coverage increase.

Unlike the previous samples where only monolayer PTCDI islands were observed, the PTCDI islands on this sample form a mixture of monolayers and bilayers as shown from the island height distribution in Figure 5.15 (c).

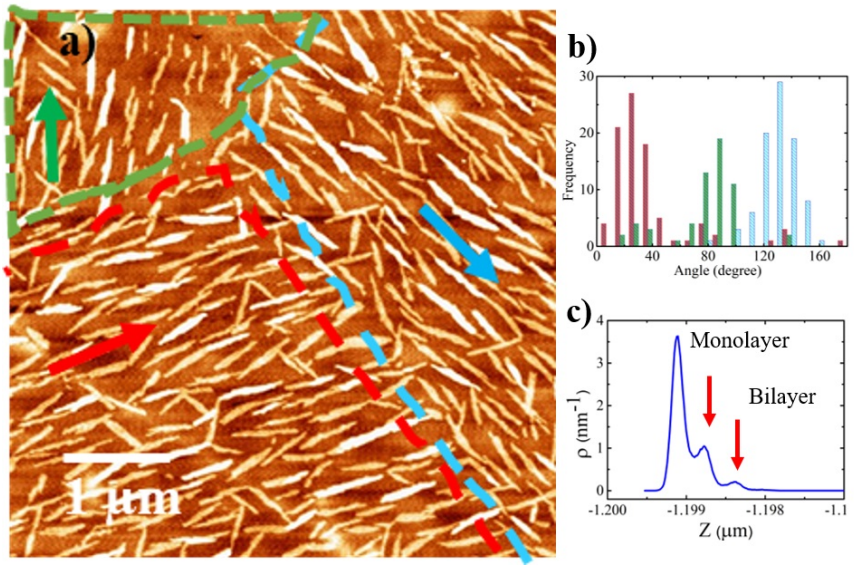


Figure 5.15: (a) AFM image of the NTCDI/PTCDI heterostructure grown on hBN on SiO_2 where the deposition of these materials was 0.7 ML of PTCDI on top of 0.97 ML of NTCDI; (b) the orientations of PTCDI islands on NTCDI were extracted from the AFM image using Gwyddion and is plotted as a histogram; (c) the islands distribution extracted from the same AFM image.

The island orientation of the PTCDI within what appears to be one island of NTCDI have three different regions as shown in Figure 5.15 (a) where the different colours of arrows in (a) indicate one preferred angle. The distribution of island orientations were extracted from the AFM image shown in Figure 5.15 and are plotted as a histogram as shown in Figure 5.15 (b). The three major peaks in the orientation distribution of PTCDI correspond to the three regions with a small amount of material aligned at 60° from the dominant direction in a region. This is consistent with the previous structure where the PTCDI molecules align with the underlying NTCDI molecules if this island is actually

three merged islands of NTCDI with different orientations. Merging of islands might be expected for this high coverage. Another example is shown in Figure 5.16.

Near the edges of the NTCDI islands, an absence of PTCDI islands on top of the NTCDI is seen, as shown by the red rectangle in Figure 5.16. In this Figure the phase of this image (b) shows the edge of NTCDI islands clearly and suggests that the PTCDI is also growing from the edges the hBN surface.

Additionally, areas of PTCDI bilayer were also observed on hBN as shown in Figure 5.16 (c) which shows the profile height of the red line in (a).

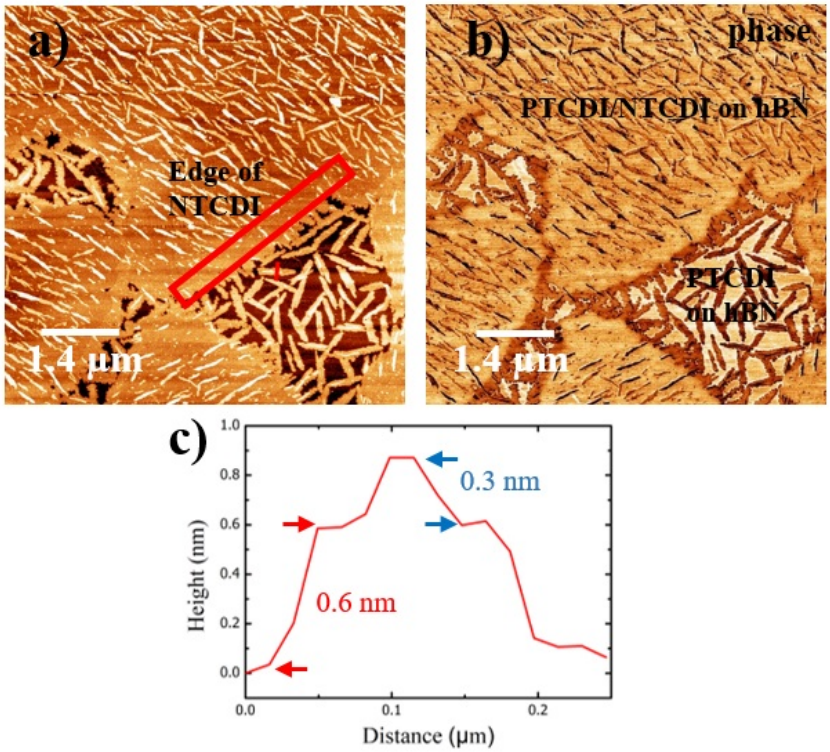


Figure 5.16: (a) AFM images of the NTCDI/PTCDI heterostructure grown on hBN on SiO_2 where the deposition of these materials was 0.7 ML of PTCDI on top of 0.97 ML of NTCDI; (b) the phase of this image; (c) The height profile taken along the red line in (a) which confirms that a monolayer grown on top of PTCDI bilayer island.

5.4.2 NTCDI on PTCDI

In a previous study by Kerfoot et al. [15], the growth of PTCDI on hBN with a fixed dose of 0.3 ML of PTCDI was investigated. As the substrate temperature was increased, the size of islands increased while their areal density decreased as shown in Figure 5.17. These islands were used as substrates for NTCDI deposition to form NTCDI/PTCDI heterostructure with the layer reversed from the previous section.

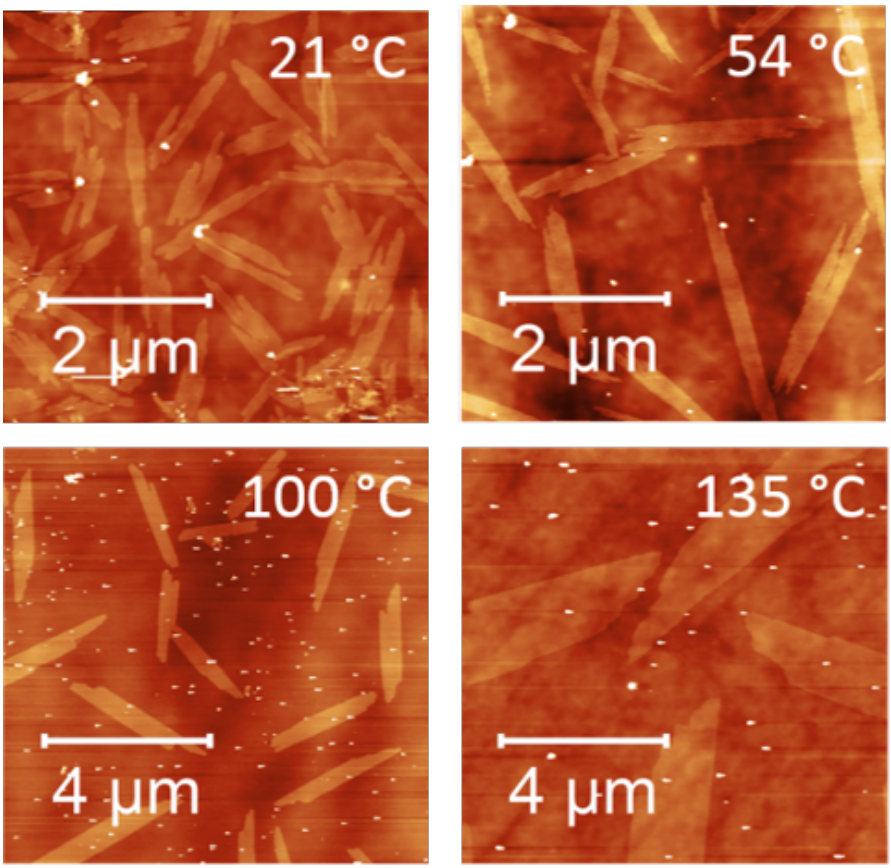


Figure 5.17: AFM images of a 0.3 ML dose of PTCDI deposited onto hBN substrates held at a range of temperatures, indicated in the top right hand corner of each image. Adapted from reference [15].

A 0.7 ML coverage of PTCDI was grown on hBN at an elevated substrate temperature of 120°C. NTCDI was then deposited with the substrate held at room temperature.

The NTCDI was found to form 3D islands on the PTCDI as shown in Figure 5.18, this suggests the growth mode of NTCDI on PTCDI is different to that on the hBN surface.

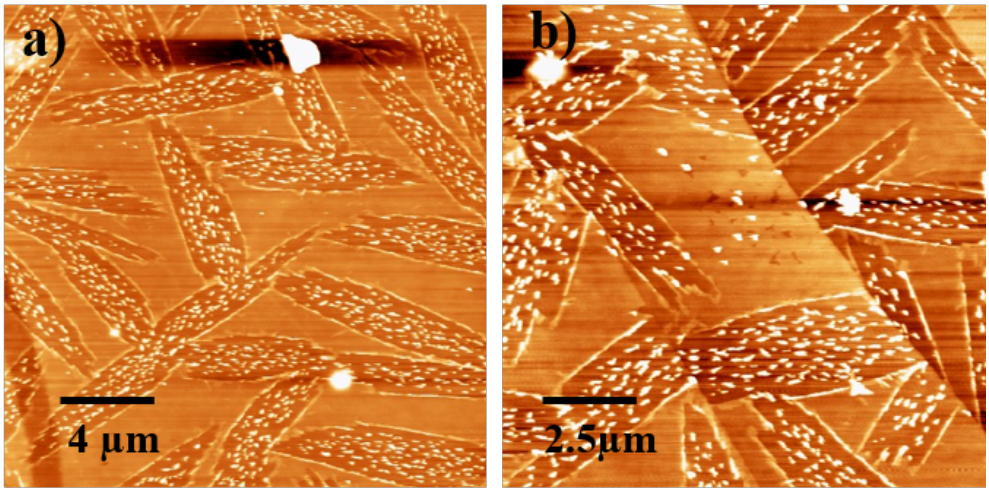


Figure 5.18: AFM images of heterostructure morphology of 0.7ML of PTCDI/ 0.97 ML of NTCDI grown on hBN/SiO_2.

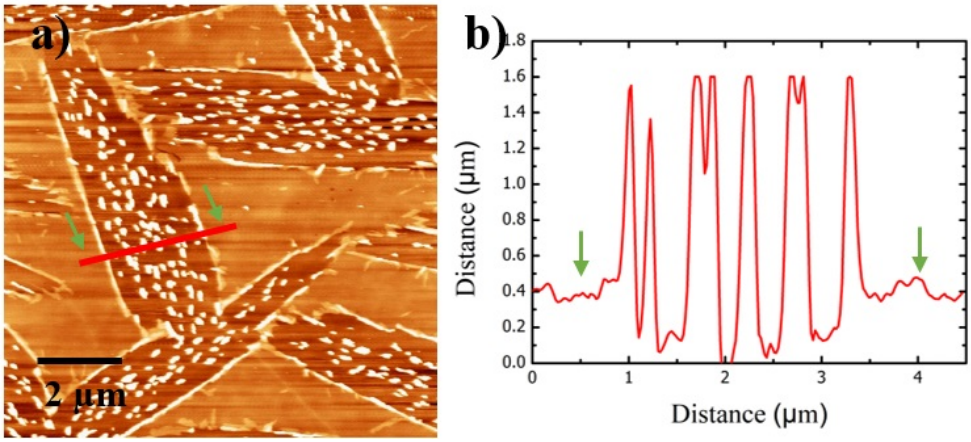


Figure 5.19: (a) AFM image of heterostructure morphology of PTCDI/ NTCDI grown on hBN on SiO_2 ; (b) the height profile of an island shown by a red line in image.

The NTCDI islands on the PTCDI have a height of ∼1.5 nm as shown in Figure 5.19. This suggests that the NTCDI molecules are not lying flat but are standing up on the PTCDI. This limits the usability of these heterostructures. In this Figure 5.19, the green arrow around the PTCDI islands edge corresponds to the height of a bilayer of NTCDI

molecules on hBN. This may be a stable structure or due to diffusing molecules. The observation on 'irregular/negative' step heights is suggestive of artefacts, possibly due to a change in the tip state at island edges or dramatic changes in the tip-sample potential between the two molecular surfaces.

5.4.3 NTCDI/PTCDI/NTCDI

Although flat lying NTCDI was not deposited onto PTCDI islands, heterostructures with NTCDI on top of the previously produced PTCDI/NTCDI heterostructures were investigated to see if the base layer of NTCDI stabilised the structure to allow for the deposition of the third layer. Further deposition of organic material has been achieved with three different layers, NTCDI/PTCDI/NTCDI, with coverages of 0.97 ML(RT)/0.7 ML(RT)/0.97 ML(120°C) respectively. The formation of sublimated molecular islands is difficult to track even for this relatively simple multilayer heterostructure. However, by comparing the AFM images to those obtained for the PTCDI/NTCDI heterostructure (Figure 5.15), it is clear that the top NTCDI layer has successfully grown on the PTCDI layer below, shown in Figure 5.20 as topography AFM images.

In Figure 5.20, the height profile in (c) shows bulk aggregates forming from NTCDI on PTCDI. Due to the incomplete PTCDI layer, it is unclear whether the NTCDI is depositing on top of the PTCDI or on top of the NTCDI around the PTCDI islands.

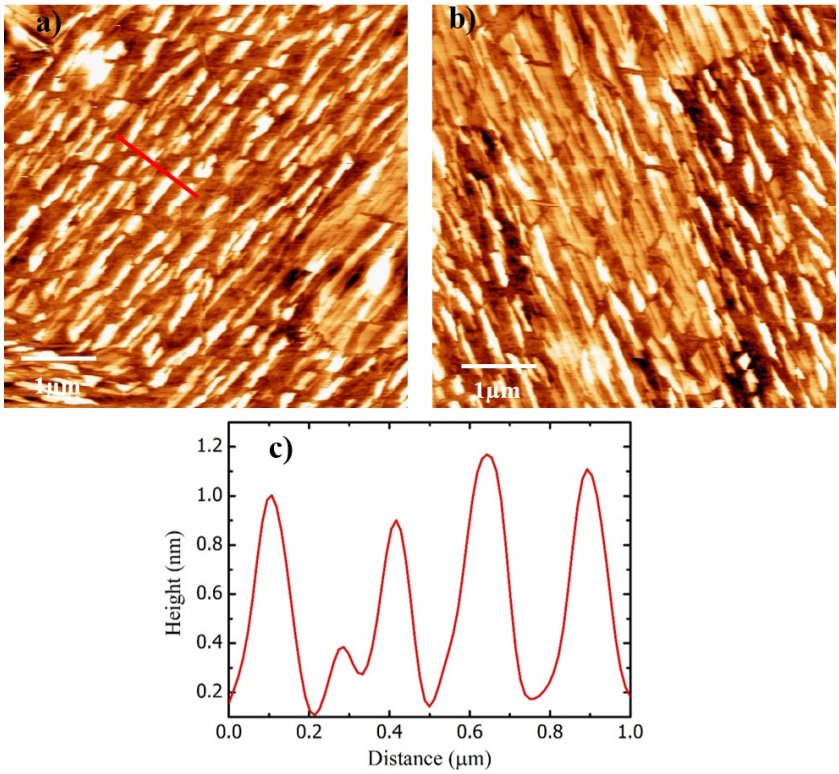


Figure 5.20: (a,b) AFM topography images of three layers of NTCDI/PTCDI/NTCDI heterostructure;(c) the height profile of an island shown by a red line in image (a).

5.5 The fluorescence of sublimed NTCDI and NTCDI/PTCDI heterostructure on hBN

One of the advantages of studying sublimed films of organic semiconductors on hBN is the possibility to explore their optical properties. Here the optical properties of NTCDI thin films sublimed on hBN by sublimation in vacuum will be discussed. However, there was a limitation in carrying out complete measurements since the photoluminescence (PL) emission of the NTCDI overlaps with the maximum emission of the 405 nm laser available for use in the physics department.

Figures 5.21 shows the fluorescence measurements of 0.3 ML coverage of NTCDI deposited at room temperature. Spectra recorded using a Horiba Raman system (avail-

able in the nmRC) with a 335 nm excitation source (UV laser) are shown in the inset of Figure 5.21, while the red line corresponds to measurements recorded using a 405 nm excitation laser, with the black line indicating the response of bulk powder of this material, again with the 405 nm laser.

For the spectra taken with the 405 nm laser, the lower wavelength peak is not present since it lies below the excitation wavelength. Instead a broad peak is observed (peak wavelength 489 nm) for the NTCDI monolayer film (red curve). A broad peak is also observed in the spectrum of bulk material confirming that NTCDI is the origin of the peak. This peak is characteristic of the NTCDI so confirms its presence on the surface.

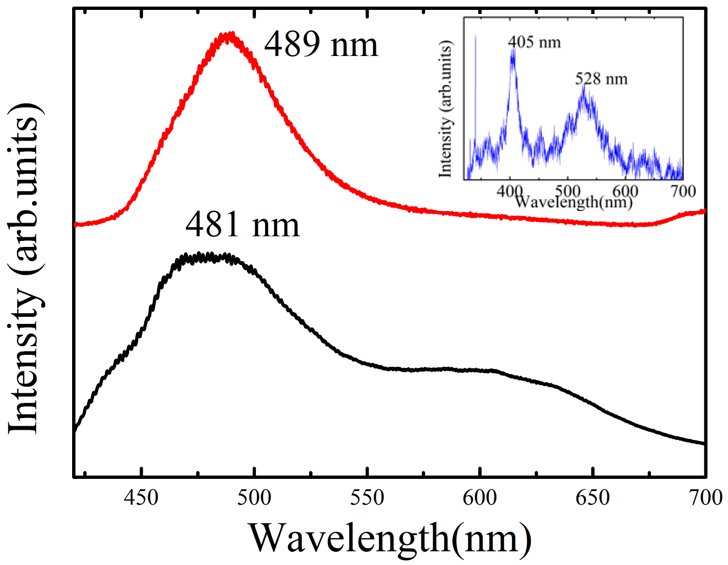


Figure 5.21: Fluorescence spectra of 0.3 ML of NTCDI on hBN, grown at room temperature, were measured using a 335 nm excitation source (blue line in the inset), a 405 nm excitation source (red). The bulk powder was also measured using a 405 nm excitation source (black).

The optical properties of the sequential heterostructure of PTCDI/NTCDI thin films sublimed on hBN by vacuum were investigated. The effect of PTCDI ad-layer of NTCDI

monolayer on the fluorescence using AFM and fluorescence microscopy was explored as shown in Figure 5.22.

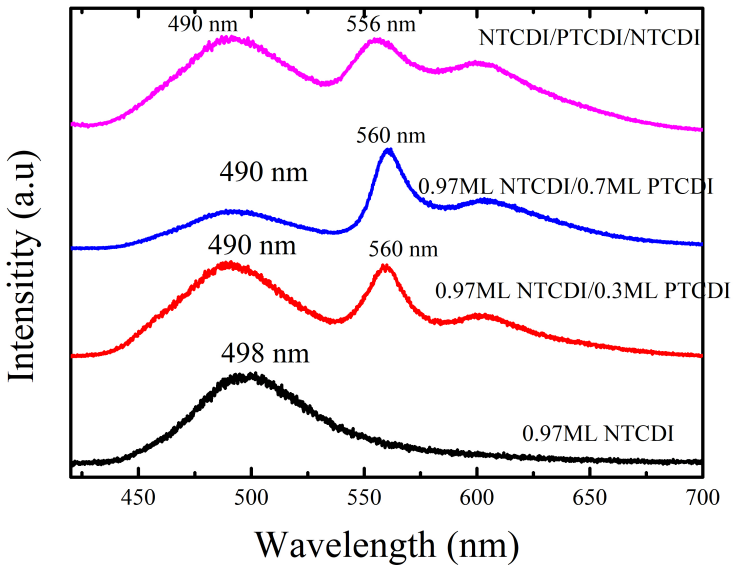


Figure 5.22: Fluorescence spectra from NTCDI and mixed NTCDI/PTCDI films on hBN, grown at a substrate temperature of 120°C. All spectra were acquired using a 405 nm excitation laser.

A fluorescence spectrum of 0.97 ML coverage of NTCDI deposited on hBN on SiO_2 at 120°C was acquired using 405 nm excitation laser. The peak is located at 498 nm, which is consistent with the peak seen for 0.3 ML coverage sample deposited at room temperature. For 0.97 ML of NTCDI coverage sample at 120°C, the peak shifted from 489 nm at room temperature to 498 nm.

Measuring the spectrum from the sample which has 0.97 ML NTCDI /0.3 ML PTCDI give the 0-0 peak of PTCDI located at 560 nm and it is consistent with the previous study of these molecules. The NTCDI peak is still present at 490 nm. Accordingly to increase the PTCDI coverage to 0.7 ML, the PTCDI intensity shows an increase and the

NTCDI peak is quenched. For three layers heterostructure the PTCDI peak is quenched and shifted ∼4 nm, this could be due to second NTCDI layer.

5.6 Summary

In this chapter, the morphology and fluorescence of sublimed NTCDI on hBN has been discussed. Firstly, the temperature dependence of the morphology of sub monolayer NTCDI islands was investigated. At room temperature, a sub monolayer coverage of sublimed NTCDI forms the anisotropic monolayer islands. As the temperature is increased, the size of these islands increases and the transformation of their morphology into lily-pad shape islands have been studied. Secondly, the coverage dependence at fixed substrate temperature of sub monolayer NTCDI islands was explored. For a growth temperature of 120°C, a set of samples were produced with a range of coverages up to 0.97 ML.

In addition, the heterostructure of two species of organic molecules has been explored. The sublimed PTCDI on top of preformed NTCDI islands with different coverages was investigated. This heterostructure revealed that the PTCDI islands can grow on top of NTCDI. However, flat laying NTCDI islands did not grow on PTCDI.

It has been shown clearly that even for these rather similar molecules it is not possible to grow controlled heterostructures and this stimulates further studies of the formation of organic thin films for device applications.

CHAPTER 6

Encapsulating PTCDI between hBN layers

Van der Waals heterostructures, which consist of vertical stacks of layers of two dimensional materials, are of great interest to the nanoscience community as they enable structural control in the out-of-plane direction with sub-nanometre precision [138, 139]. This level of structural control can then be harnessed in order to fabricate novel device architectures which utilise boron nitride tunnel barriers [140–142] or to engineer states such as inter-layer excitons [143].

The introduction of organic molecules, specifically well-ordered monolayers, into the interfaces of 2D layers in van der Waals heterostructures is an interesting prospect for a number of reasons. Firstly, encapsulation with hBN is expected to enhance the thermal stability of organic materials, which may enable processing steps promoting phenomena such as polymerisation. Secondly, encapsulation can be used to control both the dielectric environment and the pressure experienced by organic molecules [144], which may be used to influence the functional properties of the encapsulated layer. Finally,

introducing organic molecules into the interfaces of van der Waals heterostructures has been demonstrated to lead to charge transfer excitons between the organic layer and a transition metal dichalcogenide layer [145, 146]. 2D materials such as hBN are prime candidates for creating heterostructures due to their atomically thin structure, electronic properties, and the ability to create high quality interfaces. The quality and cleanliness of these interfaces are of high importance to fabricate sophisticated devices with high performance [147]. Fabrication is carried out using stamping techniques, the technique used here involves picking up mechanically exfoliated hBN and graphene flakes with PPC/PDMS fabricated stamps where the preparation process has been discussed earlier in Chapter 3. Combining this with PTCDI deposition allows for sandwiched heterostructures (hBN/PTCDI/hBN) to be formed. Once encapsulated within a heterostructure, the change in the properties of the molecular layer due to the presence of the additional interface can be studied. One example of such a change is that the additional layer may modify the local chemical and dielectric environment, leading to chromatic shifts. These shifts can be easily measured by monitoring the fluorescence before and after additional layers are added.

In this work, heterostructures of hBN thick flakes and monolayers of PTCDI were formed using different approaches and the change in the properties of the encapsulated material was explored with photoluminescence (PL).

6.1 Transfer of flakes by mechanical transfer

To pick up an hBN flake in order to cap a molecular layer mechanically, transfer/stamping apparatus is used, as discussed in Chapter 3. The hBN on SiO_2 was prepared as described in Section 3.5. The substrate containing the target hBN flake for transfer is

flame annealed and placed on the stamping stage before being heated to 50°C. Once this temperature is reached, the stamp is aligned and brought into contact with the target flake which is to be picked up. Once the polymer stamp is in contact with the target flake, the stamp is retracted. If successful, the target hBN flake will be picked up by the polymer stamp. The pickup process is outlined in Figure 6.1.

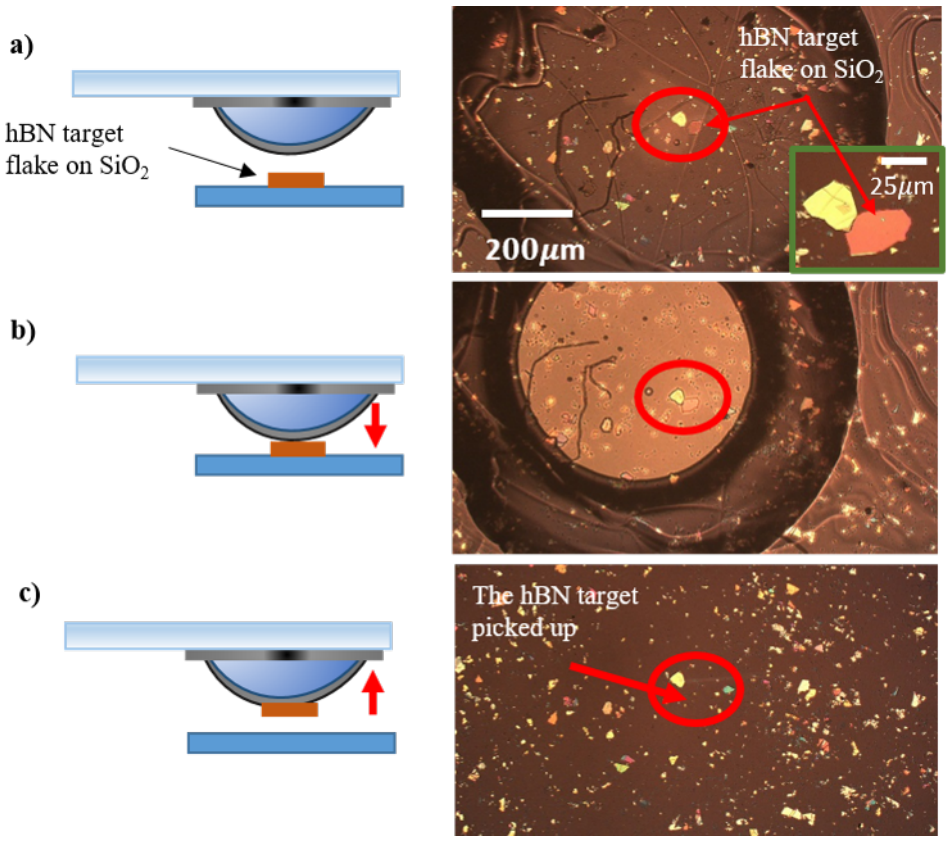


Figure 6.1: Flake pick up process of flame annealed hBN on Si_2 where: a) polymer stamp is aligned on targeted hBN flake on SiO_2 ; b) once the polymer stamp is brought down and aligned with the hBN flake, the substrate stage is heated to 50 °C; c) hBN flake is picked up as the stamp is retracted.

In order to deposit the hBN flake deterministically, the hBN flake on the polymer stamp is aligned and brought into contact with a flake on a second substrate. In many experiments there is a sublimed layer of molecules on this second flake. The stage is then heated to 110°C. At this temperature, the polymer starts to peel off from the top of the

stamp, leaving a stack of one hBN flake on top of another hBN flake with an embedded molecular monolayer. The process flow for heterostructure fabrication and hBN flake transferral is outlined as shown in Figure 6.2.

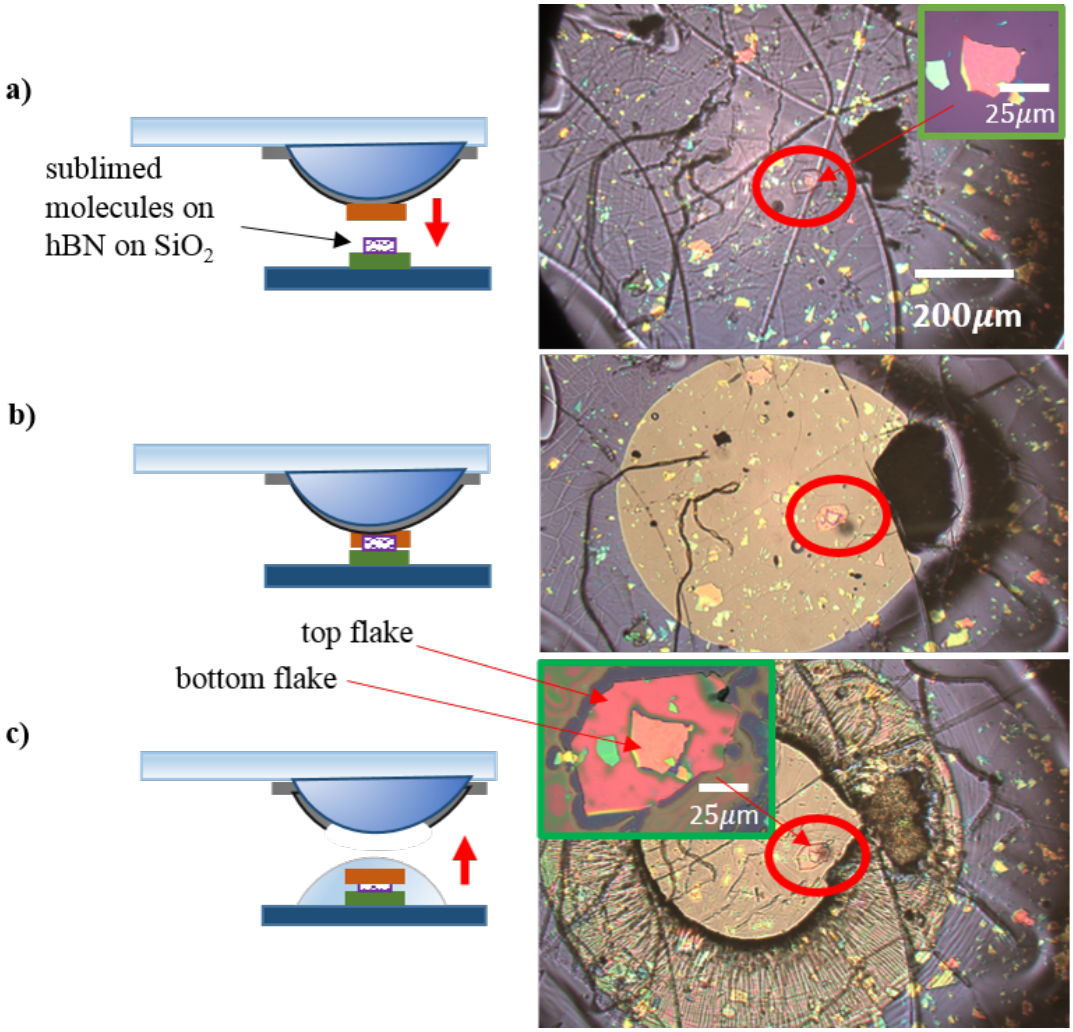


Figure 6.2: Process flow for heterostructure fabrication and flake transfer using PPC as the adhesive polymer on top of PDMS as elastomer where: a) The hBN flake stacked on the polymer stamp is brought down to the second substrate with sublimed organic molecules on top of hBN on SiO_2; b) Once the hBN flake is in contact with the specific flake to capsulate, the stage is heated to 110 °C; c) The polymer stamp is retracted to leave the fabricated heterostructure on top of the substrate.

Figure 6.3 shows images acquired before and after the stamping of capping layers of hBN, before cleaning the residue from the transfer polymer. Prior to the deposition of a top hBN flake, the PTCDI islands are optically visible as a difference in contrast on the hBN layer, see Figure 6.3 (a,c). These islands are still observed as a difference in the contrast after the stamping procedure, see Figure 6.3 (b,d).

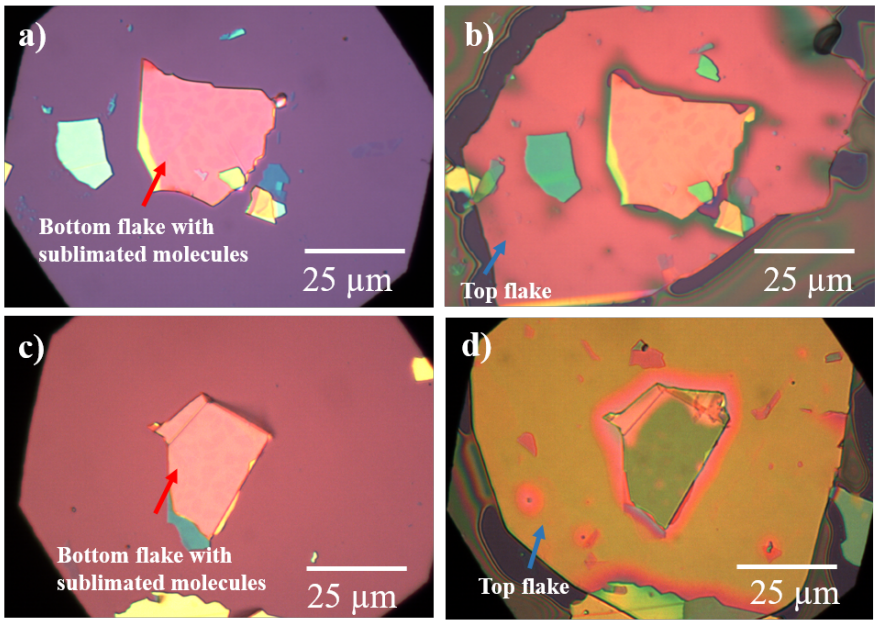


Figure 6.3: Optical images of two hBN flakes before (a,c) and after (b,d) stamping.

6.2 Different cleaning approaches

In this section, after trapping the PTCDI molecules using the flake transfer technique discussed above, the effect of different cleaning methods has been investigated. This involved measuring the fluorescence of structures cleaned through different approaches: furnace and solvent cleaning separately.

6.2.1 Furnace clean

In this study, two hBN flakes are fabricated as described previously. The first hBN flake was exfoliated onto the SiO_2 substrate followed by PTCDI deposition. Next, the second hBN flake was stamped on top using PPC, as described above, in order to encapsulate the molecules. The PPC is then removed by annealing in an atmosphere of hydrogen and argon H_2/Ar (5:95) to 250°C for 4 hours, with PL measurements acquired before and after. Following PL results, the samples was heated to 250°C for 4 hours a second time, followed by a third time at 300°C for 4 hours. Finally, the sample was heated at 400°C for 4 hours. After each individual heating procedure, PL measurements for the sample were acquired. These can be seen in Figure 6.4.

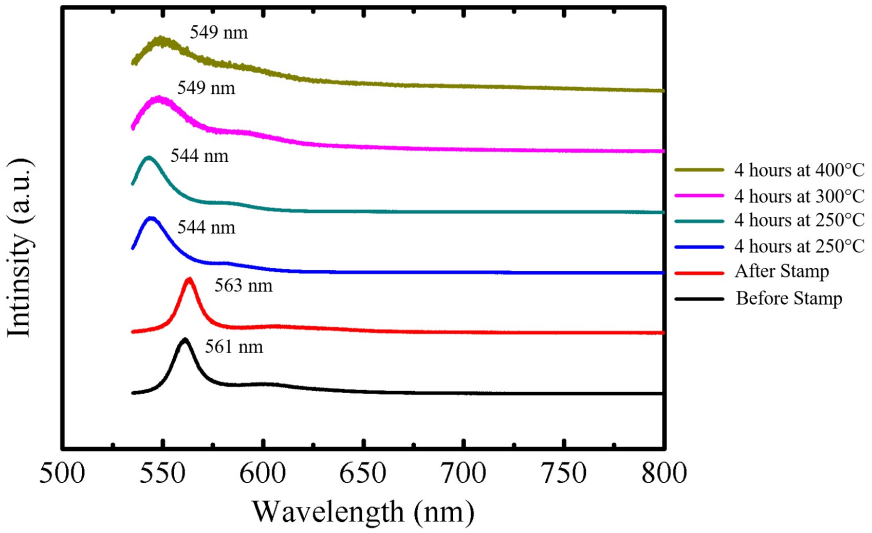


Figure 6.4: PL measurements for PTCDI molecules at various stages of encapsulation and cleaning in the furnace.

Fluorescence spectra were acquired from these heterostructures using the Horiba LabRAM HR spectrometer (532 nm excitation laser). The PL measurement for the deposited PTCDI molecules on hBN in Figure 6.4 shows a peak at 561 nm which is in good agreement with earlier results for PTCDI on hBN [16]. Encapsulation was found to lead to

a red shift of ∼2 nm. The resilience of the encapsulated molecules to decomposition upon annealing in the furnace was investigated and results are also shown in Figure 6.4. The encapsulated molecules were then heated for 4 hours at 250°C and the PL peak was blue shifted to 544 nm. Secondly, the sample was heated for 4 hours at 300°C. After this, the peak was red shifted to 549 nm and the intensity was low. Further heating for 4 hours at 400°C gave a very low intensity unshifted peak.

6.2.2 Solvent clean

For the second sample, prepared in the same way as the previous sample, the polymer was removed by immersion in chloroform . Next, the sample was heated twice in the furnace for 4 hours at 250°C, as carried out with the previous sample. This was also followed by a further heating at 300°C, and 400°C, both for 4 hours. PL measurements were recorded between each solvent cleaning/heating step see Figure 6.5.

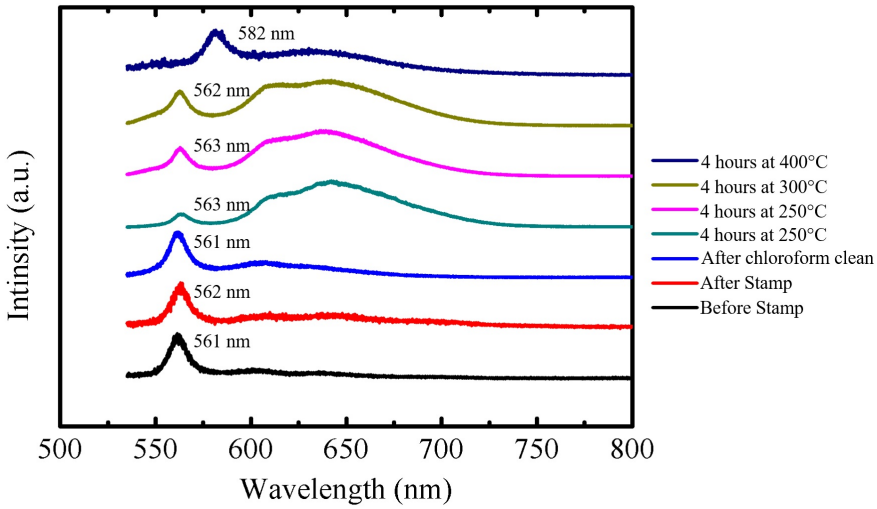


Figure 6.5: PL measurements for PTCDI molecules at various stages of encapsulation, cleaning with solvent, and furnace heating.

As above, fluorescence spectra were acquired using the Horiba LabRAM HR spectrometer. The PL measurement after encapsulating the molecules shows a red shift of $\sim$1 nm. Post chloroform cleaning, the spectra matched that for prior to stamping. Following the solvent cleaning, the heating procedure used a the previous sample was repeated. First, the encapsulating molecules were heated twice for 4 hours at 250°C, with an observed red shift of $\sim$2 nm. Second, the sample was heated at 300°C for 4 hours, with a low intensity peak at 562 nm, in addition to the appearance of additional peaks at wavelengths greater than 600 nm, corresponding to the position of the vibronic peak of PTCDI. Finally, the sample was annealed for 4 hours at 400°C, after which the peak is red shifted by $\sim$20 nm with the vibronic peak still present with low intensity [148].

6.3 Comparison of different cleaning methods

As seen above different PL shifts are observed upon carrying out different cleaning methods. In the case of furnace cleaning, where the PPC was removed by annealing in the furnace at 250°C, there is dramatic blue shift in the PL peak. This blue shift could due to the polymer at this temperature not being removed from the flake completely and may be infusing between two hBN layers. This would change the local environment of the molecule, leading to chromatic shifts due to processes such as solvatochromism and a change in the adsorption geometry of the molecules. For the case where solvent cleaning is carried out prior to furnace heating, the PPC was removed from the flake prior to annealing and did not lead to shifts in the photoluminescence peak up to 300°C, suggesting there is no change to the local environment of the PTCDI molecules. Blisters within the heterostructure lead to areas within the heterostructure

which are not fully encapsulated, such that the second BN interface is not in contact with the molecular layer, hence there would exist two different dielectric environments for molecular layers within the heterostructure, with their associated resonant and non-resonant interactions giving rise to differing optical signatures.

Upon annealing to 400°C, only one red-shifted peak was seen in the photoluminescence, which tentatively assign to the removal of blisters from the heterostructure, giving rise to a homogenous dielectric environment for molecules within the heterostructure, presumably due to full encapsulation. The observed red-shift upon annealing to 400°C is consistent with the experimental results of Svatek et al. and calculated resonant and non-resonant shifts [148].

It is suspected that the reason this effect is not seen at low temperature is that contamination (either atmospheric or present on the lower surface of the capping flake) or even trapped air leads to blisters within the heterostructure, which may form preferentially over PTCDI islands given the differing surface energies/adsorption energies of hBN and PTCDI. Svatek et al. [148] measured the same red shifted peak in samples processed at much lower temperature, 110°C, though interestingly, this was for monolayer and few-layer hBN flakes, which might be due to the ability of ultra-thin hBN to deform to form high-aspect ratio blisters, leaving more of the heterostructure 'fully encapsulated'.

6.4 PTCDI polarisation

Upon the deposition of 0.5 ML of PTCDI onto hBN at substrate temperature held at 150°C, large monolayer islands are formed, as described previously. Interestingly, the extinction coefficient of the molecule is sufficient that the contrast of monolayer PTCDI

islands can be detected and resolved spatially using optical microscopy, see Figure 6.6 (a), the optical image of this sample with no polarisation filter. When a linear polarisation filter was placed between the sample and the CCD camera, such that the polarisation of the reflected light from the sample could be selected, the contrast of different PTCDI islands on the substrate was found to change. The change in the optical contrast was found to be dependent upon the relative orientation of different needle like PTCDI islands and the position of the polarisation filter, see Figure 6.6 (b), with the polarization filter applied.

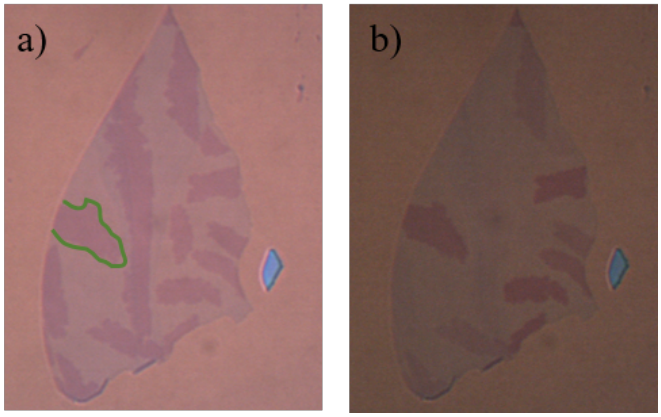


Figure 6.6: Optical image of PTCDI molecules deposited onto hBN flake which the islands are observed where; a) no polarisation filter applied; b) polarisation filter applied. The PTCDI island identified by the green line.

To illustrate the relationship between the polarisation and optical contrast, the contrast of an island identified by the green line as seen in unpolarised image, see Figure 6.6 (a), was investigated by varying the position of a polarisation filter in 2.5° increments. A series of optical images were acquired for the flake for a series polarisation positions. These were analysed by extracting the RGB colour pixel values from the pixels contained exclusively over the indicated island. The absolute magnitude of all three pixels was summated and is shown plotted in Figure 6.7.

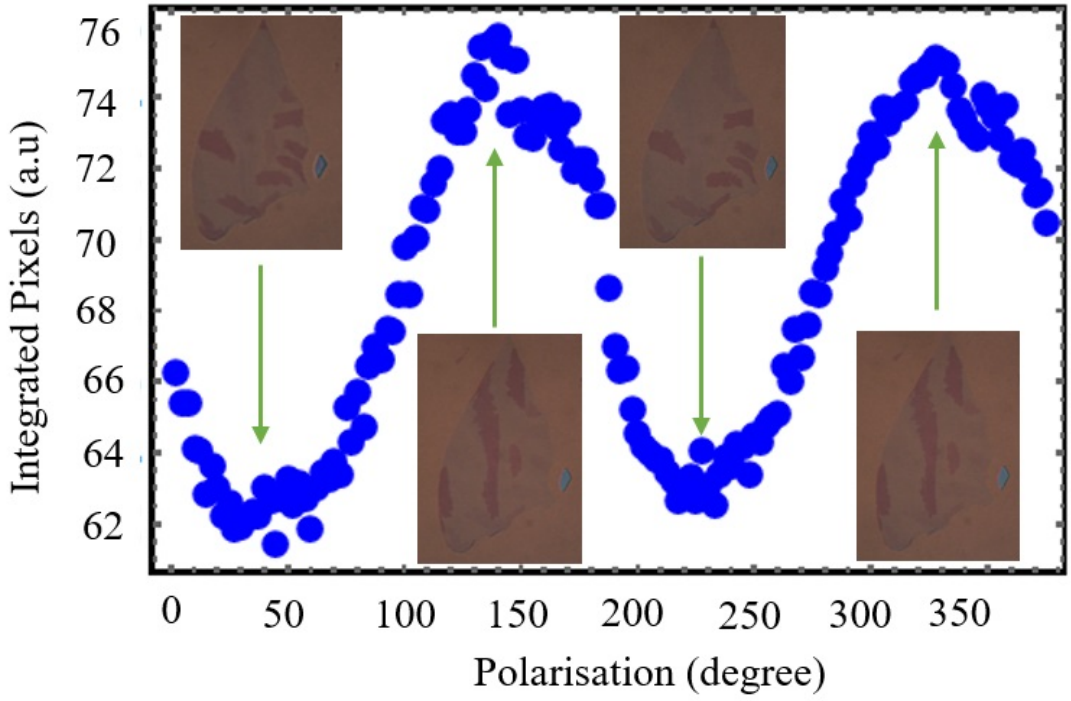


Figure 6.7: The extracted RGB pixel values plotted against the position of the polarisations filter where insets are the optical images at the given polarisations.

As the position of the polarisation filter was modulated over 360°, two maxima and minima were observed. Since the orientation of PTCDI molecules within the molecular monolayer is templated by the canted hydrogen bonding arrangement, all the transition dipoles moments within the structure are oriented along two common directions. When the electric field of the incident polarised light couples to the transition dipole moments of PTCDI, leading to light absorption, this coupling will be strongest when the electric field of the incident light and the transition dipole moments are parallel, and weakest when they are perpendicular.

6.5 Summary

In this chapter, the PTCDI molecules were sublimed onto hBN/SiO_2 and the effect of sandwiching the layers between two insulating hBN layers was explored using fluorescence spectroscopy. The PTCDI islands were studied using optical microscopy before and after the deposition of the capping hBN flake. The produced samples that treated differently using two different cleaning approach (heating and solvent clean) were investigated. The PL measurements for these samples were discussed. Finally, the relationship between the optical contrast and the polarisation was explored.

CHAPTER 7

Self-assembly and photo-polymerization of diacetylene molecular wire on hBN and HOPG

Polydiacetylene is a conducting polymer closely related to polyacetylene. A monomer that can form a polydiacetylene polymer is 10, 12-pentacosadiynoic acid (PCDA), as shown in Figure 7.1. These molecules have a general formula *R*-*C*≡*C*-*C*≡*C*-*R'*, where *C*≡*C*-*C*≡*C* is the diacetylene moiety, *R* and *R'*, the substituent groups. These monomers and polymers have potential applications in biosensors, as pathogenic agents, and in optical and electrical devices [63].

The polydiacetylene polymer derived from PCDA monomers has alternative double and triple bonds which are generated when PCDA is exposed to UV light or external stimuli, such as thermal, chemical and mechanical, as shown in Figure 7.2. The microstructure of these polymers was first reported by Wegner in 1969 [64]. These materials have remarkable properties which include uniform dimensional structures

and responsive chromic characteristics that can be utilized as is, within a solution, or self-assembled onto various substrates, such as silica, polymer, and metal surfaces.

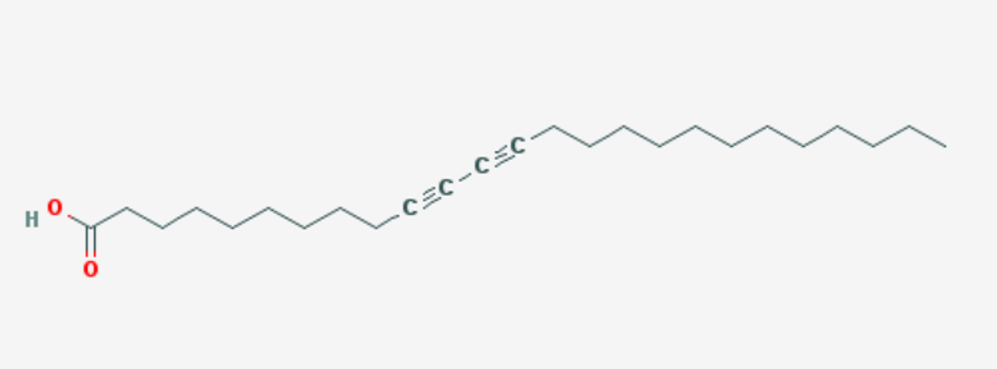


Figure 7.1: The chemical structure of 10,12-pentacosadiynoic acid (PCDA).

Various attempts have been made to adsorb PCDA molecules on different surfaces [67, 149]. A diacetylene-substituted azobenzene derivative was adsorbed by Zhang et al. onto a highly ordered pyrolytic graphite (HOPG) surface resulting in one-dimensional islands [149]. These islands form rows where the molecules are aligned with azobenzene group units formed by two diacetylene that are presented in lower contrast on both sides as shown in the STM image and corresponding model given in Figure 7.3. The length of these units determines the 8.0 ± 0.1 nm line separation. The island morphology was taken before irradiation under ambient conditions. These samples were then exposed to 254 nm light from a mercury lamp. This led to the complex nanostructure of the conjugated polydiacetylene polymer due to polymerization of diacetylene monomers.

In this chapter, self-assembled networks of 10, 12-pentacosadiynoic acid (PCDA) adsorbed onto both hBN and HOPG surfaces will be investigated. The stages of tuning the deposition using various concentrations of different solvents will be included. The polymerization (transition from monomers to polymer) of PCDA molecules and its rate

under UV irradiation will be explored. The results of deposited thin films on both the hBN and HOPG surfaces will be investigated by AFM as this instrument is compatible with insulating and conducting surfaces.

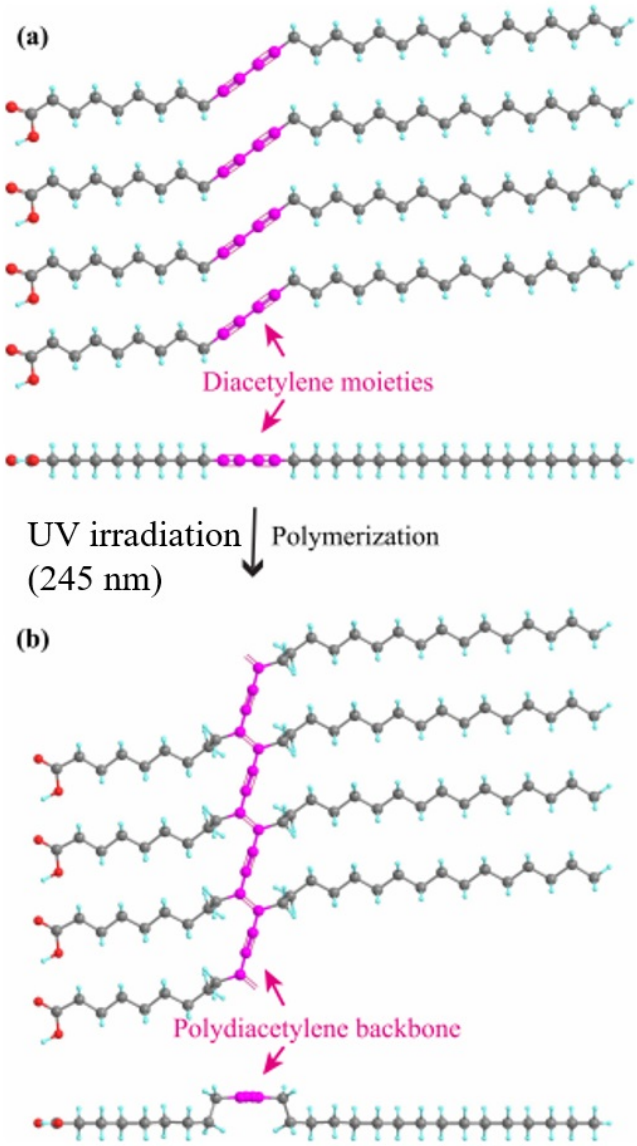


Figure 7.2: The chemical structure of: a) monomer; b) polymer of 10,12-nonacosadiynoic acid adsorbed on HPOG surface. The π -conjugated bonds connected with neighbouring molecules and oriented parallel to the surface [150].

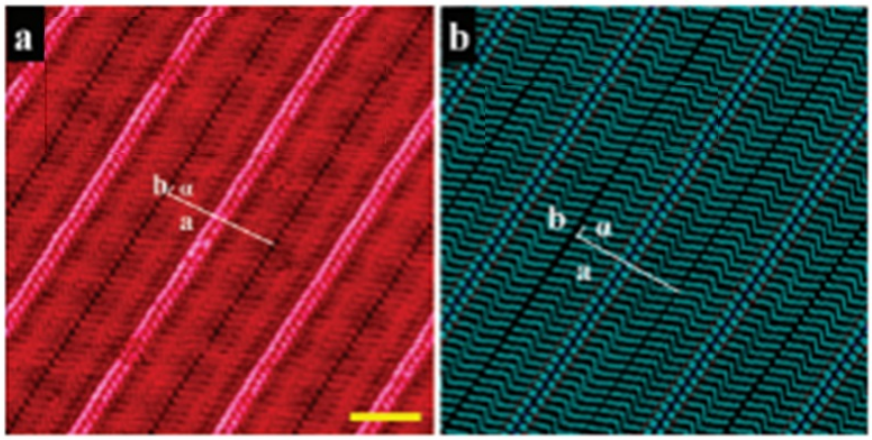


Figure 7.3: (a) STM image of diacetylene-substituted azobenzene derivative adsorbed on HOPG, scale bar = 5 nm. (b) Suggested molecular model of the observed monolayers in (a). The molecules were aligned and formed two diacetylene with units length determines the 8.0 $\pm$ 0.1 nm line separation [149].

7.1 AFM investigation of PCDA self-assemble on HOPG

As discussed above, the HOPG surface was shown to be a good candidate to adsorb PCDA and related molecules, and to trigger a chemical chain reaction by providing energy via electrical pulses using an STM tip [66–68, 70–72, 149, 151, 152].

In this section we evaluate the structures formed by PCDA molecules on HOPG deposited with toluene as the solvent. The solution concentration was 0.1 mg/ml. The HOPG surface was prepared by using scotch tape to remove the upper layer resulting in a freshly cleaved surface. The sample then was immersed for few seconds in the solution. Following immersion for 10 s, very thin islands were deposited on the HOPG surface as shown in Figure 7.4.

The PCDA self-assembled on the HOPG surface and formed row-like islands with orientations separated by 60° which is consistent with the symmetry of the underlying

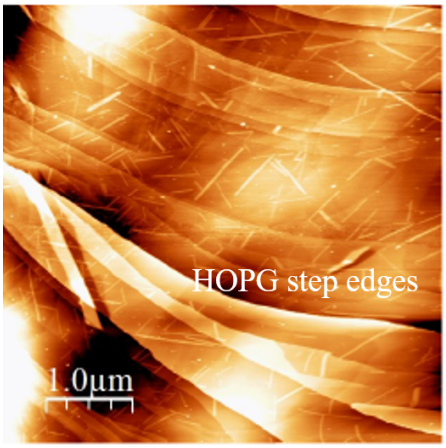


Figure 7.4: AFM topography image for PCDA deposited on HOPG surface with 0.1 mg/ml solution concentration for 10 s.

HOPG lattice. The HOPG edges mostly limit the growth with only a few islands growing over a step edge.

Secondly, the immersion time was increased to 30 s and the resulting molecules appeared as rows in one-dimensional islands, as shown in the AFM images of Figure 7.5 (a-c). These images are similar to those shown in Figure 7.3. Some neighbouring islands, such as that labelled with the blue arrow, see Figure 7.5 (b), have similar orientations but form a domain boundary between them due to their slight misalignment.

The AFM image of highly ordered one-dimensional formations of these islands has a periodic structure and the islands form rows, see Figure 7.6 (a). The phase image in (b) corresponds to the area in the red circle in (a). The line separation within these islands is 7.6 ± 0.3 nm as shown in Figure 7.6 (c). This supports the molecular structure shown in Figure 7.3 in which the molecules aligned with acidic group units are formed by two molecules. The height of the islands is measured to be $\sim$0.15 nm which is consistent with literature [150].

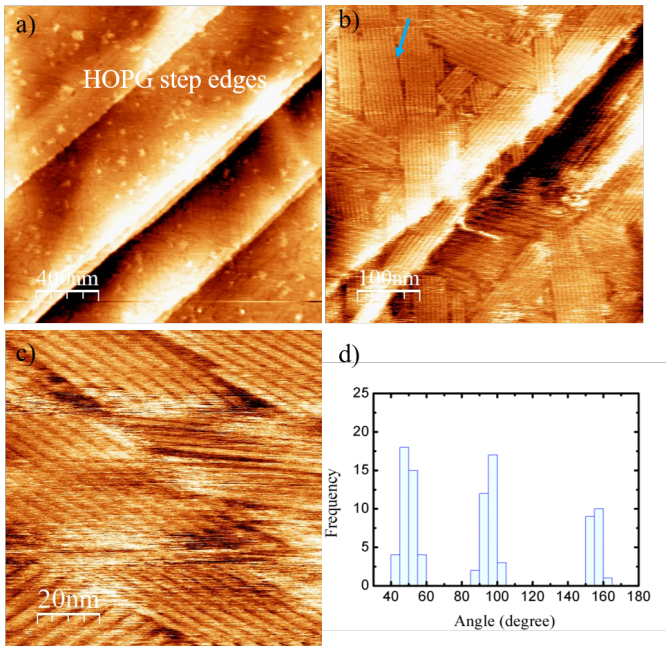


Figure 7.5: (a-c) AFM topography images of PCDA deposited on HOPG surface with 0.1 mg/ml solution concentration for 30 s. The blue arrow is indicated to misalignment domain boundary between the neighbouring islands; d) the island orientations of PCDA were extracted from the AFM image (a) using Gwyddion and are plotted as a histogram.

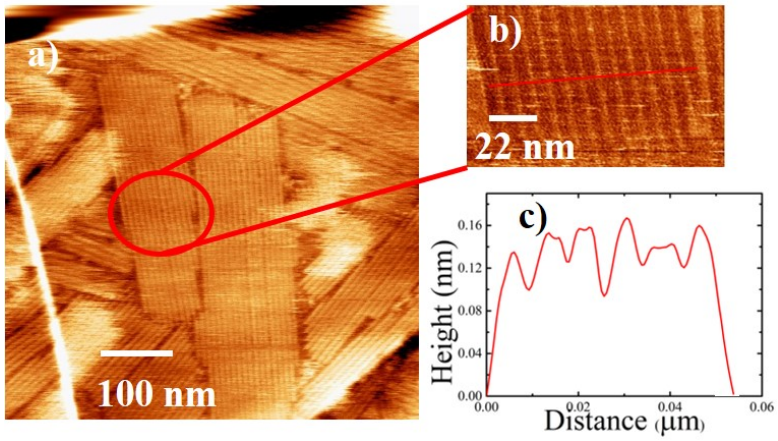


Figure 7.6: (a,b) AFM topography image for PCDA deposited on HOPG surface with 0.1 mg/ml solution concentration for 30 s; c) height profile taken along the red line in (b).

7.2 Deposition of PCDA on hBN

In this section, the quality of deposited thin films of PCDA on the surface of hBN was investigated by testing different solvents and different concentrations of PCDA. Two different solvents were used for this purpose; toluene and IPA. The different self-assemblies using the two solvents are shown below.

Firstly, depositions using IPA were attempted. Solutions were made of 0.1 mg/ml and 0.01 mg/ml concentrations and deposited via immersion for a few seconds then the samples were immediately dried using a flow of nitrogen (N_2). The resulting surface is shown in Figure 7.7. Highly ordered one-dimensional islands were formed on the hBN surface. The islands adsorbed in a manner consistent with the symmetry of the underlying hBN lattice for all concentrations, as shown in the AFM images and associated histogram as shown in Figure 7.7 (right column) for both concentrations with different immersion times.

For all concentrations, the islands have an approximate height $\sim$0.6 nm as shown in the profiles taken from the red lines in the AFM topography images in Figure 7.7 (left column). As discussed below we propose that this height corresponds to a bilayer PCDA molecular structure.

When the sample was deposited for 15 s with 0.01 mg/ml solution concentration, the islands have length and width 0.9 $\pm$ 0.5 μm and 0.18 $\pm$ 0.08 μm respectively. The coverage of this sample is 79%. When decreasing the immersion time for 10 s with the same concentration, the islands have average lengths and width of 0.8 $\pm$ 0.4 μm and 0.2 $\pm$ 0.05 μm respectively. The coverage for this sample was 68%. A further decrease in the immersion time to 5 s for this solution concentration results in a changed

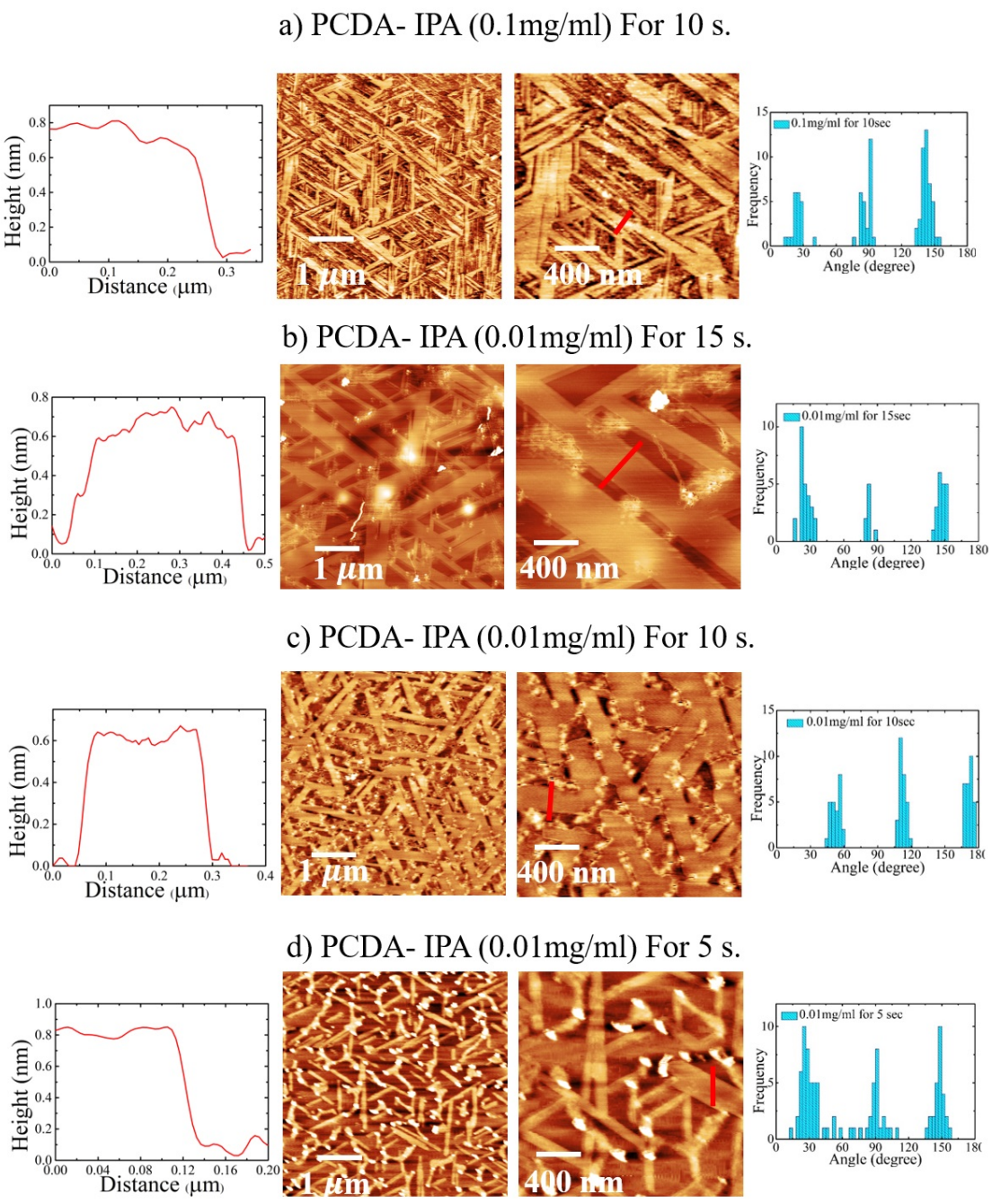


Figure 7.7: (a-d) AFM images of immersion depositions in IPA with different concentrations and different times, as labelled. The right column shown the island orientations of PCDA following extraction from the corresponding AFM images (in the left column) using Gwyddion, plotted as a histogram. The left column show the height profile taken along the red lines in the AFM images.

topography, with a reduced island length and width of 0.6 ± 0.2 μm and 0.1 ± 0.03 μm. The coverage for this sample was 39%.

For the increased concentration of (0.1 mg/ml) with a 10 s immersion an average island length of approximately 0.8 ± 0.4 μm was found. The coverage of this sample also matched that of the 0.01 mg/ml for 10 s deposition, with a coverage of 68%. Figure 7.8 compares the islands lengths and widths for different immersion times.

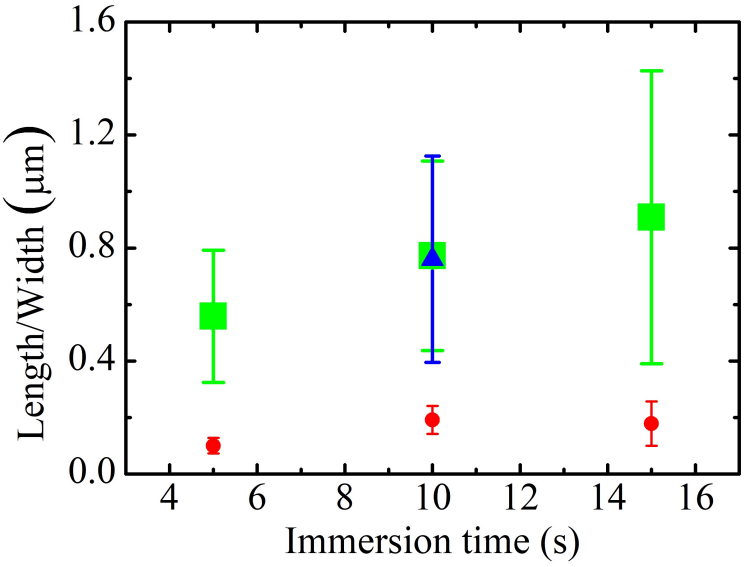


Figure 7.8: The average length and width for different solution concentrations and different immersion times. The green boxes represent the spread of lengths of the measured islands for the 0.01 mg/ml against immersion time, with the corresponding widths shown by red circles. The blue triangle shows the island length of the 0.1 mg/ml deposition.

The AFM images show the PCDA domains are aligned mainly in three directions separated by 60° reflecting the symmetry as the hBN lattice and implying alignment with lattice vectors of hBN. In addition to the flat islands, higher features between domains islands were observed, seen as bright spots in the topographic AFM images,Figure 7.7.

These could be contamination due to the solvent, alternatively the molecules may have become aggregated in the solution.

Following this, a solution in toluene (0.1 mg/ml concentration) was made and the samples deposited using the same method as above. The resulting surface is shown in Figure 7.9.

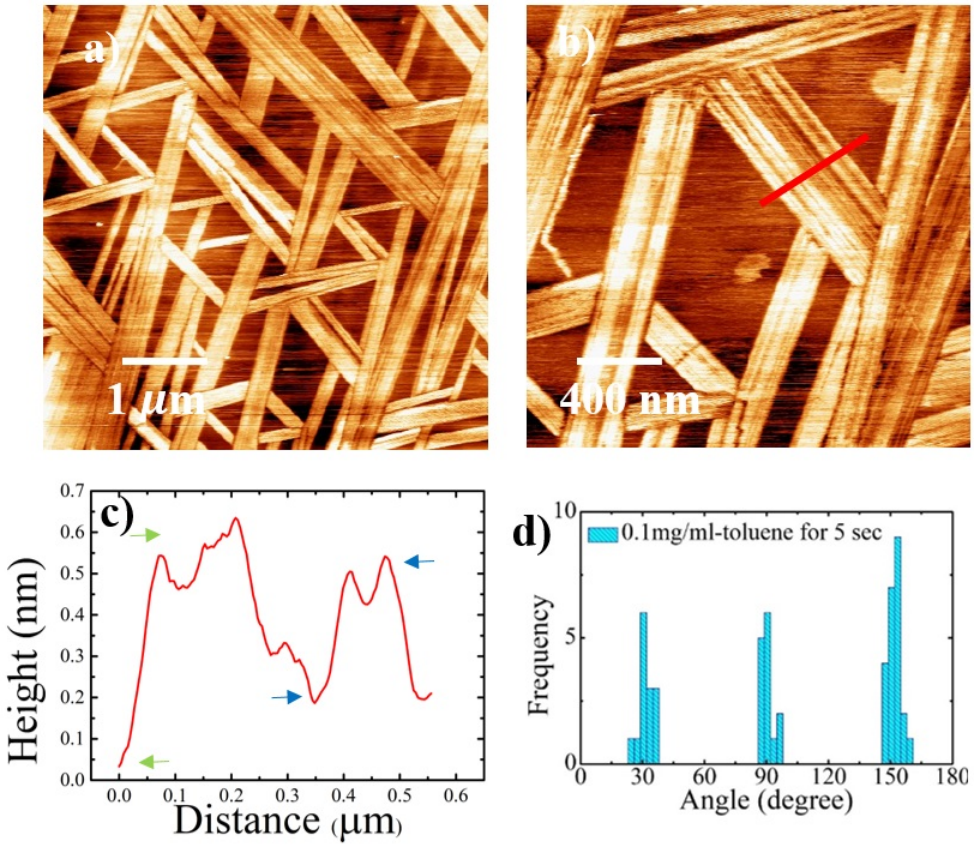


Figure 7.9: (a,b) AFM images of PCDA in toluene for 5 s and the solution concentration 0.1 mg/ml; c) the height profile taken along the red lines in the AFM image in (a); d) the islands orientations of PCDA were extracted from the AFM image (a) using Gwyddion and are plotted as a histogram.

In this sample the surface was much cleaner than for the IPA solution with no aggregates of molecules co-existing with the one-dimensional islands. These islands have contrast levels which are attributed to the presence of monolayers and bilayers, as

shown in the height variation indicated by the blue arrows for the monolayer and the green arrows represent the bilayers, see Figure 7.9 (c). The presence of two height levels gives confidence in the earlier observation of bilayer deposited from IPA. The island orientation is separated by 60° similar to those deposited from IPA. The island have dimensions of 1.4 ± 0.8 μm and 0.2 ± 0.08 μm, length and width respectively. The coverage for this sample was 66% which is comparable to the 10 s deposition for both concentration IPA solution samples.

7.3 Polymerization under UV light

The PCDA molecules exhibit strong optical absorption and fluorescence properties that can change with applied external stimuli [66–68, 70, 71, 149, 151–153]. These changes are due to the nature of the diacetylene groups which are photoactive, and the results show that surface assemblies of this molecule undergo polymerization following irradiation at 254 nm as shown in Figure 7.2. Previously, the chromatic transition molecules have been studied using different external stimuli such as STM tip-induced or UV light for the polymerization. Their results give good guidance for the surface science and engineering to fabricate further optoelectronics device. However, the exact mechanisms are not fully understood [66].

In this section the molecules are deposited onto an atomically flat insulating surface (hBN) to be compatible with PL measurements. The molecules are polymerized with exposure to UV light. The surface topography and PL response for different exposure times were measured for the same sample. The exposure time varies from 1 s up to 5 min in total.

In Figure 7.10, the topography of the AFM images for different exposure times of the same area are shown. Long parallel striped islands corresponding to self-assembled molecules were observed and similar observation were found in literature in the published works on graphite [154] and on hBN [67, 150]. For these islands the polymerization is expected to occur along the chains. The polymerization islands are visible as bright white lines in the topography, one of them indicated with blue rectangle in Figure 7.10 (b) where the darker areas still non-polymerized. The island heights in (a) appear as bilayer (shown by the profile in (c)). After exposure to UV light for 1 s the majority of islands are bilayer with no sign of polymerization, however, one area of possible polymerization was seen which is indicated with green arrow in (a). After a 5 min exposure, new features appeared with a height of 3 nm.

The rows average length and width for 1 s irradiation are 1.4 μm and 0.18 μm respectively. After 5 min irradiation, 0.7 μm and 0.13 μm was the average length and width for the polymerized rows. The surface coverage and island orientation is unchanged by the polymerization.

Figure 7.11 shows the AFM topography image after exposure to UV light for 1 s and the height profile across the two lines shows the height of polymerized chains are 0.16 nm and 0.19 nm higher than variation in non-polymerized stripes. This height is consistent with polymerized PCDA molecules published work on graphite [154] and on hBN [67, 150]. This confirms the polymerized molecules are lifted up and standing above non-polymerized [67, 150, 154] which is explained in model in Figure 7.2. The alkyl chain in this model, remain in the same orientation as the monomer while the backbone of polydiacetylene is raised from the surface.

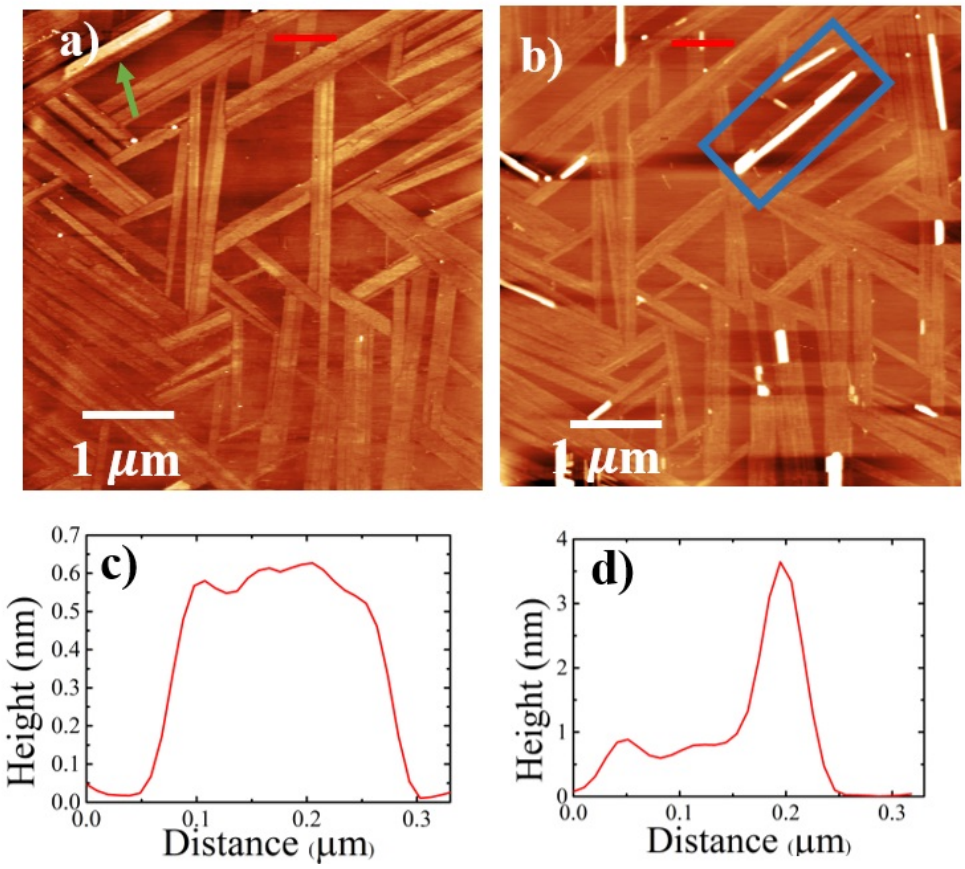


Figure 7.10: AFM topography images of PCDA in toluene (concentration 0.1 mg/ml) adsorbed on a hBN substrate and showing two phases of polymerization: a) after exposure to UV light for 1 s where the green arrow indicates the islands polymerization; b) with a duration of exposure of 5 min in total; (c,d) the height profiles taken along the red lines in the AFM images in (a,b).

The inter-row separation of PCDA on hBN was extracted from image 7.11 (blue arrows) and found to be 7.4 $\pm$ 0.5 nm , as discussed earlier, a similar value was found for the line separation of deposited PCDA on HOPG.

The bulk spectrum for PCDA powder is shown in Figure 7.12 (a). Spectra are recorded using a 405 nm excitation laser with spot size 2 μm^2. In Figure 7.12 (b), the PL response for different exposure times of the same area are shown. The deposited molecules have very low intensity prior to exposure to UV. With increased exposure time to 1 s the

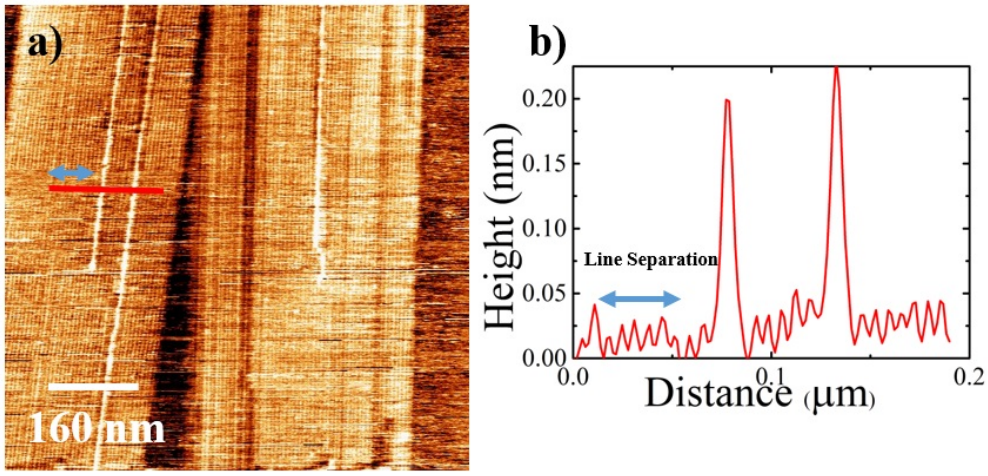


Figure 7.11: (a) AFM topography images of PCDA deposited on hBN after irradiation with UV light for 1 s; b) the average height profile along the red line. The blue arrow highlights the inter-row separations between non-polymerized molecules..

intensity slightly increased. Further exposure time gives a proportionate change in peak and intensity.

The peak positions of the bulk material and deposited material were expected to show a shift in wavelength due to polymerization. However, as shown by Figure 7.12, the peak values have remained the same, with the largest at 483 nm. This may suggest that the powdered bulk material had already experienced some polymerization.

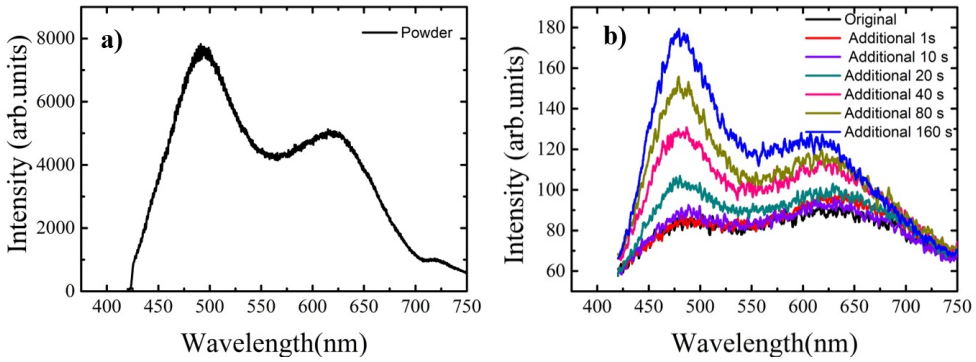


Figure 7.12: PL response for; a) the PCDA powder and; b) the deposition molecules before and after exposure to UV light.

7.4 Summary

In this chapter, the self-assembly of deposited PCDA molecules onto hBN and HOPG surfaces using different solvents and different concentrations was investigated. The highly ordered islands grown on these surfaces have been investigated and their morphology was scanned using AFM.

The PCDA self-assembled molecules on hBN have been exposed to UV light (245 nm) to induce polymerization. The exposure of these molecules leads to topographically bright islands. The intensity of the PL response was increased as a result of increasing the exposure time.

CHAPTER 8

Conclusion

The primary objective of this body of work was to investigate the growth of optically active small organic molecules on insulating substrates. This is an area of study which draws upon ideas in molecular self-assembly on surfaces, organic electronics and 2D materials, with the aim of identifying technologically interesting optical and electronic phenomena which are bestowed upon a material by its structure, which is itself directly influenced by the manner in which it is grown and further processed.

The first example in this work is the case of the self-assembly of free-base phthalocyanine monolayers on hBN, as discussed in Chapter 4, where it was found that the H_2Pc deposited onto hBN forms monolayer islands with height of 0.34 $\pm$ 0.02 nm. These islands were found to arrange on the surface with orientations reflecting the symmetry of the underlying hBN lattice, which has three axes of rotational symmetry separated by 60°. The unit cell of this organic molecules was extracted from high resolution AFM images and found to be a_{Pc}= b_{Pc}= 2.2 $\pm$ 0.03 nm and a_{Pc}= b_{Pc}= 2.18 $\pm$ 0.05 nm for room temperature and higher substrate temperature growth respectively, these lattice vectors were also found to be subtended by an angle θ= 86°. Upon increasing the cover-

age, molecules on hBN were found to form three dimensional islands upon completion of the monolayer, as shown for deposited doses of up to 32 nm equivalent coverage, such 3D islands could be resolved using optical microscopy. The fluorescence of the H_2Pc monolayer was measured using fluorescence microscopy, with the 0-0 peak of H_2Pc on hBN observed at 1.76 eV, which was blue-shifted from the fluorescence of the source material at 1.38 eV. For a series of films of increasing coverage, the fluorescence spectra taken from the 3D islands was found to exhibit a reduced 0-0 monolayer peak (1.76 eV) while the bulk peak (1.38 eV) increased in the intensity. Relative to 0-0 peak of H_2Pc in the gas phase (1.879 eV), the peak was red shifted by ΔE= 0.13 eV.

The ZnPc molecule was also investigated, and was found to form islands with a height 0.6 $\pm$ 0.1 nm, consistent with molecules adsorbed in a non-planar geometry, the fluorescence measurements of these molecules was located at 1.82 eV.

The self-terminated growth of Pc monolayers on hBN discussed in this work is interesting for a number of reasons. Firstly as it is an example of a well-defined system which enables the interplay between the optical properties of an organic material with its structure and adsorption geometry [16, 122, 137]. Ways in which this work could be taken forward include integrating such Pc monolayers into the interfaces of more complicated structures such as van der Waals heterostructures. Here the functional properties of the molecule could be utilised with no loss of in-plane structural control. Furthermore, such phthalocyanine layers could act as a substrate for the heteroepitaxial growth of additional molecular layers, with the potential to grow heterostructures of organic p- and n-type layers, with a well-defined inter-layer registry.

In Chapter 5, the formation of organic heterostructures was discussed, which as mentioned previously, offers the potential to influence device-critical processes in small

molecule organic electronics such as exciton dissociation and diffusion at donor acceptor interfaces. Chapter 5 began with an account of the growth of NTCDI on mechanically exfoliated hBN flakes by sublimation in vacuum, which was found to form anisotropic monolayer islands with height of 0.3 ± 0.1 nm. As the substrate temperature was increased, the size of islands was found to increase, and for growth temperatures of 80°C and 120°C, the island morphology changes to a lily-pad shape. These islands are found to have a plane of approximate symmetry arising from the twinning of adjacent crystals on the surface.

Upon a description of the growth of NTCDI films, the formation of heterostructures produced by sequential deposition of PTCDI/NTCDI, and NTCDI/PTCDI on hBN/SiO_2 was then discussed. For the PTCDI/NTCDI, heterostructure, NTCDI islands exhibited the same morphology as seen previously, a lily-pad shape, while the PTCDI islands possessed different morphologies on NTCDI and on hBN. In both cases the PTCDI islands formed a flat-laying monolayer. These islands were found to have an average length of 0.28 ± 0.07 μm and 0.8 ± 0.2 μm on PTCDI [16] and hBN respectively, which is a consequence of the differing growth kinetics of PTCDI on the two surfaces. The orientation of PTCDI islands on NTCDI was found to be aligned to the underlying molecular layer. The distribution of island orientations relative to the facet direction shows a single peak which corresponds to an alignment with the NTCDI facet. The facet edge indicates the row direction, which we associate with the direction of molecular rows of NTCDI. The dominant orientation of the PTCDI on the NTCDI is theorised to be because the PTCDI aligns with the underlying NTCDI to give the islands the same orientation. This is clearest at the island edges where one dimensional crystalline filaments grow. These are not observed along the straight facet islands.

When the deposition sequence was reversed, the NTCDI was found to form 3D islands on the PTCDI, this suggests the growth mode of NTCDI on PTCDI is different to that on the hBN surface. The NTCDI islands on the PTCDI have a height of 1.5 nm which is suggested that the molecules are not lying flat, and are instead standing up on the PTCDI. Finally, three different layers, NTCDI/PTCDI/NTCDI, with coverages of 0.97 ML (RT)/0.7 ML (RT)/0.97 ML (120°C) respectively, were deposited. The formation of sublimated molecular islands was found to be difficult to track even for this relatively simple multilayer heterostructure.

In Chapter 6, the heterostructures of thick hBN flakes and monolayers of PTCDI were formed using mechanical flake transfer. The change in properties of the encapsulated material was explored with photoluminescence (PL). While this Chapter discusses the relatively simple case of PTCDI encapsulated by hBN, this approach offers numerous opportunities to fabricate technologically relevant devices, with several accounts of hybrid heterostructure devices discussed in the literature. Given the past and ongoing work into the growth of well-ordered molecular films of 2D materials, such systems offer many opportunities to fabricate electronic devices where structure can be imposed on the molecular and monolayer thickness length scales in the in-plane and out-of-plane directions respectively.

In Chapter 7, the self-assembly of PCDA molecules on hBN and HOPG surfaces was carried out using different solvents and different concentrations. Highly ordered islands grown on these surfaces were observed using AFM. The self-assembled molecules on hBN were exposed to the UV light (245 nm), and the light induced polymerisation of these molecules has been discussed. The intensity of the PL response was increased as a result of increasing the exposure time.

Molecular self-assembly, organic-organic formation of heterostructures have been investigated and demonstrated to influence the fluorescent properties of organic thin films. By controlling the structure and environment of organic thin films in this way, their optical properties can be tuned. The experimental methods used in this thesis are immediately applicable to molecular heterostructures containing two or more species and measuring the fluorescent properties of more complicated hybrid heterostructures. Such systems provide an opportunity to test and refine our current understanding in the field of molecular fluorescence in addition to providing structures which could be used to develop novel optical and electronic devices.

Bibliography

[1] Tang, C. W.; VanSlyke, S. A. Organic electroluminescent diodes. *Applied physics letters* **1987**, *51*, 913–915.

[2] Friend, R.; Gymer, R.; Holmes, A.; Burroughes, J.; Marks, R.; Taliani, C.; Bradley, D.; Dos Santos, D.; Bredas, J.; Lögdlund, M.; Salaneck, W. Electroluminescence in conjugated polymers. *Nature* **1999**, *397*, 121.

[3] Peumans, P.; Yakimov, A.; Forrest, S. R. Small molecular weight organic thin-film photodetectors and solar cells. *Journal of Applied Physics* **2003**, *93*, 3693–3723.

[4] Shaheen, S. E.; Brabec, C. J.; Sariciftci, N. S.; Padinger, F.; Fromherz, T.; Hummelen, J. C. 2.5% efficient organic plastic solar cells. *Applied Physics Letters* **2001**, *78*, 841–843.

[5] Gundlach, D. J.; Lin, Y.-Y.; Jackson, T. N.; Nelson, S.; Schlom, D. Pentacene organic thin-film transistors-molecular ordering and mobility. *IEEE Electron Device Letters* **1997**, *18*, 87–89.

[6] Sirringhaus, H.; Tessler, N.; Friend, R. H. Integrated optoelectronic devices based on conjugated polymers. *Science* **1998**, *280*, 1741–1744.

[7] Aakeröy, C. B.; Champness, N. R.; Janiak, C. Recent advances in crystal engineering. *CrystEngComm* **2010**, *12*, 22–43.

[8] Theobald, J. A.; Oxtoby, N. S.; Phillips, M. A.; Champness, N. R.; Beton, P. H. Controlling molecular deposition and layer structure with supramolecular surface assemblies. *Nature* **2003**, *424*, 1029.

[9] Goronzy, D. P.; Ebrahimi, M.; Rosei, F.; Arramel,; Fang, Y.; De Feyter, S.; Tait, S. L.; Wang, C.; Beton, P. H.; Wee, A. T.; Weiss, P. S.; Perepichka, D. F. Supramolecular assemblies on surfaces: nanopatterning, functionality, and reactivity. *ACS Nano* **2018**, *12*, 7445–7481.

[10] De Feyter, S.; De Schryver, F. C. Two-dimensional supramolecular self-assembly probed by scanning tunneling microscopy. *Chemical Society Reviews* **2003**, *32*, 139–150.

[11] Wei, Y.; Tong, W.; Zimmt, M. B. Self-assembly of patterned monolayers with nanometer features: molecular selection based on dipole interactions and chain length. *Journal of the American Chemical Society* **2008**, *130*, 3399–3405.

[12] Ye, Y.; Sun, W.; Wang, Y.; Shao, X.; Xu, X.; Cheng, F.; Li, J.; Wu, K. A unified model: self-assembly of trimesic acid on gold. *The Journal of Physical Chemistry C* **2007**, *111*, 10138–10141.

[13] Chen, W.; Li, H.; Huang, H.; Fu, Y.; Zhang, H. L.; Ma, J.; Wee, A. T. S. Two-dimensional pentacene: 3, 4, 9, 10-perylenetetracarboxylic dianhydride supramolecular chiral networks on Ag (111). *Journal of the American Chemical Society* **2008**, *130*, 12285–12289.

[14] Liu, J.; Chen, T.; Deng, X.; Wang, D.; Pei, J.; Wan, L.-J. Chiral hierarchical molecular nanostructures on two-dimensional surface by controllable trinary self-assembly. *Journal of the American Chemical Society* **2011**, *133*, 21010–21015.

[15] Barth, J. V.; Costantini, G.; Kern, K. *Nanoscience And Technology: A Collection of Reviews from Nature Journals*; World Scientific, 2010; pp 67–75.

[16] Kerfoot, J.; Korolkov, V. V.; Nizovtsev, A. S.; Jones, R.; Taniguchi, T.; Watanabe, K.; Lesanovsky, I.; Olmos, B.; Besley, N. A.; Besley, E.; Beton, p. H. Substrate-induced shifts and screening in the fluorescence spectra of supramolecular adsorbed organic monolayers. *The Journal of Chemical Physics* **2018**, *149*, 054701.

[17] Kerfoot, J.; Korolkov, V. V.; Svatek, S. A.; Alkhamisi, M.; Taniguchi, T.; Watanabe, K.; Parkinson, P. W.; Beton, P. H. Two-Dimensional Diffusion of Excitons in a Perylene Diimide Monolayer Quenched by a Fullerene Heterojunction. *The Journal of Physical Chemistry C* **2019**, *123*, 12249–12254.

[18] Korolkov, V. V.; Baldoni, M.; Watanabe, K.; Taniguchi, T.; Besley, E.; Beton, P. H. Supramolecular heterostructures formed by sequential epitaxial deposition of two-dimensional hydrogen-bonded arrays. *Nature Chemistry* **2017**, *9*, 1191.

[19] Korolkov, V. V.; Svatek, S. A.; Summerfield, A.; Kerfoot, J.; Yang, L.; Taniguchi, T.; Watanabe, K.; Champness, N. R.; Besley, N. A.; Beton, P. H. Van der waals-induced chromatic shifts in hydrogen-bonded two-dimensional porphyrin arrays on boron nitride. *ACS Nano* **2015**, *9*, 10347–10355.

[20] Milián-Medina, B.; Gierschner, J. π-Conjugation. *Wiley Interdisciplinary Reviews: Computational Molecular Science* **2012**, *2*, 513–524.

[21] Nalwa, H. S. *Handbook of Organic Conductive Molecules and Polymers, Volume 2, Conductive Polymers: Synthesis and Electrical Properties*; Chichester: John Wiley and Sons, 1997.

[22] Farchioni, R.; Grosso, G. *Organic electronic materials: conjugated polymers and low molecular weight organic solids*; Springer Science & Business Media, 2013; Vol. 41.

[23] Zu Heringdorf, F.-J. M.; Reuter, M.; Tromp, R. Growth dynamics of pentacene thin films. *Nature* **2001**, *412*, 517–520.

[24] Hlawacek, G.; Puschnig, P.; Frank, P.; Winkler, A.; Ambrosch-Draxl, C.; Teichert, C. Characterization of step-edge barriers in organic thin-film growth. *Science* **2008**, *321*, 108–111.

[25] Zorba, S.; Shapir, Y.; Gao, Y. Fractal-mound growth of pentacene thin films. *Physical Review B* **2006**, *74*, 245410.

[26] Venables, J.; Spiller, G.; Hanbücken, M. Nucleation and growth of thin films. *Reports on Progress in Physics* **1984**, *47*, 399.

[27] Kowarik, S.; Gerlach, A.; Schreiber, F. Organic molecular beam deposition: fundamentals, growth dynamics, and in situ studies. *Journal of Physics: Condensed Matter* **2008**, *20*, 184005.

[28] Schreiber, F. Organic molecular beam deposition: Growth studies beyond the first monolayer. *physica Status Solidi (a)* **2004**, *201*, 1037–1054.

[29] Wang, Y.; Chen, W.; Wang, B.; Zheng, Y. Ultrathin Ferroelectric Films: Growth, Characterization, Physics and Applications. *Materials* **2014**, *7*, 6377–6485.

[30] Kaiser, N. Review of the fundamentals of thin-film growth. *Applied Optics* **2002**, *41*, 3053–3060.

[31] Margenau, H. Van der Waals forces. *Reviews of Modern Physics* **1939**, *11*, 1.

[32] Ratsch, C.; Venables, J. Nucleation theory and the early stages of thin film growth. *Journal of Vacuum Science & Technology A: Vacuum, Surfaces, and Films* **2003**, *21*, S96–S109.

[33] Venables, J. *Introduction to surface and thin film processes*; Cambridge University Press, 2000.

[34] Brune, H. Microscopic View of Nucleation on Surfaces. *Phys. Rev. Lett* **1994**, *73*, 1955.

[35] Stadlober, B.; Haas, U.; Maresch, H.; Haase, A. Growth model of pentacene on inorganic and organic dielectrics based on scaling and rate-equation theory. *Physical Review B* **2006**, *74*, 165302.

[36] Pratontep, S.; Brinkmann, M.; Nüesch, F.; Zuppiroli, L. Correlated growth in ultrathin pentacene films on silicon oxide: effect of deposition rate. *Physical Review B* **2004**, *69*, 165201.

[37] McKeown, N.; B, M. *Phthalocyanine Materials: Synthesis, Structure and Function*; Bruce Dunn; Cambridge University Press, 1998.

[38] Sakamoto, K.; Ohno-Okumura, E. Syntheses and functional properties of phthalocyanines. *Materials* **2009**, *2*, 1127–1179.

[39] Nilson, K.; Åhlund, J.; Shariati, M.-N.; Schiessling, J.; Palmgren, P.; Brena, B.; Göthelid, E.; Hennies, F.; Huismans, Y.; Evangelista, F., et al. Potassium-intercalated H_2Pc films: Alkali-induced electronic and geometrical modifications. *The Journal of Chemical Physics* **2012**, *137*, 044708.

[40] Milgrom, L. R.; Warren, M. J. *The colours of life: an introduction to the chemistry of porphyrins and related compounds*; Oxford University Press Oxford, 1997.

[41] Tang, C. W. Two-layer organic photovoltaic cell. *Applied Physics Letters* **1986**, *48*, 183–185.

[42] Puigdollers, J.; Voz, C.; Fonrodona, M.; Cheylan, S.; Stella, M.; Andreu, J.; Vetter, M.; Alcubilla, R. Copper phthalocyanine thin-film transistors with polymeric gate dielectric. *Journal of Non-Crystalline Solids* **2006**, *352*, 1778–1782.

[43] Nelson, J. *The physics of solar cells*; World Scientific Publishing Company, 2003.

[44] Fujii, N.; Ohmori, Y.; Yoshino, K. An organic infrared electroluminescent diode utilizing a phthalocyanine film. *IEEE Transactions on Electron Devices* **1997**, *44*, 1204–1207.

[45] Wilson, A.; Wright, J. D. Understanding and optimising NO2-sensing using semiconducting phthalocyanine films. *Molecular Crystals and Liquid Crystals Science and Technology. Section A. Molecular Crystals and Liquid Crystals* **1992**, *211*, 321–326.

[46] Caplins, B. W.; Suich, D. E.; Shearer, A. J.; Harris, C. B. Metal/phthalocyanine hybrid interface states on Ag (111). *The Journal of Physical Chemistry Letters* **2014**, *5*, 1679–1684.

[47] Shariati, M.-N.; Luder, J.; Bidermane, I.; Ahmadi, S.; Gothelid, E.; Palmgren, P.; Sanyal, B.; Eriksson, O.; Piancastelli, M. N.; Brena, B., et al. Photoelectron and Absorption Spectroscopy Studies of Metal-Free Phthalocyanine on Au (111): Experiment and Theory. *The Journal of Physical Chemistry C* **2013**, *117*, 7018–7025.

[48] Nilson, K.; Åhlund, J.; Brena, B.; Göthelid, E.; Schiessling, J.; Mårtensson, N.; Puglia, C. Scanning tunneling microscopy study of metal-free phthalocyanine monolayer structures on graphite. *The Journal of Chemical Physics* **2007**, *127*, 114702.

[49] Buchholz, J.; Somorjai, G. The surface structures of phthalocyanine monolayers and vapor-grown films: A low-energy electron diffraction study. *The Journal of Chemical Physics* **1977**, *66*, 573–580.

[50] Gopakumar, T.; Lackinger, M.; Hackert, M.; Müller, F.; Hietschold, M. Adsorption of palladium phthalocyanine on graphite: STM and LEED study. *The Journal of Physical Chemistry B* **2004**, *108*, 7839–7843.

[51] Li, C.; Wonneberger, H. Perylene imides for organic photovoltaics: yesterday, today, and tomorrow. *Advanced Materials* **2012**, *24*, 613–636.

[52] Liu, X.-P.; Xue, L.-W.; Wei, Q.; Liang, M.; Deng, K.; Zhang, Z.-J.; Jiang, P. Seeing Modulability Self-Assembled Monolayers of π-Conjugated Perylene Derivatives by Scanning Tunneling Microscopy. *The Journal of Physical Chemistry C* **2016**, *120*, 18607–18615.

[53] Swarbrick, J.; Ma, J.; Theobald, J.; Oxtoby, N.; O'Shea, J.; Champness, N.; Beton, P. Square, Hexagonal, and Row Phases of PTCDA and PTCDI on Ag- Si (111)$\times$ R 30°. *The Journal of Physical Chemistry B* **2005**, *109*, 12167–12174.

[54] Ludwig, C.; Gompf, B.; Petersen, J.; Strohmaier, R.; Eisenmenger, W. STM investigations of PTCDA and PTCDI on graphite and MoS 2. A systematic study of epitaxy and STM image contrast. *Zeitschrift für Physik B Condensed Matter* **1994**, *93*, 365–373.

[55] Topple, J.; Burke, S.; Fostner, S.; Grütter, P. Thin film evolution: Dewetting dynamics of a bimodal molecular system. *Physical Review B* **2009**, *79*, 205414.

[56] Mura, M.; Silly, F.; Briggs, G.; Castell, M.; Kantorovich, L. H-bonding supramolecular assemblies of PTCDI molecules on the Au (111) surface. *The Journal of Physical Chemistry C* **2009**, *113*, 21840–21848.

[57] Korolkov, V. V.; Svatek, S. A.; Allen, S.; Roberts, C. J.; Tendler, S. J.; Taniguchi, T.; Watanabe, K.; Champness, N. R.; Beton, P. H. Bimolecular porous supramolecular networks deposited from solution on layered materials: graphite, boron nitride and molybdenum disulphide. *Chemical Communications* **2014**, *50*, 8882–8885.

[58] Perdigão, L. M.; Fontes, G. N.; Rogers, B. L.; Oxtoby, N. S.; Goretzki, G.; Champness, N. R.; Beton, P. H. Coadsorbed NTCDI-melamine mixed phases on Ag-Si (111). *Physical Review B* **2007**, *76*, 245402.

[59] Keeling, D.; Oxtoby, N.; Wilson, C.; Humphry, M.; Champness, N.; Beton, P. Assembly and processing of hydrogen bond induced supramolecular nanostructures. *Nano Letters* **2003**, *3*, 9–12.

[60] Sweetman, A.; Jarvis, S. P.; Rahe, P.; Champness, N. R.; Kantorovich, L.; Moriarty, P. Intramolecular bonds resolved on a semiconductor surface. *Physical Review B* **2014**, *90*, 165425.

[61] Jarvis, S. P.; Sweetman, A. M.; Lekkas, I.; Champness, N. R.; Kantorovich, L.; Moriarty, P. Simulated structure and imaging of NTCDI on Si (1 1 1)-7$\times$ 7: a combined STM, NC-AFM and DFT study. *Journal of Physics: Condensed Matter* **2014**, *27*, 054004.

[62] Seydou, M.; Teyssandier, J.; Battaglini, N.; Kenfack, G. T.; Lang, P.; Tielens, F.; Maurel, F.; Diawara, B. Characterization of NTCDI supra-molecular networks on

Au (111); combining STM, IR and DFT calculations. *RSC Advances* **2014**, *4*, 25698–25708.

[63] Charych, D. H.; Nagy, J. O.; Spevak, W.; Ager, J.; Bednarski, M. D. Direct colorimetric detection of virus by a polymerized bilayer assembly. *MRS Online Proceedings Library Archive* **1993**, *330*.

[64] Sun, X.; Chen, T.; Huang, S.; Li, L.; Peng, H. Chromatic polydiacetylene with novel sensitivity. *Chemical Society Reviews* **2010**, *39*, 4244–4257.

[65] Jelinek, R.; Ritenberg, M. Polydiacetylenes–recent molecular advances and applications. *RSC Advances* **2013**, *3*, 21192–21201.

[66] Carpick, R.; Sasaki, D.; Burns, A. First observation of mechanochromism at the nanometer scale. *Langmuir* **2000**, *16*, 1270–1278.

[67] Verveniotis, E.; Okawa, Y.; Watanabe, K.; Taniguchi, T.; Taniguchi, T.; Osada, M.; Joachim, C.; Aono, M. Self-Sensitization and Photo-Polymerization of Diacetylene Molecules Self-Assembled on a Hexagonal-Boron Nitride Nanosheet. *Polymers* **2018**, *10*, 206.

[68] Okawa, Y.; Aono, M. Linear chain polymerization initiated by a scanning tunneling microscope tip at designated positions. *The Journal of Chemical Physics* **2001**, *115*, 2317–2322.

[69] Du, X.; Skachko, I.; Barker, A.; Andrei, E. Y. Approaching ballistic transport in suspended graphene. *Nature Nanotechnology* **2008**, *3*, 491.

[70] Spagnoli, S.; Briand, E.; Vickridge, I.; Fave, J.-L.; Schott, M. Method for determining the polymer content in nonsoluble polydiacetylene films: application to pentacosadiynoic acid. *Langmuir* **2017**, *33*, 1419–1426.

[71] Verstraete, L.; Hirsch, B. E.; Greenwood, J.; De Feyter, S. Confined polydiacetylene polymerization reactions for programmed length control. *Chemical Communications* **2017**, *53*, 4207–4210.

[72] Okawa, Y.; Aono, M. nanoscale control of chain polymerization. *Nature* **2001**, *409*, 683.

[73] Geim, A. K.; Novoselov, K. S. *Nanoscience and Technology: A Collection of Reviews from Nature Journals*; World Scientific, 2010; pp 11–19.

[74] Novoselov, K. S.; Geim, A. K.; Morozov, S. V.; Jiang, D.; Zhang, Y.; Dubonos, S. V.; Grigorieva, I. V.; Firsov, A. A. Electric field effect in atomically thin carbon films. *Science* **2004**, *306*, 666–669.

[75] Novoselov, K. S.; Jiang, Z.; Zhang, Y.; Morozov, S.; Stormer, H. L.; Zeitler, U.; Maan, J.; Boebinger, G.; Kim, P.; Geim, A. K. Room-temperature quantum Hall effect in graphene. *Science* **2007**, *315*, 1379–1379.

[76] Järvinen, P.; Hämäläinen, S. K.; Banerjee, K.; Häkkinen, P.; Ijäs, M.; Harju, A.; Peter, L. Molecular self-assembly on graphene on SiO_2 and h-BN substrates. *Nano Letters* **2013**, *13*, 3199–3204.

[77] Song, L.; Ci, L.; Lu, H.; Sorokin, P. B.; Jin, C.; Ni, J.; Kvashnin, A. G.; Kvashnin, D. G.; Lou, J.; Yakobson, B. I., et al. Large scale growth and characterization of atomic hexagonal boron nitride layers. *Nano Letters* **2010**, *10*, 3209–3215.

[78] Mayorov, A. S.; Gorbachev, R. V.; Morozov, S. V.; Britnell, L.; Jalil, R.; Ponomarenko, L. A.; Blake, P.; Novoselov, K. S.; Watanabe, K.; Taniguchi, T., et al. Micrometer-scale ballistic transport in encapsulated graphene at room temperature. *Nano Letters* **2011**, *11*, 2396–2399.

[79] Watanabe, K.; Taniguchi, T.; Kanda, H. Direct-bandgap properties and evidence for ultraviolet lasing of hexagonal boron nitride single crystal. *Nature Materials* **2004**, *3*, 404.

[80] Summerfield, A.; Davies, A.; Cheng, T. S.; Korolkov, V. V.; Cho, Y.; Mellor, C. J.; Foxon, C. T.; Khlobystov, A. N.; Watanabe, K.; Taniguchi, T., et al. Strain-engineered graphene grown on hexagonal boron nitride by molecular beam epitaxy. *Scientific Reports* **2016**, *6*, 22440.

[81] Dean, C. R.; Young, A. F.; Meric, I.; Lee, C.; Wang, L.; Sorgenfrei, S.; Watanabe, K.; Taniguchi, T.; Kim, P.; Shepard, K. L., et al. Boron nitride substrates for high-quality graphene electronics. *Nature Nanotechnology* **2010**, *5*, 722.

[82] Gorbachev, R. V.; Riaz, I.; Nair, R. R.; Jalil, R.; Britnell, L.; Belle, B. D.; Hill, E. W.; Novoselov, K. S.; Watanabe, K.; Taniguchi, T., et al. Hunting for monolayer boron nitride: optical and Raman signatures. *Small* **2011**, *7*, 465–468.

[83] Wiesendanger, R.; Roland, W. *Scanning probe microscopy and spectroscopy: methods and applications*; Cambridge university press, 1994.

[84] Bhushan, B.; Marti, O. *Springer handbook of nanotechnology*; Springer, 2010; pp 573–617.

[85] Chen, C. J. *Introduction to scanning tunneling microscopy*; Oxford University Press on Demand, 1993; Vol. 4.

[86] Giessibl, F. J. Advances in atomic force microscopy. *Reviews of Modern Physics* **2003**, *75*, 949.

[87] Binnig, G.; Quate, C. F.; Gerber, C. Atomic force microscope. *Physical Review Letters* **1986**, *56*, 930.

[88] Ohnesorge, F.; Binnig, G. True atomic resolution by atomic force microscopy through repulsive and attractive forces. *Science* **1993**, *260*, 1451–1456.

[89] Binnig, G.; Rohrer, H.; Gerber, C.; Weibel, E. 7×7 reconstruction on Si (111) resolved in real space. *Physical Review Letters* **1983**, *50*, 120.

[90] Binnig, G.; Rohrer, H.; Gerber, C.; Weibel, E. Tunneling through a controllable vacuum gap. *Applied Physics Letters* **1982**, *40*, 178–180.

[91] West, P. E. *Introduction to atomic force microscopy theory, practice, applications*; P. West, 2006, 2007.

[92] Fuierer, R. Basic operation procedures for the Asylum Research MFP-3D atomic force microscope. *Asylum Research, Santa Barbara* **2006**,

[93] Hamaker, H. C. The London—van der Waals attraction between spherical particles. *Physica* **1937**, *4*, 1058–1072.

[94] Seo, Y.; Jhe, W. Atomic force microscopy and spectroscopy. *Reports on Progress in Physics* **2007**, *71*, 016101.

[95] García, R. *Amplitude modulation atomic force microscopy*; John Wiley & Sons, 2011.

[96] García, R.; Pérez, R. Dynamic atomic force microscopy methods. *Surface Science Reports* **2002**, *47*, 197–301.

[97] Pedrotti, F. L.; Pedrotti, L. M.; Pedrotti, L. S. *Introduction to optics*; Cambridge University Press, 2017.

[98] Garfitt, J. M. Hydrogen bonding and covalent coupling in adsorbed molecular monolayers. Ph.D. thesis, University of Nottingham, 2014.

[99] Herman, B. *Fluorescence Microscopy and Fluorescent Probes*; Springer, 1996; pp 1–14.

[100] Ishikawa-Ankerhold, H. C.; Ankerhold, R.; Drummen, G. P. Advanced fluorescence microscopy techniques—Frap, Flip, Flap, Fret and flim. *Molecules* **2012**, *17*, 4047–4132.

[101] Kim, K.; Yankowitz, M.; Fallahazad, B.; Kang, S.; Movva, H. C.; Huang, S.; Larentis, S.; Corbet, C. M.; Taniguchi, T.; Watanabe, K.; Banejee, S.; Leroy, B.; Tutuc, E. van der Waals heterostructures with high accuracy rotational alignment. *Nano Letters* **2016**, *16*, 1989–1995.

[102] Pizzocchero, F.; Gammelgaard, L.; Jessen, B. S.; Caridad, J. M.; Wang, L.; Hone, J.; Bøggild, P.; Booth, T. J. The hot pick-up technique for batch assembly of van der Waals heterostructures. *Nature Communications* **2016**, *7*, 11894.

[103] Mali, K. S.; Pearce, N.; De Feyter, S.; Champness, N. R. Frontiers of supramolecular chemistry at solid surfaces. *Chemical Society Reviews* **2017**, *46*, 2520–2542.

[104] Bao, Z.; Lovinger, A. J.; Dodabalapur, A. Organic field-effect transistors with high mobility based on copper phthalocyanine. *Applied Physics Letters* **1996**, *69*, 3066–3068.

[105] de la Torre, G.; Claessens, C. G.; Torres, T. Phthalocyanines: old dyes, new materials. Putting color in nanotechnology. *Chemical communications* **2007**, 2000–2015.

[106] Imada, H.; Miwa, K.; Imai-Imada, M.; Kawahara, S.; Kimura, K.; Kim, Y. Real-space investigation of energy transfer in heterogeneous molecular dimers. *Nature* **2016**, *538*, 364.

[107] Zhang, Y.; Luo, Y.; Zhang, Y.; Yu, Y.-J.; Kuang, Y.-M.; Zhang, L.; Meng, Q.-S.; Luo, Y.; Yang, J.-L.; Dong, Z.-C., et al. Visualizing coherent intermolecular dipole–dipole coupling in real space. *Nature* **2016**, *531*, 623.

[108] Doppagne, B.; Chong, M. C.; Bulou, H.; Boeglin, A.; Scheurer, F.; Schull, G. Electrofluorochromism at the single-molecule level. *Science* **2018**, *361*, 251–255.

[109] Nečas, D.; Klapetek, P. Gwyddion: an open-source software for SPM data analysis. *Open Physics* **2012**, *10*, 181–188.

[110] Yanagi, H.; Kouzeki, T.; Ashida, M.; Noguchi, T.; Manivannan, A.; Hashimoto, K.; Fujishima, A. Molecular orientation of vacuum-deposited thin films of zincnaphthalocyanine. *Journal of Applied Physics* **1992**, *71*, 5146–5153.

[111] Lu, X.; Hipps, K.; Wang, X.; Mazur, U. Scanning tunneling microscopy of metal phthalocyanines: d7 and d9 cases. *Journal of the American Chemical Society* **1996**, *118*, 7197–7202.

[112] Upward, M.; Beton, P.; Moriarty, P. Adsorption of cobalt phthalocyanine on Ag terminated Si (111). *Surface Science* **1999**, *441*, 21–25.

[113] Hamalainen, S. K.; Stepanova, M.; Drost, R.; Liljeroth, P.; Lahtinen, J.; Sainio, J. Self-assembly of cobalt-phthalocyanine molecules on epitaxial graphene on Ir (111). *The Journal of Physical Chemistry C* **2012**, *116*, 20433–20437.

[114] Shao, Y.; Gan, Z.; Epifanovsky, E.; Gilbert, A. T.; Wormit, M.; Kussmann, J.; Lange, A. W.; Behn, A.; Deng, J.; Feng, X., et al. Advances in molecular quantum chemistry contained in the Q-Chem 4 program package. *Molecular Physics* **2015**, *113*, 184–215.

[115] Godlewski, S.; Szymonski, M. Adsorption and self-assembly of large polycyclic molecules on the surfaces of TiO2 single crystals. *International Journal of Molecular Sciences* **2013**, *14*, 2946–2966.

[116] Palmgren, P.; Priya, B. R.; Niraj, N.; Göthelid, M. Bonding of metal-free phthalocyanine to TiO2 (1 1 0) single crystal. *Solar Energy Materials and Solar Cells* **2006**, *90*, 3602–3613.

[117] Palmgren, P.; Nilson, K.; Yu, S.; Hennies, F.; Angot, T.; Nlebedim, C. I.; Layet, J.-M.; Le Lay, G.; Göthelid, M. Strong interactions in dye-sensitized interfaces. *The Journal of Physical Chemistry C* **2008**, *112*, 5972–5977.

[118] Wang, T.; Kafle, T. R.; Kattel, B.; Liu, Q.; Wu, J.; Chan, W.-L. Growing ultra-flat organic films on graphene with a face-on stacking via moderate molecule-substrate interaction. *Scientific Reports* **2016**, *6*, 28895.

[119] Lehnig, R.; Slenczka, A. Emission spectra of free base phthalocyanine in superfluid helium droplets. *The Journal of Chemical Physics* **2003**, *118*, 8256–8260.

[120] Loi, M. A.; Da Como, E.; Dinelli, F.; Murgia, M.; Zamboni, R.; Biscarini, F.; Muccini, M. Supramolecular organization in ultra-thin films of α-sexithiophene on silicon dioxide. *Nature Materials* **2005**, *4*, 81.

[121] Murray, C.; Dozova, N.; McCaffrey, J. G.; Shafizadeh, N.; Chin, W.; Broquier, M.; Crépin, C. Visible luminescence spectroscopy of free-base and zinc phthalocyanines isolated in cryogenic matrices. *Physical Chemistry Chemical Physics* **2011**, *13*, 17543–17554.

[122] Müller, M.; Paulheim, A.; Eisfeld, A.; Sokolowski, M. Finite size line broadening and superradiance of optical transitions in two dimensional long-range ordered molecular aggregates. *The Journal of Chemical Physics* **2013**, *139*, 044302.

[123] Eisfeld, A.; Marquardt, C.; Paulheim, A.; Sokolowski, M. Superradiance from two dimensional brick-wall aggregates of dye molecules: the role of size and shape for the temperature dependence. *Physical Review Letters* **2017**, *119*, 097402.

[124] Forker, R.; Dienel, T.; Krause, A.; Gruenewald, M.; Meissner, M.; Kirchhuebel, T.; Gröning, O.; Fritz, T. Optical transition energies of isolated molecular monomers and weakly interacting two-dimensional aggregates. *Physical Review B* **2016**, *93*, 165426.

[125] Mattioli, G.; Filippone, F.; Alippi, P.; Giannozzi, P.; Bonapasta, A. A. A hybrid zinc phthalocyanine/zinc oxide system for photovoltaic devices: a DFT and TDDFPT theoretical investigation. *Journal of Materials Chemistry* **2012**, *22*, 440–446.

[126] Zhan, X.; Facchetti, A.; Barlow, S.; Marks, T. J.; Ratner, M. A.; Wasielewski, M. R.; Marder, S. R. Rylene and related diimides for organic electronics. *Advanced Materials* **2011**, *23*, 268–284.

[127] Schmitz-Hübsch, T.; Sellam, F.; Staub, R.; Törker, M.; Fritz, T.; Kübel, C.; Müllen, K.; Leo, K. Direct observation of organic–organic heteroepitaxy: perylene-tetracarboxylic-dianhydride on hexa-peri-benzocoronene on highly ordered pyrolytic graphite. *Surface Science* **2000**, *445*, 358–367.

[128] Chen, W.; Qi, D.-C.; Huang, H.; Gao, X.; Wee, A. T. Organic–organic heterojunction interfaces: Effect of molecular orientation. *Advanced Functional Materials* **2011**, *21*, 410–424.

[129] Schwarze, M.; Tress, W.; Beyer, B.; Gao, F.; Scholz, R.; Poelking, C.; Ortstein, K.; Günther, A. A.; Kasemann, D.; Andrienko, D., et al. Band structure engineering in organic semiconductors. *Science* **2016**, *352*, 1446–1449.

[130] Kang, B.; Jang, M.; Chung, Y.; Kim, H.; Kwak, S. K.; Oh, J. H.; Cho, K. Enhancing 2D growth of organic semiconductor thin films with macroporous structures via a small-molecule heterointerface. *Nature Communications* **2014**, *5*, 4752.

[131] Zimmerman, J. D.; Xiao, X.; Renshaw, C. K.; Wang, S.; Diev, V. V.; Thompson, M. E.; Forrest, S. R. Independent control of bulk and interfacial morphologies of small molecular weight organic heterojunction solar cells. *Nano Letters* **2012**, *12*, 4366–4371.

[132] Gimzewski, J.; Reihl, B.; Coombs, J.; Schlittler, R. Photon emission with the scanning tunneling microscope. *Zeitschrift für Physik B Condensed Matter* **1988**, *72*, 497–501.

[133] Forker, R.; Gruenewald, M.; Fritz, T. Optical differential reflectance spectroscopy on thin molecular films. *Annual Reports Section" C"(Physical Chemistry)* **2012**, *108*, 34–68.

[134] Xue, J.; Sanchez-Yamagishi, J.; Bulmash, D.; Jacquod, P.; Deshpande, A.; Watanabe, K.; Taniguchi, T.; Jarillo-Herrero, P.; LeRoy, B. J. Scanning tunnelling microscopy and spectroscopy of ultra-flat graphene on hexagonal boron nitride. *Nature Materials* **2011**, *10*, 282.

[135] Dienel, T.; Loppacher, C.; Mannsfeld, S. C.; Forker, R.; Fritz, T. Growth-Mode-Induced Narrowing of Optical Spectra of an Organic Adlayer. *Advanced Materials* **2008**, *20*, 959–963.

[136] Burke, S.; Topple, J.; Grütter, P. Molecular dewetting on insulators. *Journal of Physics: Condensed Matter* **2009**, *21*, 423101.

[137] Alkhamisi, M.; Korolkov, V. V.; Nizovtsev, A. S.; Kerfoot, J.; Taniguchi, T.; Watanabe, K.; Besley, N. A.; Besley, E.; Beton, P. H. The growth and fluorescence of phthalocyanine monolayers, thin films and multilayers on hexagonal boron nitride. *Chemical Communications* **2018**, *54*, 12021–12024.

[138] Novoselov, K.; Mishchenko, A.; Carvalho, A.; Neto, A. C. 2D materials and van der Waals heterostructures. *Science* **2016**, *353*, aac9439.

[139] Geim, A. K.; Grigorieva, I. V. Van der Waals heterostructures. *Nature* **2013**, *499*, 419–425.

[140] Britnell, L.; Gorbachev, R.; Geim, A.; Ponomarenko, L.; Mishchenko, A.; Greenaway, M.; Fromhold, T.; Novoselov, K.; Eaves, L. Resonant tunnelling and negative differential conductance in graphene transistors. *Nature Communications* **2013**, *4*, 1794.

[141] Britnell, L.; Gorbachev, R. V.; Jalil, R.; Belle, B. D.; Schedin, F.; Katsnelson, M. I.; Eaves, L.; Morozov, S. V.; Mayorov, A. S.; Peres, N. M., et al. Electron tunneling through ultrathin boron nitride crystalline barriers. *Nano Letters* **2012**, *12*, 1707–1710.

[142] Withers, F.; Yang, H.; Britnell, L.; Rooney, A.; Lewis, E.; Felten, A.; Woods, C.; Sanchez Romaguera, V.; Georgiou, T.; Eckmann, A., et al. Heterostructures produced from nanosheet-based inks. *Nano Letters* **2014**, *14*, 3987–3992.

[143] Mouri, S.; Zhang, W.; Kozawa, D.; Miyauchi, Y.; Eda, G.; Matsuda, K. Thermal dissociation of inter-layer excitons in MoS2/MoSe2 hetero-bilayers. *Nanoscale* **2017**, *9*, 6674–6679.

[144] Vasu, K.; Prestat, E.; Abraham, J.; Dix, J.; Kashtiban, R.; Beheshtian, J.; Sloan, J.; Carbone, P.; Neek-Amal, M.; Haigh, S., et al. Van der Waals pressure and its effect on trapped interlayer molecules. *Nature Communications* **2016**, *7*, 12168.

[145] Zhu, X.; Monahan, N. R.; Gong, Z.; Zhu, H.; Williams, K. W.; Nelson, C. A. Charge transfer excitons at van der Waals interfaces. *Journal of the American Chemical Society* **2015**, *137*, 8313–8320.

[146] Ajayi, O. A.; Ardelean, J. V.; Shepard, G. D.; Wang, J.; Antony, A.; Taniguchi, T.; Watanabe, K.; Heinz, T. F.; Strauf, S.; Zhu, X., et al. Approaching the intrinsic photoluminescence linewidth in transition metal dichalcogenide monolayers. *2D Materials* **2017**, *4*, 031011.

[147] Rooney, A. P.; Kozikov, A.; Rudenko, A. N.; Prestat, E.; Hamer, M. J.; Withers, F.; Cao, Y.; Novoselov, K. S.; Katsnelson, M. I.; Gorbachev, R., et al. Observing imperfection in atomic interfaces for van der Waals heterostructures. *Nano Letters* **2017**, *17*, 5222–5228.

[148] Svatek, S. A.; Kerfoot, J.; Summerfield, A.; Nizovtsev, A.; Korolkov, V.; Taniguchi, T.; Watanabe, K.; Antolín, E.; Besley, E.; Beton, P. H. Triplet excitation and electroluminescence from a supramolecular monolayer embedded in a boron nitride tunnel barrier. *Nano Letters* **2019**,

[149] Zhang, X.-m.; Xu, S.-d.; Li, M.; Shen, Y.-t.; Wei, Z.-q.; Wang, S.; Zeng, Q.-d.; Wang, C. Photo-induced polymerization and isomerization on the surface observed by scanning tunneling microscopy. *The Journal of Physical Chemistry C* **2012**, *116*, 8950–8955.

[150] Makarova, M. V.; Okawa, Y.; Verveniotis, E.; Watanabe, K.; Taniguchi, T.; Joachim, C.; Aono, M. Self-assembled diacetylene molecular wire polymerization on an insulating hexagonal boron nitride (0001) surface. *Nanotechnology* **2016**, *27*, 395303.

[151] Wu, A.; Gu, Y.; Tian, H.; Federici, J. F.; Iqbal, Z. Effect of alkyl chain length on chemical sensing of polydiacetylene and polydiacetylene/ZnO nanocomposites. *Colloid and Polymer Science* **2014**, *292*, 3137–3146.

[152] Miura, A.; De Feyter, S.; Abdel-Mottaleb, M. M.; Gesquiere, A.; Grim, P. C.; Moessner, G.; Sieffert, M.; Klapper, M.; Müllen, K.; De Schryver, F. C. Light-and STM-tip-induced formation of one-dimensional and two-dimensional organic nanostructures. *Langmuir* **2003**, *19*, 6474–6482.

[153] Mandal, S. K.; Okawa, Y.; Hasegawa, T.; Aono, M. Rate-determining factors in the chain polymerization of molecules initiated by local single-molecule excitation. *ACS Nano* **2011**, *5*, 2779–2786.

[154] Okawa, Y.; Takajo, D.; Tsukamoto, S.; Hasegawa, T.; Aono, M. Atomic force microscopy and theoretical investigation of the lifted-up conformation of polydiacetylene on a graphite substrate. *Soft Matter* **2008**, *4*, 1041–1047.